Multi Application Solar Telescope (MAST)

P. Venkatakrishnan and MAST Team

Udaipur Solar Observatory
Physical Research Laboratory
P. O. Box 198, Badi Road
Udaipur – 313 001, India

July, 2004

Table of Contents

Glossary

Glossary

AO	Adaptive Optics
BBSO	Big Bear Solar Observatory
CME	Coronal Mass Ejection
CVD	Chemical Vapour Deposition
DOT	Dutch Open Telescope
ECS	Enclosure Control System
EOST	Electro Optic System Technologies
GMRT	Giant Metrewave Radio Telescope
GONG	Global Oscillation Network Group
HCT	Himalayan Chandra Telescope
ICS	Instrument Control System
IS	Imaging System
KIS	Kiepenhuer – Institute für Sonnenphysik
KP	Kitt Peak
LEST	Large Earth-based Solar Telescope
MAST	Multi –Application Solar Telescope
MCS	Mount Control System
MDI	Michelson Doppler Imager
MSFC	Marshall Space Flight Center
MTF	Modulation Transfer Function
NSO	National Solar Observatory
NSST	New Swedish Solar Telescope
PSF	Point Spread Function

RHESSI	Ramaty High Energy Solar Spectroscopic Imager
SHWFS	Shack – Hartmann Wave Front Sensor
SoHO	Solar and Heliospheric Observatory
SOLIS	Synoptic Optical Long-term Investigations of the Sun
STEREO	Solar TErrestrial RElations Observatory
SVST	Swedish Vacuum Solar Telescope
TCS	Telescope Control System
USO	Udaipur Solar Observatory

1. Introduction

With an impressive history of more than 300 years of recorded solar observations, solar physics has definitely attained the status of a mature discipline. In many ways, this wealth of information about the Sun has posed exciting challenges to Man's understanding of natural phenomena. One illustrious example is the way in which the relatively new technique of helioseismology has led to a fresh look at the fundamental properties of neutrinos. There are a number of other examples which, if not as spectacular as the solar neutrino problem, are quite challenging. The resolution of some of these questions will lead to possible methods of heating and confining plasma on the one hand, and to an enhanced capability for predicting major solar eruptions, on the other. The former has potential applications for constructing viable fusion reactors - a valuable source of energy for human activities, while the latter will allow us to anticipate the serious disruptions to satellites, terrestrial power and communication systems that are occasionally caused by the solar eruptions. On a more academic plane, the Sun serves as the Rosetta stone for all theories about stars, which in turn constitute the galaxies, and therefore the very Universe in which we live.

The Indian efforts in solar physics have also a long history. Jansen discovered Helium in the flash spectrum seen just before a total solar eclipse observed from Guntur in 1868. The Government of India established the Kodaikanal Observatory in 1899 with the express purpose of studying the connection, if any, between the solar cycle and recurrence of droughts in India. Soon after its inception, Evershed (1909) made a fundamental discovery about the radial outflow of gas from sunspots. It is interesting to note that these discoveries were possible either because of unique circumstances (eclipses) or because state-of-the-art equipment (Evershed's spectrograph) was used. A. K. Das installed the next major facility - the tower/tunnel telescope at Kodaikanal in 1960. This led to several studies of solar velocity oscillations (Bhatnagar, 1968; Sivaraman, 1970; Bhattacharyya, 1970), which are perhaps some of the earliest investigations on helioseismology. Later efforts, albeit commendable, could never attain the cutting edge, because the international facilities rapidly attained standards far beyond the capabilities of the Kodaikanal telescope. The scope for uninterrupted observations was enhanced by the establishment of a small observatory on an island in lake Fatehsagar at Udaipur in 1975, by A. Bhatnagar. Later on, this observatory started functioning as one of the 6 sites of the GONG network of telescopes collecting information about the solar interior. Although this site tries to mimic the conditions at the Big Bear Solar Observatory (BBSO), the presence of a lake seems to be the only similarity. At BBSO, the ambient air temperature is not much different from that of the water surface. At USO, the ambient air temperature far exceeds the water surface temperature during summer. As a result, even a small wind flow could produce forced turbulence, and hence spoil the seeing. The lake is also prone to drying up in summer, in recent times, further aggravating the problem. However, the site provides more than 270 clear days in a year, which is extremely important for intensive study of solar phenomena. Thus, we have decided to remain at this site, and install a new telescope of the largest size that can optimally benefit from adaptive optics. In what follows, we will first enumerate the science goals that we have set out to achieve. Then, we will arrive at the optimum size of the telescope that will benefit from adaptive optics. In the following sections, we will discuss the optical design, mount specifications, tip-tilt secondary and guider telescope, weather parameters, dome and building, control systems and back-end instruments.

2. Science Goals

2.1. Justification For a Facility at USO and Strategy For Choice of Science Goals

2.1.1 Site Conditions

The contiguous number of clear days is very large, thereby allowing for long time monitoring of solar activity. Location within a moderate sized city with rail and air connections is no mean advantage for logistics.

2.1.2 Longitude Advantage

India is situated at a crucial longitude for synoptic coverage of solar phenomenon. The resounding success of the GONG project in terms of new results about the internal dynamics of the Sun is in no small part due to the participation of Udaipur Solar Observatory at such a crucial longitude. Many new projects like SOLIS will realise their full potential only if the magnetic field variations are monitored without large temporal gaps. New missions like the STEREO mission would rely on magnetic field information observed from all longitudes. Thus, the ability to fill a niche in studies of the solar magnetic field, justifies the inclusion of solar magnetism as one of the major targets of study.

2.1.3 Expertise

As far as expertise is concerned, the Udaipur Solar Observatory has been involved in the study of the active Sun on the one hand, while it has also benefited academically by hosting the GONG instrument. Recent results from USO have shown the possibility of using the acoustic spectrum of the Sun as a new diagnostic tool for probing solar activity mechanisms (Bhatnagar, Jain and Tripathy, 2002; Venkatakrishnan, Kumar and Tripathy, 2002; 2003; Tripathy, Jain and Bhatnagar, 2003; Ambastha, Basu and Antia, 2003; Ambastha et al., 2004). The operation of the GONG instrument has also created skills in maintaining state-of-the-art instruments, as well as familiarity with well planned projects. Furthermore, the use of MSFC vector magnetograms to understand the pre-flare magnetic configuration of active regions has increased USO's interest in making a vector magnetograph. Having successfully completed a line-of-sight videomagnetograph, USO is finalising the installation of a vector magnetograph. This activity would prepare USO for making a more sensitive magnetograph at the back of a larger aperture telescope. Here again, solar magnetism seems to be the most appropriate subject of study, from the viewpoint of expertise available. Furthermore, expertise on high angular resolution techniques was accumulated through many Ph.D. thesis projects and short term student projects on these techniques (Krishnakumar, 2000; Sridharan, 2003).

Keeping in view the afore-mentioned strengths of USO, it would seem most profitable to focus on high angular resolution studies *(expertise advantage)*, solar polarimetry *(geographical location and expertise advantage)*, and mechanisms of solar variability *(site, geographical location and expertise advantage).*

2.2. Brief Description of Science Goals

We now proceed to give a brief description of the various scientific problems that need to be studied extensively. Several of these problems require the accumulation of high quality data on a regular basis. Obviously, we need our own facility so that any chosen problem can be pursued in great depth. This is the only way to do basic science and "quick fixes" like obtaining limited observing time on existing international facilities cannot be a substitute for such an intensive approach. A new generation of young solar astronomers, trained to use such modern facilities will be able to leapfrog to even greater achievements.

2.2.1 High Angular Resolution Studies

The Sun is a unique plasma physics laboratory, which produces phenomena spanning ten orders of magnitude in spatial scales. The largest scales deal with very fundamental processes like the solar dynamo and the solar cycle. However, these phenomena have defied explanation for the past 100 years, because of the fact that the crucial process of destruction of magnetic field occurs on the smallest possible scales. Thus, the importance of obtaining statistical information on the smallest observable scales of magnetic and velocity fields for estimating the parameters of the diffusion and destruction of magnetic flux cannot be over-emphasized. Some details follow:

Statistics of small-scale magnetic fields: The availability of a stable platform and long temporal baseline on board the Solar and Heliospheric Observatory (SoHO) satellite enabled Schrijver et al. (1998) to accumulate accurate statistics on flux cancellation events near the network boundary in quiet regions with an angular resolution of 0.5 arc-sec. These new results have altered the estimates for diffusion and random walk of magnetic elements drastically, requiring a fresh look at the problem of sunspot structure (Venkatakrishnan, 2000). It is expected that the diffusion process will be significantly altered in regions of strong magnetic fields. We therefore propose to monitor the random walk parameters and examine the changes produced near and at regions of strong magnetic fields. We already have started seeing interesting results using the Michelson Doppler Imager (MDI) on board SoHO, like the inward movement of magnetic inhomogeneities in sunspot umbrae (Ravindra, Venkatakrishnan and Kumar, 2004). Once these changes are estimated, then we can study the temporal behaviour of these parameters to predict emergence of magnetic flux. A finer spatial resolution and continuous monitoring will ensure more complete statistics, and hence greater reliability in the predictions.

Small-scale intensity features: Intensity features at small scales provide important details about thermal processes occurring on small scales. A very good example is the statistics of small white light flares. Usually, white light flares are rare events because these become detectable only when their size is reasonably large. However, it could well be that small sized flares are more frequent. By observing with higher angular resolution, it is possible to build up the statistics of these events. Since white light flares are manifestations of the most intense electron beams capable of penetrating the chromosphere and reaching the photosphere, increasing the database on their statistics will provide a huge impetus to the difficult problem of particle acceleration. In a recent attempt at interferometric imaging, an intense continuum source of 0.3 arc-sec size was observed that lasted for several tens of minutes (Sridharan and Venkatakrishnan, 2001). Radio flares of small size were also seen in the archives of Nobeyama observatory (Kundu, 1999, seminar at USO). G-band bright points are another example where recent results (Lofdahl et al., 1998) show possibilities of looking for chromospherhic (Krishnakumar and Venkatakrishnan, 1999) and coronal (van Ballegooijen et al., 1998) heating agents. Clearly, more data is necessary to build a complete theory for such processes.

Small-scale velocity features: Flow patterns within sunspots and active regions observed recently with the adaptive optics system developed at Sac Peak, USA, show intriguing properties (Rimmele, 2004) that were not observed earlier with lower angular resolution (Beckers, 1981). It is quite possible that these velocity patterns result from a very fragmented state of the sunspot magnetic fields. More efforts are required in this area.

Likewise, velocity data at higher angular resolution will enable us to look for vortices that could create meso-scale organisation of flow on larger scales.

2.2.2. Solar Polarimetry

Polarisation of sunlight provides unique information about the magnetic field or scattering properties of the solar atmosphere. This branch of solar studies has received considerable attention in recent times (Stenflo, 1994; Stenflo and Nagendra, 1996; Nagendra and Stenflo, 1999). The polarised spectrum of the Sun is so different from the intensity spectrum, that Stenflo has called the former as the "second solar spectrum". The largest number of applications of solar polarimetry is in the measurement of solar magnetic field using the Zeeman effect. However, there have been several results in recent times that use the Hanle effect as well to study the polarisation induced by scattering within resonance lines.

Sunspot structure and evolution: The evolution of sunspots can be understood either as the manifestation of different cross-sections of an emerging flux rope (Leka et al., 1994) or as the coalescence of a large number of small magnetic elements (Parker, 1979). Proper motion of sunspots, their areal evolution and flare activity in active region also need attention (Ambastha and Bhatnagar, 1988). The measurement of vector magnetic fields of an evolving sunspot along with the associated velocity fields can provide a good discrimination between the opposing models, provided a consistent set of well calibrated vector magnetograms are available. In most cases, there will be a need to monitor this evolution with a fair amount of temporal sampling. Single stations might not suffice for this purpose. We therefore propose to obtain vector magnetograms with the same spectral lines as used by the proposed SOLIS instrument (Keller, 2000).

Canopy fields and acoustic frequency shifts: Recent results using GONG data (Bhatnagar, Jain and Tripathy, 1999; Jain, Tripathy and Bhatnagar, 2000) have clearly established a correlation between solar cycle and acoustic frequency shifts. One of the possible causes of the frequency shift could be the change in the reflectivity of the upper wall of the acoustic cavity. Changes in the properties of the canopy fields with the solar cycle could well change the reflectivity of the upper boundary. Recently, the Hanle effect was used to successfully model the canopy magnetic fields (Faurobert-Scholl, 1993). Thus, an important science goal would be the use of the Hanle effect to monitor the changes produced in the canopy magnetic fields.

Polarisation of molecular lines: Stenflo and Keller (1997) had measured polarisation in molecular lines, which was interpreted by Rangarajan and Rao (1999). The molecular polarisation measurements would thus provide information on the detailed balance between the formation and dissociation of molecules at different regions of the Sun – verily, a completely new window on the chemistry of the solar atmosphere.

Resonance line polarisation: Measurements of the chromospheric magnetic fields are hard to come by because most of the strong chromospheric lines are resonance lines whose polarisation is hard to interpret. Recent developments in polarised radiative transfer theory have enabled better application of resonance line polarimetry. For example, the pattern of polarisation within resonance lines has been used to propose a novel technique for detecting waves in the chromosphere (Rangarajan, 1999).

2.2.3 Mechanisms of Solar Variability

Solar magnetism manifests in a hierarchy of spatial scales, as well as temporal scales. It is becoming more and more evident that there is strong interaction and coupling at various scales. The study of these interactions will occupy the solar physicists during the current solar cycle. Some specific areas where this study can be used are:

Solar flare prediction: Solar flare prediction is an important component of space weather forecasting. The current progress on this kind of activity leaves ample room for improvement. The difficulty in using photospheric magnetic fields (Ambastha, Hagyard and West, 1993) could well be due to the constraints imposed on the photospheric field by sub-photospheric dynamics (Hagyard, Stark and Venkatakrishnan, 1999). The velocity fields associated with the active regions might also provide another handle to this problem (Fontenla et al., 1995; Debi Prasad et al., 1998; Debi Prasad, 2000). Monitoring of the chromospheric magnetic fields promises to improve our predictive capability because the chromospheric magnetic fields are more force-free in nature as reinforced by observed changes in Hα filaments related to flares (Sivaraman et al., 1992). Along with flare prediction, one needs to forecast coronal mass ejections too. This would require the close monitoring of filament and prominence activities (Srivastava, 1994; Srivastava et al., 2000).

Magnetic origin of CMEs: It is now well established that CMEs originate from active regions. The coronal dimming of active regions associated with CMEs (Zarro et al., 1999), the clear identification of EIT waves with several CMEs (Thompson et al., 1999), the relationship of non-potentiality of active regions (Falconer et al., 2002) with the CME productivity, the relationship of total magnetic energy of an active region with the speed of the ejecta (Venkatakrishnan and Ravindra, 2003), are all different manifestations of the influence of active region magnetic fields on the CME phenomenon. Many of the previous studies were restricted to evaluating magnetic fields close in time to the event. This does not tell us much about the previous history of the active regions. We do not know how exactly the field evolved into a state that produced the ejection. We will rectify this situation by a dedicated study of all active regions by obtaining vector magnetograms of all active regions using the vector magnetograph at the back-end of MAST. The various indices of non-potentiality will be calculated and the evolution of these parameters will be monitored. The Udaipur site gives 270 plus clear days in a year and hence a great deal of information will be collected. This information will be correlated with any CME that would occur during the period of our study and a clear picture of the connection between vector magnetic field parameters and CME parameters will be established.

CMEs are associated with both the large solar flares and prominence eruptions observed in the chromosphere. However, it is not well understood as to what distinguishes the filament eruption/flare events producing CMEs from those that are not associated with CMEs. The fastest CME events are believed to be associated with the flares, while the slow, gradually accelerating events are associated with erupting prominences (MacQueen and Fisher, 1983), but this issue is far from settled (Feynman and Ruzmaikin, 2004). This problem needs to be addressed. Further, using simultaneous, multi-wavelength observations, it would be possible to track CMEs to the solar disk to look for changes in chromospheric, magnetic and velocity field structures (Hudson and Cliver, 2001). Recent studies have shown that from the space weather prediction point of view, fast CMEs associated with flares which originate close to central meridian and low latitude areas are candidates for major geomagnetic activity at the earth (Srivastava and Venkatakrishnan, 2004). The ultimate aim is to use these disk signatures as a predictive tool for geo-effective CMEs.

It is also important to follow the magnetic field evolution of active regions over several solar rotations. Some studies have shown that flares and CMEs occur during the early stages of the active region evolution (van Driel-Gesztelyi et al., 1999). On successive rotations, flares cease to occur but CMEs continued.

High time-resolution studies: The scattering of sound waves from magnetic structures can provide diagnostics about the internal fine-structure of these elements (Venkatakrishnan, 1979). Likewise, the study of micro and nanoflares will add to our understanding about coronal heating (Udit Narain and Ulmschneider, 1990). Thus, it would be very important to study the time variability on very short time-scales. A stable observing platform including an adaptive optics system would make these measurements very reliable. Some of the problems to be studied using such a system include oscillation of filaments/prominences, and oscillations in sunspots and pores, to name a few.

2.3 Summary and Conclusions

The science goals mentioned above provide only a limited list that would benefit maximally from the points of view of the various parameters of site, location, and expertise mentioned at the very beginning of this chapter. This does not preclude other goals that may be important for other researchers from different solar groups, both within the country and from abroad. In fact, some of these goals would definitely overlap, and would therefore serve as platforms for close interaction and collaboration amongst the groups. The back-end instrumentation can be so designed as to meet most of the desired goals. Likewise, the multi-wavelength observations require collaboration with a larger community that is familiar with radio observations (e.g. GMRT, Gauribidanur radioheliograph, Nobeyama array) and with space observations (RHESSI, SOLAR-B, STEREO, etc). However, the advantages of focussing on a few front-line problems are quite obvious. By having a world class facility, we can also attract a larger number of young people, who generally prefer to work on exciting and challenging problems.

3. Optimum Size of Telescope

The desirable spatial resolution to meet our science goals is 0.2 arc-sec, which is the diffraction limit of a 50 cm telescope at 500 nm. Generally, one plans for a bigger telescope to have a “cushion” in terms of photons, efficiencies of resolving power, etc. Our plan to use a combination of low order adaptive optics and speckle reconstruction is limited by the typical “seeing” conditions at our site. The frequent drying up of the lake in recent times is also a matter of concern. Thus, it is crucial to determine what size of telescope will provide the desired resolution after employing adaptive optics (AO) and speckle reconstruction, at the worst “seeing” conditions. In order to do this, we have to first determine the “seeing” parameter, then use it in simulations of the adaptive optics and speckle procedure for various telescope apertures and find out the optimum size. To know about the adaptive optics, we need to collect information about the existing systems. Finally, we have to build a prototype system and actually try out the difficult technology in-house since complete AO systems are not commercially available. In this section, we report our results on all these tasks.

3.1 Estimation of “Seeing” when Lake Fatehsagar was Completely Dry

Lake Fatehsagar had dried out completely during October 2002 - July 2003. A special observing schedule was implemented from March 20th to April 10th 2003 to estimate the seeing using spectral ratio method (von der Lühe, 1984). A series of 100 to 200 images of quiet Sun solar features was recorded in Hα line with an exposure time of 33 ms and a frame rate of 3 frames per second, 3 or 4 times a day separated by approximately 1.5 hours using the central 7.5 cm aperture of the 15 cm spar telescope. The images were analysed and the Fried’s parameter was estimated for each series. The estimated values were in the range of 1.5 to 3 cm. There was an indication of the seeing becoming worse during the mid-day and reverting back to its morning value after 2 pm. It should be noted that unlike other methods of site characterisation, the spectral ratio method provides an estimation of the effective seeing (combined effect of the site, dome and the telescope). For further details, please refer to Annexure I.

3.2 Compilation of Information on Existing Solar AO Systems

3.2.1 Swedish Vacuum Solar Telescope (SVST)/ New Swedish Solar Telescope (NSST) Activities:

Scharmer and colleagues implemented adaptive optics in 1999 on their 50 cm solar telescope located at La Palma, Canary Islands. It became fully operational in 2001 (Scharmer et al., 2003). They used a cross-correlation Shack-Hartmann Wave-front Sensor (SHWFS) and a 19 element bimorph mirror from Laplacian Optics, for low order (18 Zernike modes) corrections. The control computer was a DEC alpha workstation at 500 MHz, with a specialised Compaq fast link. The CCD frame rate was 995 frames per second and the controller delay was 0.43 ms. The control software was optimized and is now available for other users (http://www.solarphysics.kva.se). Scharmer’s group also implemented adaptive optics in 2002 on their new 97 cm solar telescope (NSST). It is a low-cost, system simple to develop, maintain, calibrate and use. The system is intended for use only under good seeing conditions. The new system uses a correlating SHWFS with 37 sub-apertures, a 37 element bi-morph mirror capable of correcting for 28 Karhunen-Loeve (KL) modes and an Athlon 1400 MHz processor. A 200 mm tip-tilt mirror controlled by dc motors in SVST was upgraded to a 40 mm tip-tilt mirror with piezo actuators in NSST. The group accumulated extensive experience in the past years, with the method of phase diversity to retrieve post-facto the full diffraction limited resolution. The method works if there is high signal to noise ratio in the spatial frequency domain (e.g. very good seeing to start with). The method does not work at all for long exposure images.

3.2.2 Kiepenhuer-Institut für Sonnenphysik (KIS) Vacuum Tower Telescope Activities.

KIS has implemented a 50 mm fast steering tip-tilt mirror since 1995 on their 70 cm solar telescope fed by a coelostat. KIS used a clear aperture of 60 cm for adaptive optics. The group implemented AO in 1999-2000, with high bandwidth (> 150 Hz). A 6 × 6 element SHWFS and a 35-element bimorph mirror are used along with DEC alpha 667 MHz workstation. Low order adaptive optics followed by speckle interferometry is found to yield diffraction limited imaging performance at visual wavelengths. While neither speckle imaging nor adaptive optics alone can achieve resolution better than 500 km on the Sun, the hybrid imaging (adaptive optics and speckle interferometry) technique is found to be capable of achieving diffraction limited performance.

3.2.3 Sacramento Peak Observatory Activities

Sac Peak has been a pioneer in solar adaptive optics. Low-order adaptive optics (correction up to 20 Zernike terms) has been implemented on the 76 cm Richard Dunn Solar Telescope and is fully operational since 1999. A fast tip-tilt system has been implemented on the same telescope since 1987. A 24 sub-aperture correlating SHWFS for sensing the wave-front, a 80 mm dia, 97 actuators piezo-stack deformable mirror (Xinetics Inc.) and custom made DSP boards for on-the-fly cross-correlation and control are the main features of this system. The system bandwidth of low order adaptive optics is 25 Hz. Phase diversity has been tested and used with similar experience as that of the Swedish group. A higher order AO system is operational since October 2003 (Rimmele, 2004).

3.2.4 Kitt Peak Observatory Activities

A low cost adaptive optics system was implemented with the 50 cm clear aperture of the 1.5 m McMath Pierce solar telescope in mid 2002 for infra-red (830 nm) wavelengths. A tip-tilt mirror with a tilt range of 8-milli radian was used. A 15 mm dia, 37-actuator membrane mirror from OkoTech was used as corrector. A 200 sub-aperture SHWFS was used for sensing the wave-front. The system bandwidth was about 125 Hz.

3.2.5 Answers to Some Critical Questions

What is the typical operation time of the working AO systems?

Closed loop update rate is the rate at which the corrector receives the signal. Closed loop bandwidth or system bandwidth is the maximum temporal frequency at which the adaptive optics corrects the wave-front. There exists a time delay between wave-front sensing and correction (exposure, readout from CCD, estimation of drive signals, time taken for the deformable mirror to settle). A rule of thumb is that Closed-Loop Bandwidth = 1/(π × time delay). Another rule of thumb is that the closed Loop bandwidth is about 1/10 of the closed-loop update rate. (Keller, von der Lühe, email communication). Based on these conventions, the closed-loop bandwidth of the four solar adaptive optics systems are as follows:

~ 150 Hz at VTT
~ 630 Hz at SVST/NSST
~ 25 Hz at NSO/Sac Peak (SP) (PID type control)
~127 Hz at NSO/Kitt Peak (KP)

What is the continuous range or deformation that can be handled by the system(s)?
The 97-actuator deformable mirror from Xinetics Inc. used at Sacramento Peak has a local correlation range of 2 microns, response time of 1 ms and low hysteresis. The 37 actuator membrane mirror from OkoTech used at Kitt Peak has a local correlation range of 8 microns, response time of 0.5 ms, negligible hysteresis and is able to correct for $(D/r_0) > 10$. The 19-electrode bimorph mirror from Laplacian Optics used at SVST can achieve flatness between $\lambda/40$ and $\lambda/30$ rms.

What is the extent of corrections achieved in these systems?
The 97-actuator deformable mirror from Xinetics used at Sac Peak system can correct up to 20 Zernike modes. The 19-electrode bimorph mirror from Laplacian Optics used at SVST system can correct up to 15 Zernike modes. The 37-electrode bimorph mirror from AOPTIX Technologies Inc. used at NSST can completely correct 28 KL modes and partially corrects several higher order modes. The possible upper limit is 60 KL modes. It should be noted that perfect correction of first 30 KL modes is approximately equivalent to 50 corrected modes for a mirror providing zonal correction.

What are the artifacts arising from corrections?
While using bimorph mirrors, correction for low order modes also introduces a few higher order modes; thus there is aliasing from high to low order modes. The Swedish group has tackled this issue by optimizing their bimorph mirror geometry and the control matrix (Scharmer *et al.*, 2003). In stellar adaptive optics, artifacts arise in the point spread function (PSF), basically due to the poor signal to noise ratio and the rapid change of Fried's parameter within 5 minutes (Close, http://athene.as.arizona.edu/%7Elclose/9519/˜lclose). As most of the solar adaptive optics system operate in relatively broad bandwidth such artifacts can be expected to be negligible. Severe forms of mode coupling can occur when the membrane mirror saturates. However, its effect on the performance has not been evaluated yet. (Keller, email communication).

What are the seeing conditions?
The median r_0 at NSO/SP is 8.7 cm at 500 nm. The median r_0 at NSO/KP is ~5 cm at 500 nm (Keller, e-mail communication). There is no recent reliable statistics for Tenerife, Canary Islands. However, adaptive optics has been successfully operated with r_0 in the range of 3.6 to 5 cm (Saltau, email communication; http://www.kis.uni-freiburg.de/kiswwe.html). No statistics is available for the NSST. However, occasional very good seeing conditions (r_0 =15 cm) are possible (Scharmer, email communication).

3.3 Simulation of AO

The software for the real-time correction of an adaptive optics system includes software for the measurement of local wave-front slopes (slopes over the sub-apertures in the case of SHWFS), estimation of drive signals to the deformable mirror and the optimised calibration of the control matrix. Usually, a set of voltages to be applied to the corrector is measured one by one by measuring the corresponding 2M slopes over the M sub-apertures. Such a calibration is possible only when the system components have been assembled. However, in order to evaluate the expected performance through simulations, necessary software has been developed at USO. The following is the description of the various components of the simulation.

3.3.1 Performance Evaluation of a Hybrid Imaging System:

Hybrid imaging: An adaptive optics system consists of a wave-front sensor, corrector and a control computer. Usually, it is believed that a large number of sensor elements of the order of $(D/r_0)^2$, (where D is the diameter of the telescope and r_0 is the Fried's parameter) and actuators are needed to obtain diffraction-limited performance of an adaptive optics system. However, correcting for a few Zernike modes with a small number of sensor elements or sub-apertures produces PSF with sharp core and extended wings. This essentially brings the high frequency components of the image above the noise level, enabling the use of post-detection techniques to achieve perfectly diffraction limited imaging. This is the concept of the hybrid imaging (low order adaptive optics coupled with post detection techniques).

Performance evaluation criteria: One of the ways of defining the performance of an adaptive optics system is to specify its Strehl ratio, defined in the case of ground-based astronomical imaging, as the ratio of the maximum intensity at the diffraction focus of the recorded image to the maximum intensity at the diffraction focus in the absence of atmosphere. Equivalently, it can be defined as the ratio of the volume under the transfer function of the system to that under the diffraction limited transfer function. It is a useful measure of image quality when the performance of a given telescope is compared under various seeing conditions. However, when developing an adaptive optics system to be used under given seeing conditions, one has to estimate the optimum size of the telescope that would yield maximum efficiency. In such cases, a better evaluation criterion would be the normalised Strehl-Definition defined as the ratio of the volume under the transfer function of the system to that under an infinitely large uncompensated telescope (Fried 1966). As the partial compensation produces point spread functions with sharp core and extended wings, measuring the image quality using the full width to half maximum of the image profiles can no longer be considered as a valid criterion. A better criterion that takes the wings into account would be the Strehl width (or equivalent width) defined as the width of the rectangle having area equal to the area under the profile of the point spread function. For example, the Strehl width of an Airy pattern is 1.27 λ/r_0.

At USO, we have gained sufficient expertise in speckle imaging technique over the past few years. Thus, our strategy is to evaluate the performance of a low-order adaptive optics system followed by the speckle imaging technique for achieving a resolution of about 0.2 arc-sec in imaging and about 0.4 to 0.6 arc-sec in polarimetry and spectroscopy under the typical seeing conditions ($r_0 \sim 3$ cm at visible wavelengths) of USO.

Simulations: The following is the outline of the procedure followed in our simulations –

1. Generate a series of atmospherically distorted wave-fronts.
2. Generate pupil functions representing different lenslet array geometries.
3. Estimate the slopes of the wave-front over the sub-apertures of the lenslet array.
4. Estimate the slopes of various Zernike modes over the sub-apertures.
5. Estimate the coefficients of Zernike polynomials.
6. Estimate the wave-front phase as a linear combination of various Zernike modes weighted by the estimated coefficients.
7. Subtract the estimated wave-front phase from the original wave-front phase to get the residual wave-front phase.
8. Repeat steps 3-7 for nearly 1000 realizations of the wave-fronts over the lenslet arrays.

9. Estimate: (a) Mean square residual wave-front error (b) Average point spread function, optical transfer function (c) Structure functions of the residual wave-fronts (d) Generalised Fried's parameter (e) Strehl ratio (f) Strehl width (g) Temporal power spectra of various Zernike modes.
10. Repeat steps 1-9 for telescopes of various sizes and different seeing conditions.
11. Generate a series of speckle images by convolving the point spread function of the residual wave front with a solar image obtained from the 97 cm New Swedish Solar telescope.
12. Use speckle masking code to analyze the images and estimate the contrast enhancement over adaptive–optics-corrected long exposure images and the speckle reconstruction without adaptive optics correction.

Generation of time series of distorted wave-fronts: First, a large phase screen $\varphi(x, y)$ that simulates the behavior of turbulent layer(s) is generated using classical FFT based method (McGlamery, 1976; Sridharan, 2003). A stationary, atmospherically distorted wave-front $A(x, y)$ is then obtained using the expression $A(x, y) = exp(j\ \varphi\ (x, y))$. Assuming that the turbulence pattern due to an atmospheric layer blows past the telescope aperture faster than any changes that occur in it, the large phase screen is divided into a series of small phase screens of appropriate size and a series of wave-fronts are obtained. The spatial separation between consecutive wave-fronts is determined by the time interval between them and wind speed. In simulations, the phase screen is generated using FORTRAN program and the series of wave-fronts are generated using IDL software.

Generation of lenslet arrays: We plan to use SHWFS to sense the wave front. A SHWFS consists of an array of lenses of particular shape (square or hexagonal). Usually, it is placed in the re-imaged pupil plane of the telescope. In our simulations, we replace the pupil of the telescope by a lenslet array. We generate lenslet arrays as an array of circular pupils of diameter 7-11 cm. Figure 3.1 shows some of the lenslet arrays used in the simulations. These were generated using IDL software.

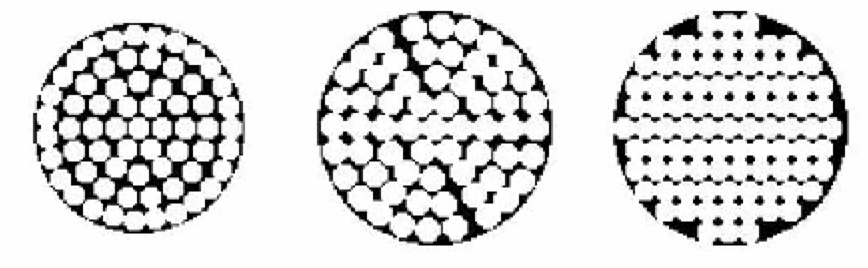
(a) (b) (c)

Figure 3.1: Various lenslet (LL) arrays used in simulations (a) LL1: D = 91 cm, d = 9 cm, No. of sub-apertures = 64 (b) LL2: D = 101 cm, d = 11 cm, No. of sub-apertures = 61 (c) LL3: D = 101 cm, d = 9 cm, No. of sub-apertures = 89. D is the diameter of the telescope; d is diameter of the sub-aperture. The white regions indicate the regions where light passes through and the black regions indicate the regions were the light is blocked.

Estimation of slopes over sub-apertures of a lenslet array: Each lens in the lenslet array produces an image of the same object (field of view) at its focal plane. The position of the images is shifted in the image plane with respect to that formed by an on axis point source imaged in the absence of the atmosphere (in other words, image formed by a perfectly plane wave-front parallel to the plane of the pupil). The extent of shift is directly proportional to the global tilt of the wave-front over the sub-aperture. We multiply the distorted wave-front by the lenslet array (one by one in sequence) and obtain the corresponding power spectrum. We estimate the shift in the position of the image from that of an on axis point source imaged in the absence of the atmosphere either by measuring the shift in the centroid of the images or by estimating the shift that *maximises* the cross-correlation between the images. The accuracy of the cross-correlation method is increased by a factor of two (half a pixel) by performing a parabolic interpolation (Sridharan, 2003).

Estimation of slopes of Zernike polynomials over sub-apertures of a lenslet array: Zernike polynomials (Born and Wolf, 1980; Noll, 1976) are ortho-normal polynomials within a circle of unit radius. As the Swedish group has demonstrated the capabilities for correcting 28 Zernike modes, we restrict our corrections only up to 28 Zernike modes. We first generate second Zernike mode corresponding to the diameter of the telescope's pupil, consider it as a distorted wave-front and estimate the slopes over the sub-apertures of the lenslet array following the procedure described in the previous section. This results in a set of 2M slopes for an M sub-sperture lenslet array. These values are ordered along a column of a 'design matrix'. The process is repeated for all the 28 Zernike modes and hence a 'design matrix' of 2M rows × 27 columns is obtained.

Estimation of the coefficients of Zernike polynomials: We estimate the pseudo inverse of the 'design matrix' using singular value decomposition method and multiply it by the slopes of the distorted wave-front measured over the sub-apertures of the lenslet array in step 3 of Simulations (Section 3.3.1) to get the coefficients of 27 Zernike modes. Z1 being piston term, is removed separately.

Estimation of the wave-front /residual wave front phase: Having determined the coefficient of the low order Zernike modes, we estimate the distorted wave-front as a linear combination of Zernike polynomials, weighted by the corresponding coefficients. A residual wave-front phase is obtained by subtracting the estimated phase from the original phase.

Results: As of now, there are no reliable statistics for r_0 at Udaipur except for a few recent measurements (Sridharan, 2002; Dashora, 2003). The measured values lie in the range of 2 to 3 cm at 656.3 nm.

We have performed the simulations for telescopes of sizes 91 cm and 101 cm for various seeing conditions (for r_0 values of 3 to 11 cm). We have also performed simulations for telescopes sizes of 27 cm, 55 cm, 75 cm and 101 cm diameter for r_0 = 3 cm assuming Kolmogorov's theory of atmospheric turbulence. The results of our simulations are given below.

Figure 3.2 shows a plot of normalized Strehl ratio R/R_{max} vs. D/r_0 for $r_0 =$ 3 cm, (solid curves) assuming ideal adaptive optics corrections of various degrees (compensated Zernike modes), N ranging from 1 to 55 obtained through our simulation. The curve with N=1 corresponds to uncompensated case. The dotted lines indicate the Strehl ratio for a given degree of compensation. For a given degree of compensation, the normalized resolution increases with increase in D/r_0, reaches a maximum and then decreases. Assuming that perfect compensation is possible up to N=28 Zernike modes (a fact, already proven by the Swedish group), a maximum Normalized Strehl ratio of about 85 and Strehl ratio of 0.43 are obtained for D/ r_0~15.

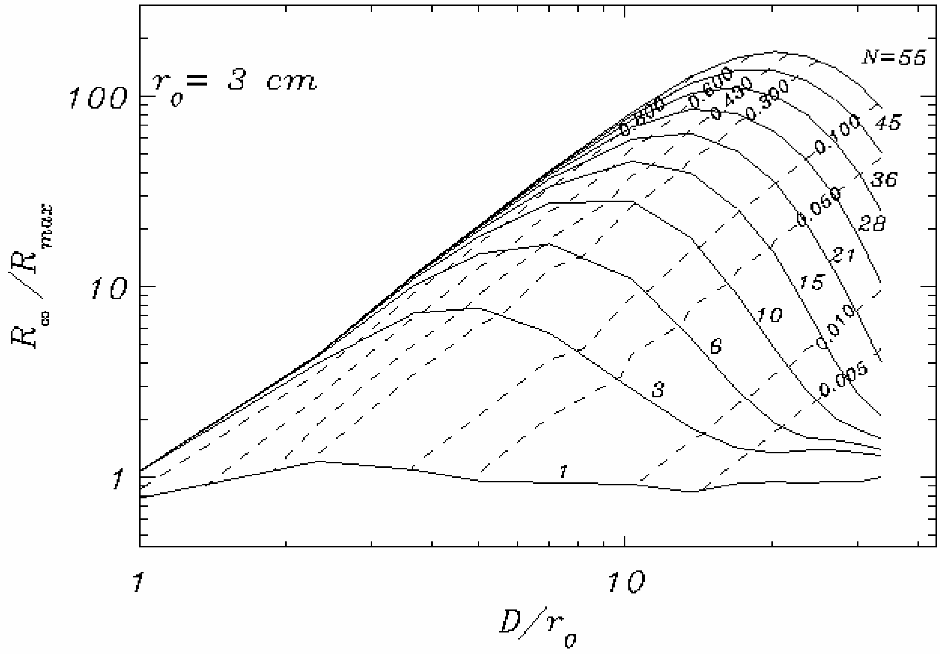

Figure 3.2: Plot of R_∞/R_{max} vs. D/r_0 for r_0 = 3 cm and for various values of order of compensation N. (solid curves). R_∞/R_{max} represents performance of the system relative to the uncompensated (without adaptive optics correction) system. The dotted lines indicate contours of constant Strehl ratio.

This indicates that an optimum diameter should be around 22 cm with a 50 % efficiency factor for real systems. For a Strehl ratio of 0.1, D/r_0=23 (from the Figure 3.2) the optimum diameter would be (23×3×0.5) about 35 cm. Thus, we conclude that a telescope of size 25-30 cm would produce diffraction limited images just with adaptive optics alone, provided the required system bandwidth is met with.

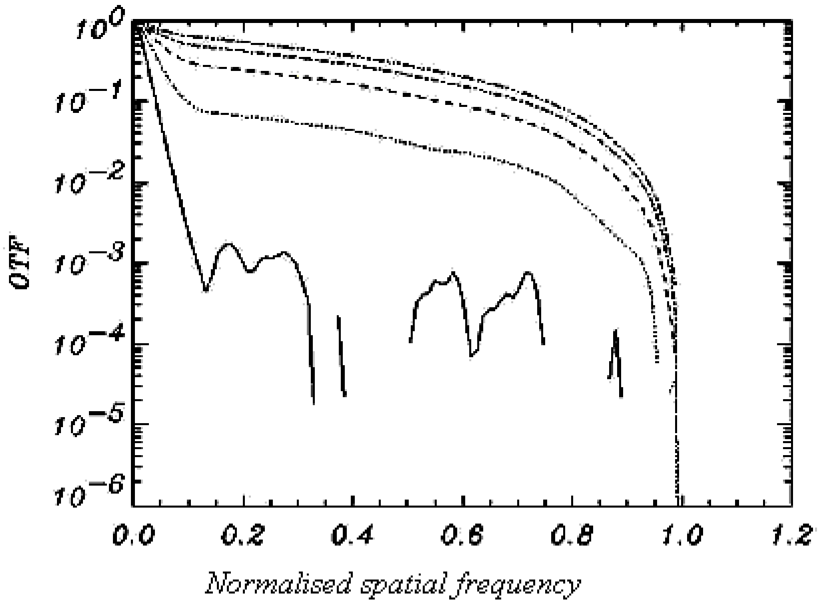

Figure 3.3: OTF after correcting for 28 Zernike modes for a telescope of diameter 91 cm and r_0 = 3 cm (continuous line), 5 cm (dotted line), 7 cm (dashed line), 9 cm (dash-dot line) and 11 cm (dash-dot-dot-dot line)

Figure 3.3 shows the OTF of adaptive optics corrected images on a logarithmic scale for various r_0 after correcting for 28 Zernike modes (radial order 6) with lenslet array LL1 (*D* = 91 cm). We find that even after correcting for 28 Zernike modes, the OTF corresponding to r_0 = 3 cm (continuous line) contains values less than 10^{-6}. The dotted curve represents OTF for r_0 = 5 cm; the dashed, dash-dot, dash-dot-dot-dot curves represent OTF for r_0 = 7, 9, 11 cm respectively.

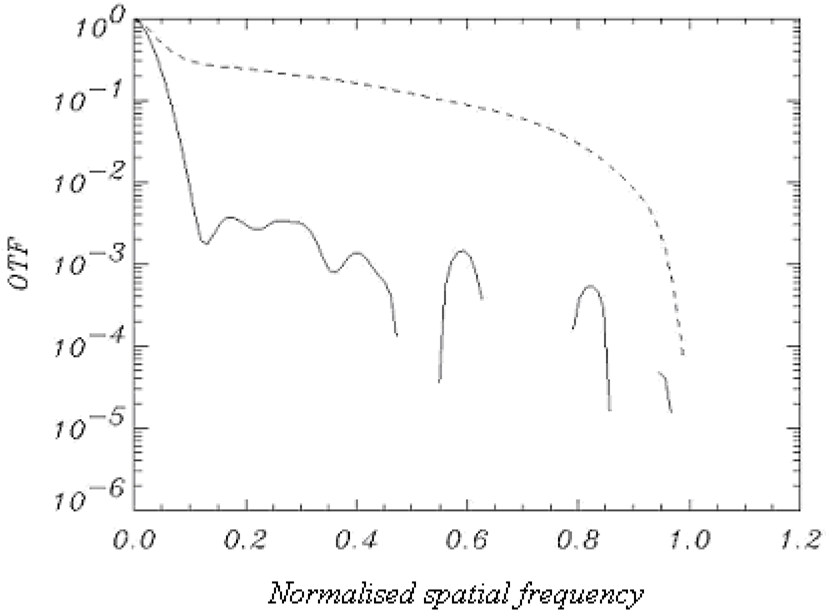

Figure 3.4: OTF for a telescope of diameter D = 91 cm and r_0 = 7 cm before and after adaptive optics correction (solid and dashed lines respectively) . The order of compensation N = 28.

Figure 3.4 represents the OTF for r_0 = 7 cm for uncompensated case (lower curve) and after compensating for 28 Zernike terms (upper curve) with lenslet array LL1.

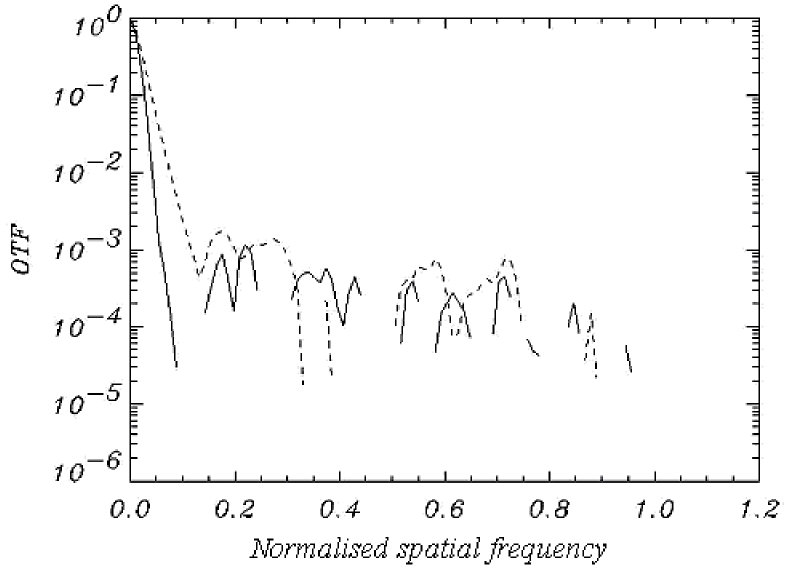

Figure 3.5: OTF for a telescope of diameter D = 91 cm and r_0 = 3 cm before and after adaptive optics correction (solid and dashed lines respectively). The order of compensation N = 28.

Figure 3.5 represents a similar plot for r_0 = 3 cm. We find that there is only marginal improvement in the OTF even after correcting for 28 Zernike modes.

Figure 3.6 represents the point-spread functions (in reversed contrast) for r_0 = 3 cm, D = 91 cm, d = 9 cm under various degrees of corrections (N= 1, 3, 6, (top row, from left to right), 10, 15, 21 (middle row), 28, 36, 45 (bottom row) respectively). We start seeing a faint core (here appearing as darkest dots) only after correcting for 21 Zernike modes. Even after correcting 55 modes, there is an extended halo. Figure 3.7 represents the point-spread functions (in reversed contrast) for r_0 = 5 cm, D = 91 cm, d = 9 cm under various degrees of compensations. Comparing this with Figure 3.6, we find that there is a substantial gain in the core intensity (here appearing as darkest dots) even with a slight improvement in r_0 for various degrees of compensation.

Figure 3.6: PSFs obtained after adaptive optics compensation of orders N = 1, 3, 6, 10, 15, 21, 28, 36, and 45 (from top left to bottom right) for r_0 = 3 cm and D = 91 cm are shown in reversed contrast. Each image occupies a segment which is 10.8×10.8 arc-sec^2 and has an image-scale of 0.085 arc-sec per pixel.

We convolved a portion of a G-band image obtained from the 97 cm New Swedish Solar Telescope with the long exposure point-spread functions obtained after various degrees of adaptive optics compensation. Figures 3.8 represents the adaptive optics corrected images for D = 91 cm, d = 9 cm and r_0 = 3 cm for N = 1, 3, 6 (top row), 10, 15, 21 (middle row), 28, 36, 45 (bottom row) respectively. Figures 3.9, 3.10, 3.11 and 3.12 represent similar images for r_0 = 5, 7, 9 and 11 cm respectively. While the adaptive optics corrected images have poor quality for r_0 = 3 cm, we find remarkable improvement in the quality of images even with medium seeing conditions (r_0 = 7 cm) after correcting for 28 Zernike modes.

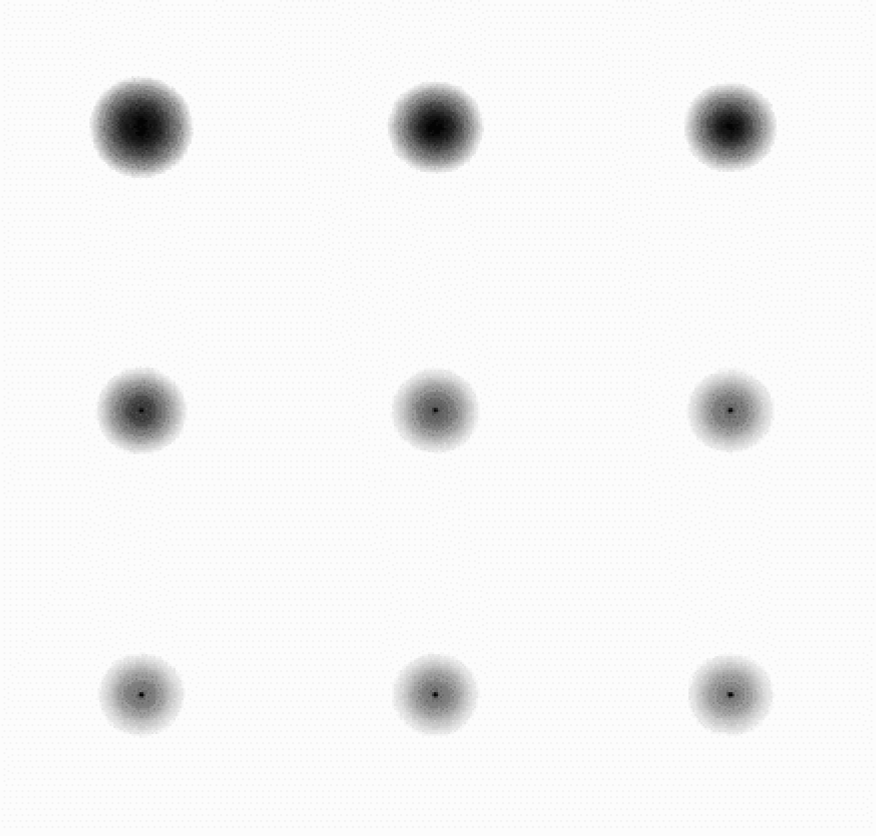

Figure 3.7: PSFs obtained after adaptive optics compensation of orders N = 1, 3, 6, 10, 15, 21, 28, 36 and 45 (from top left to bottom right) for r_0 = 5 cm and D = 91 cm are shown in reversed contrast. Each image occupies a segment of size 10.8×10.8 arc-sec^2 and has an image-scale of 0.085 arc-sec per pixel.

We estimated the average speckle transfer function from a series of adaptive optics corrected images and used it for the calibrating the average Fourier amplitudes of a series of adaptive optics corrected short exposure G-band images. The first column in Figures 3.13 and 3.14 shows the original G-band image. The second column shows adaptive optics corrected images for r_0 = 3, 5, 9, 11 cm (Figure 3.13, top to bottom) and r_0 = 4, 6, 8, 10 cm (Figure 3.14, top to bottom) respectively. The third column shows images after adaptive optics correction and speckle imaging. We find substantial improvement in the quality of the images after speckle imaging even at r_0 = 3 cm. As r_0 increases, the improvement obtained by speckle imaging decreases. This implies that under good seeing conditions, both speckle imaging and adaptive optics can produce high quality images.

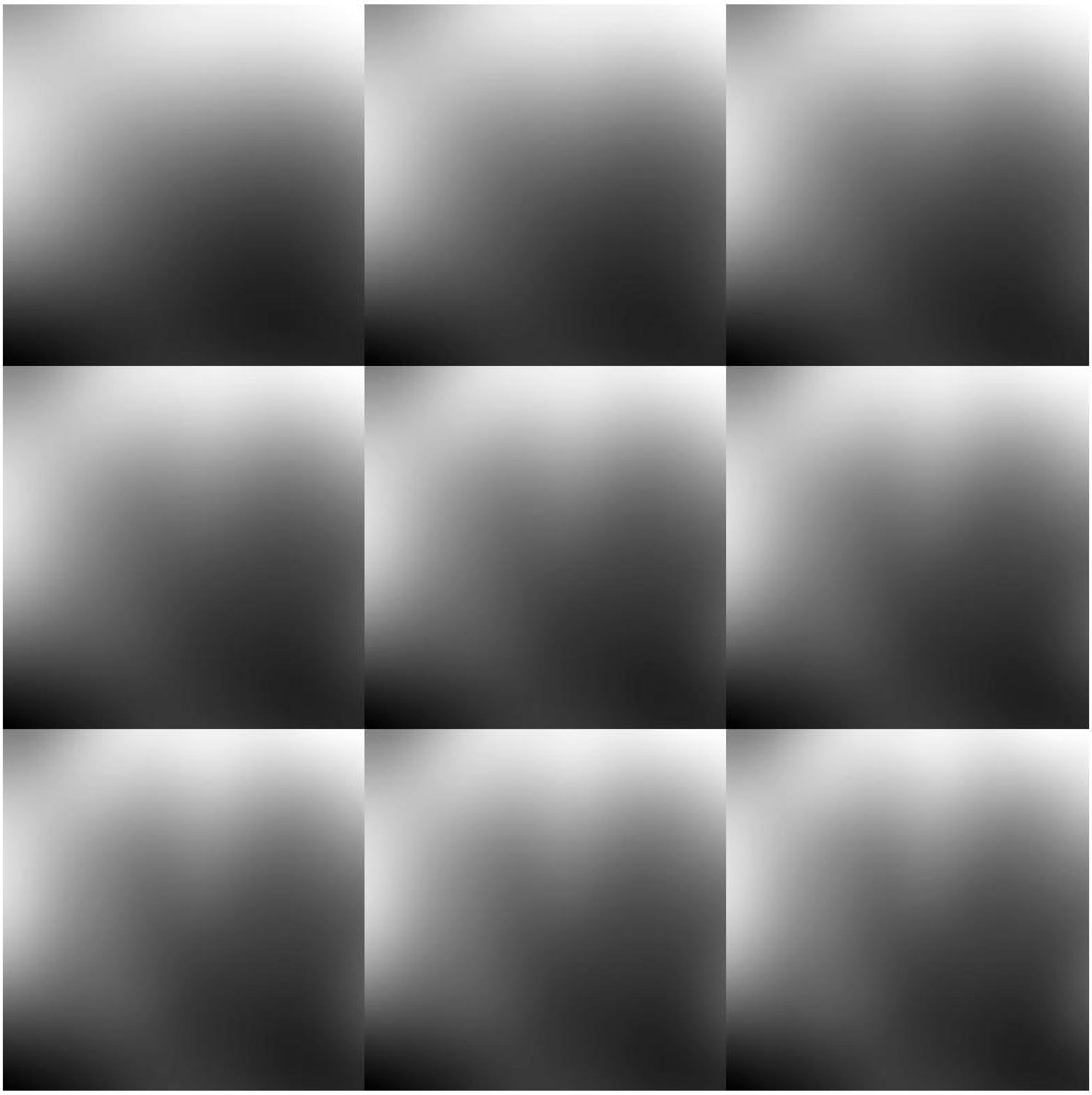

Figure 3.8: Images obtained by simulation after compensating with adaptive optics for orders N = 1, 3, 6, 10, 15, 21, 28, 36 and 45 (from top left to bottom right) for r_0 = 3 cm and D = 91 cm. The image obtained by the new 97 cm Swedish Solar Telescope after compensating with low order adaptive optics and phase diversity was used as object (input for the simulation).

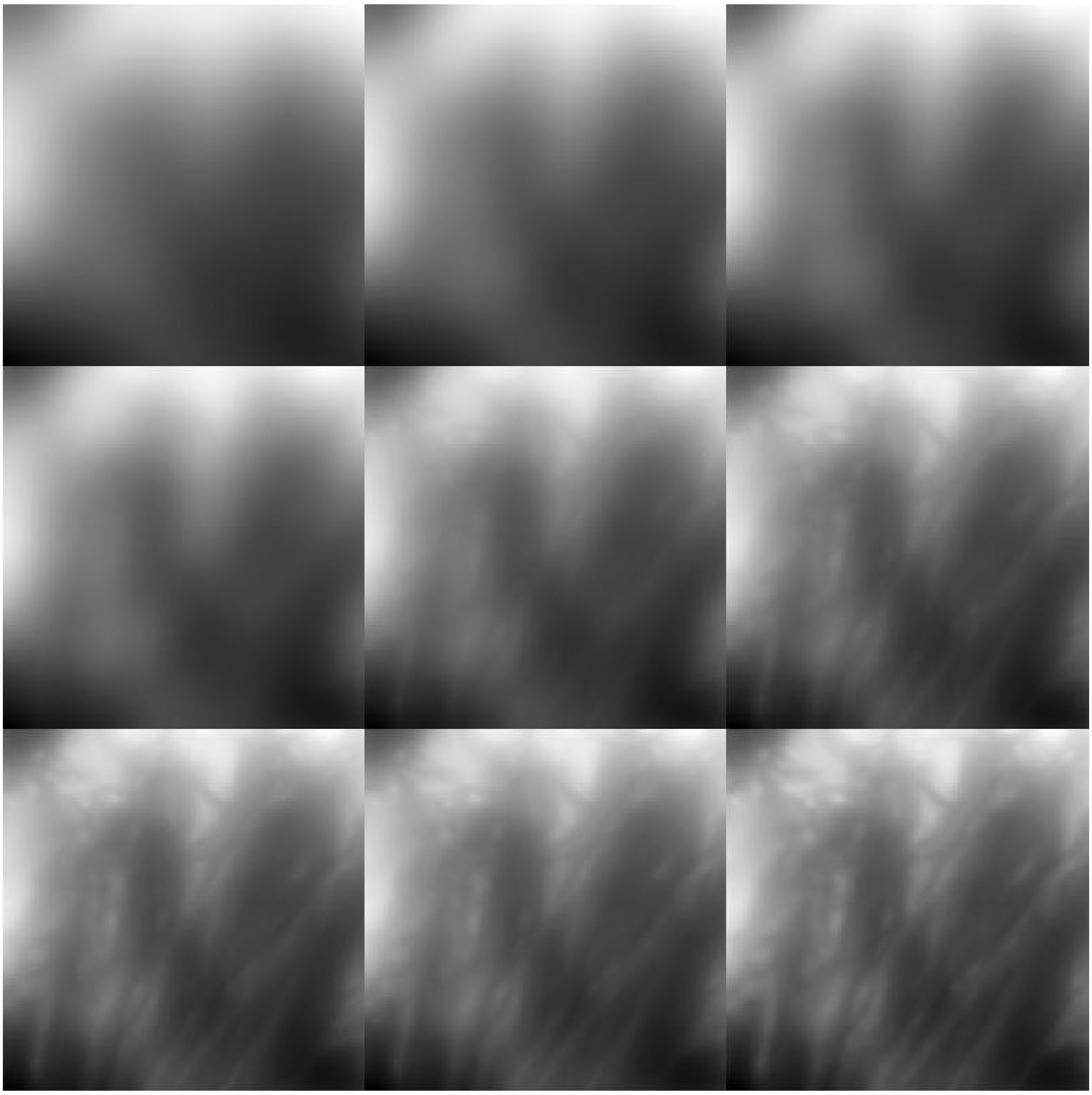

Figure 3.9: Images obtained by simulation after adaptive optics compensation for orders N = 1, 3, 6, 10, 15, 21, 28, 36 and 45 (from top left to bottom right) for r_0 = 5 cm and D = 91 cm. The image obtained by the new 97 cm Swedish Solar Telescope after compensating with adaptive optics and phase diversity was used as object (input for the simulation).

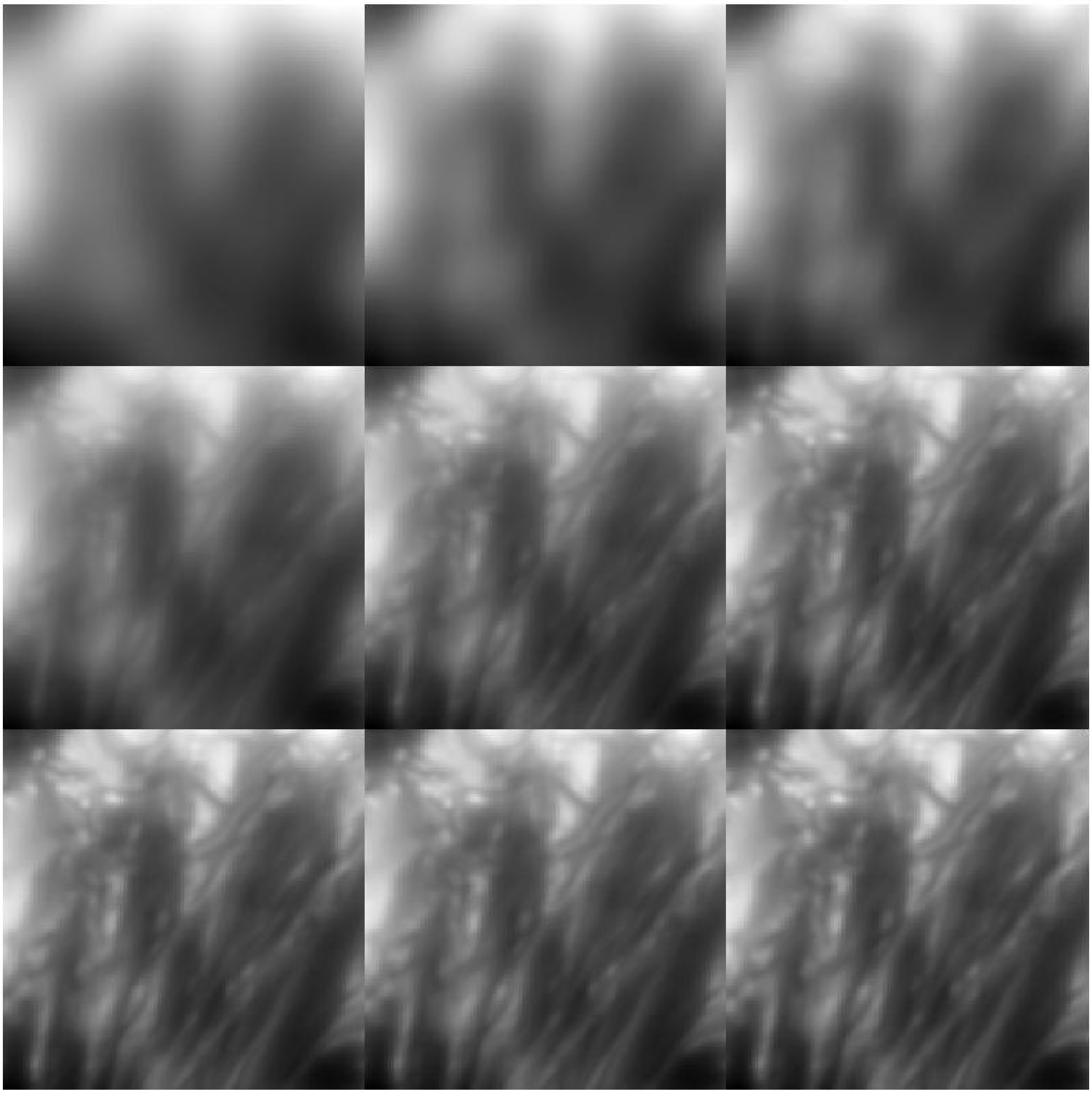

Figure 3.10: Images obtained by simulation after adaptive optics compensation for order N = 1, 3, 6, 10, 15, 21, 28, 36 and 45 (from top left to bottom right) for r_0 = 7 cm and D = 91 cm. The image obtained by the new 97 cm Swedish Solar Telescope after compensating with adaptive optics and phase diversity was used as object (input for the simulation).

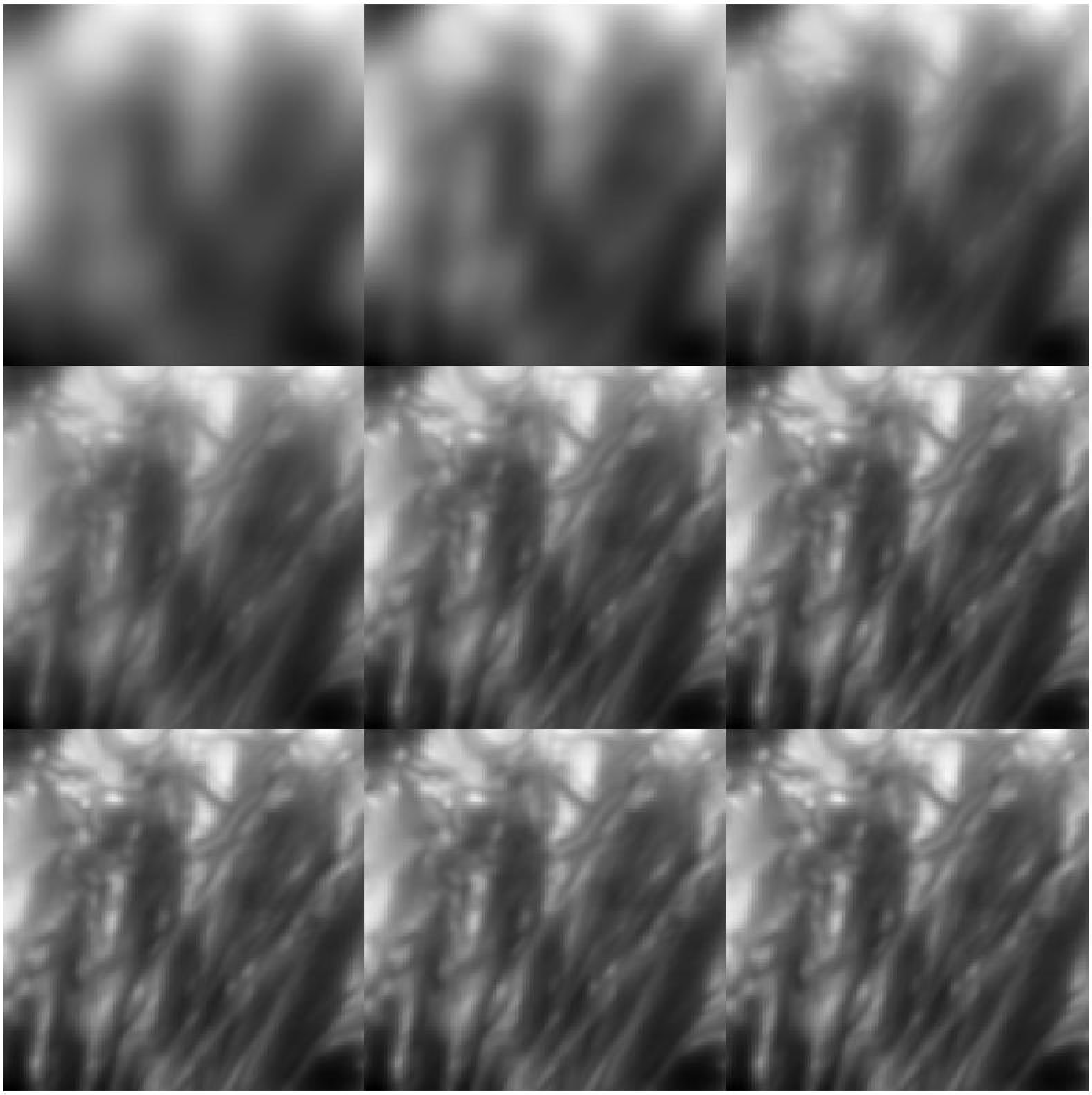

Figure 3.11: Images obtained by simulation after adaptive optics compensation for orders N = 1, 3, 6, 10, 15, 21, 28, 36 and 45 (from top left to bottom right) for r_0 = 9 cm and D = 91 cm. The image obtained by the new 97 cm Swedish Solar Telescope after compensating with adaptive optics and phase diversity was used as object (input for the simulation).

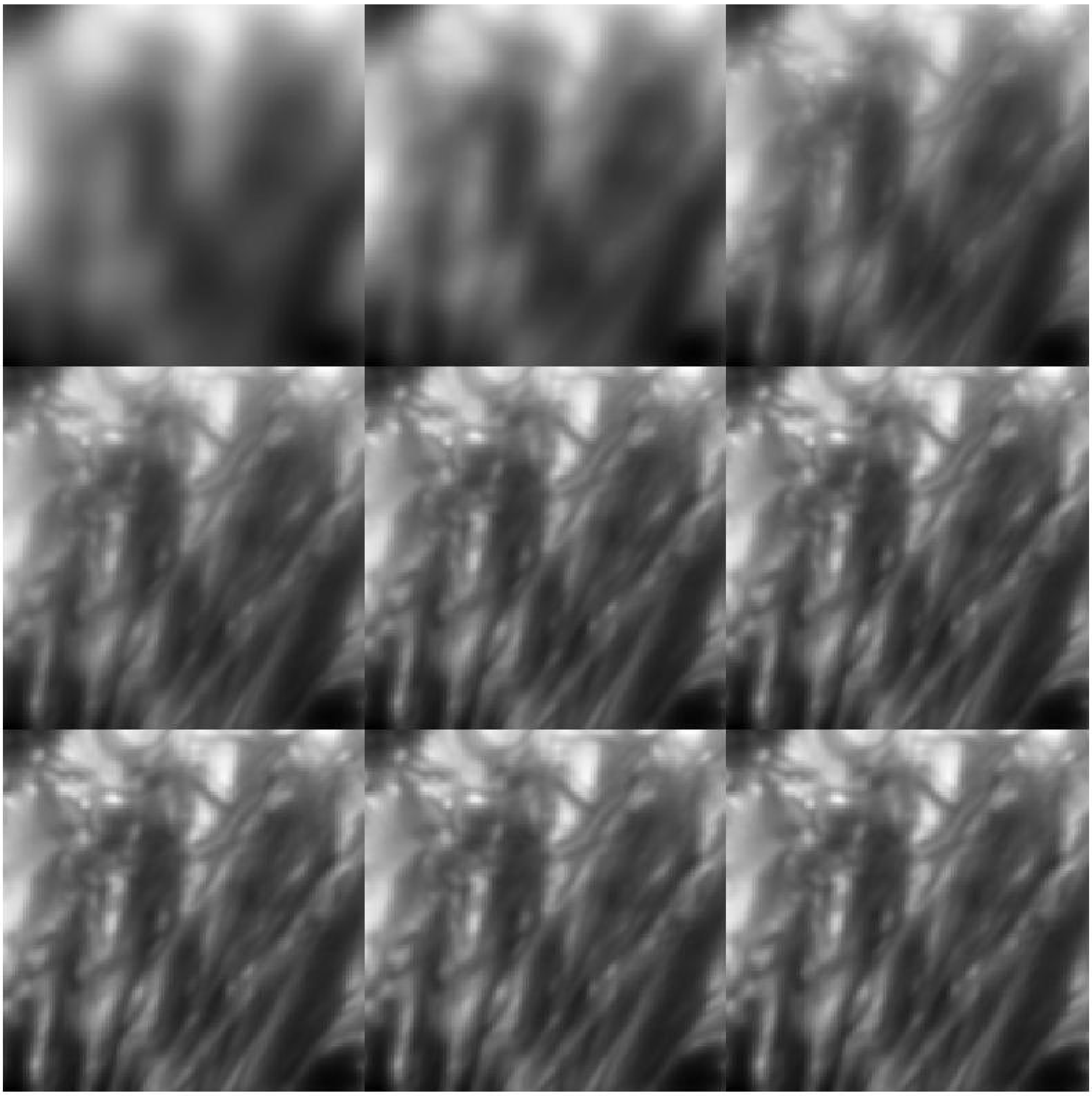

Figure 3.12: Images obtained by simulation after adaptive optics compensation for orders N = 1, 3, 6, 10, 15, 21, 28, 36 and 45 (from top left to bottom right) for r_0 = 11 cm and D = 91 cm. The image obtained by the new 97 cm Swedish Solar Telescope after compensation with adaptive optics and phase diversity was used as object (input for the simulation).

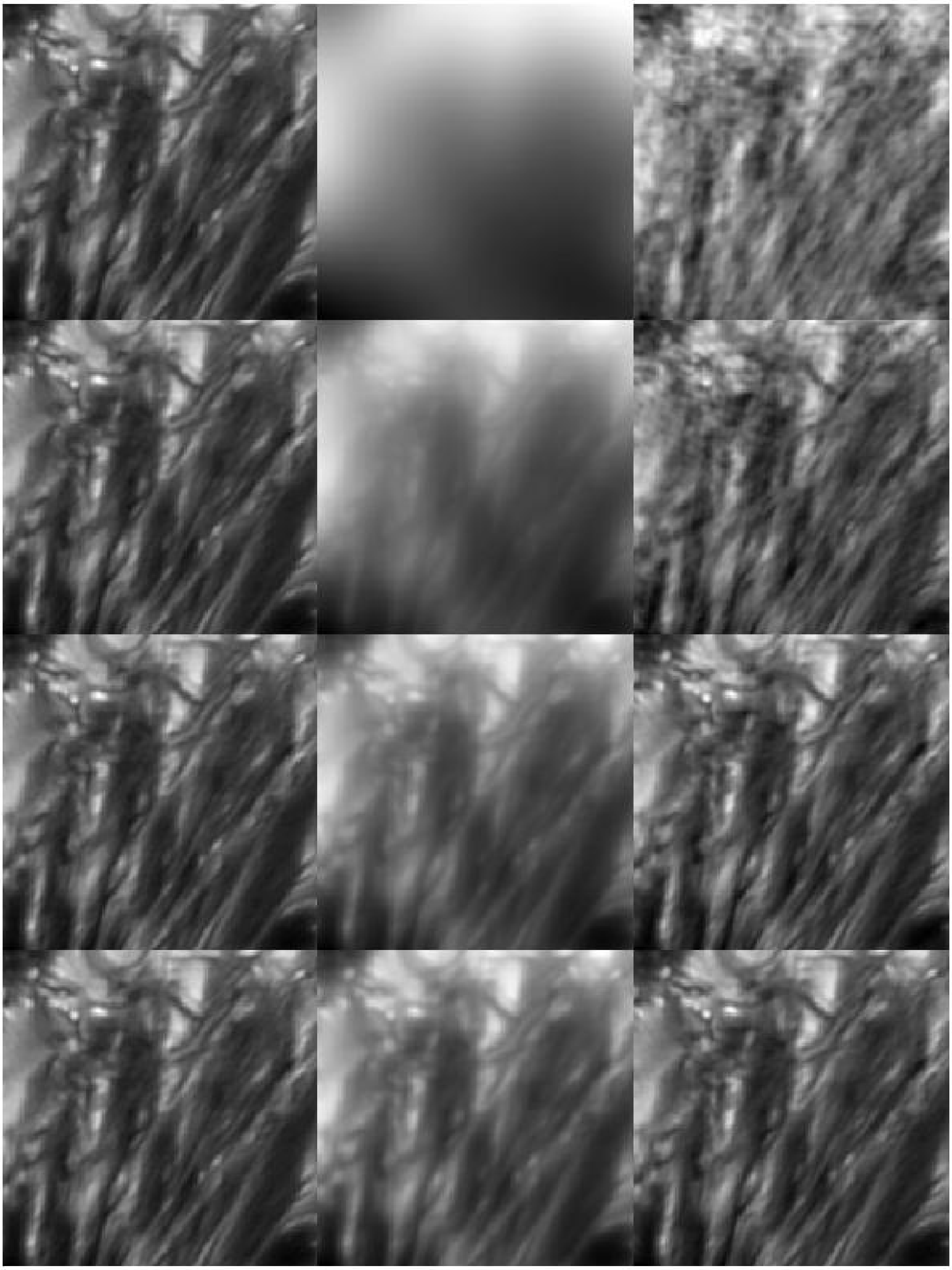

Figure 3.13: Images in first column are from the new 97 cm Swedish Solar Telescope, obtained after adaptive optics and phase diversity. The images in the middle column represent adaptive optics compensated images for r_0 = 3, 5, 7, and 11 (from top to bottom), N = 28 and D = 91 cm (obtained through simulation using those on the first column as object). The images in the last column represent results of adaptive optics compensation followed by bispectrum phase reconstruction (Speckle imaging) for the same parameters obtained by simulation using those on the first column as object.

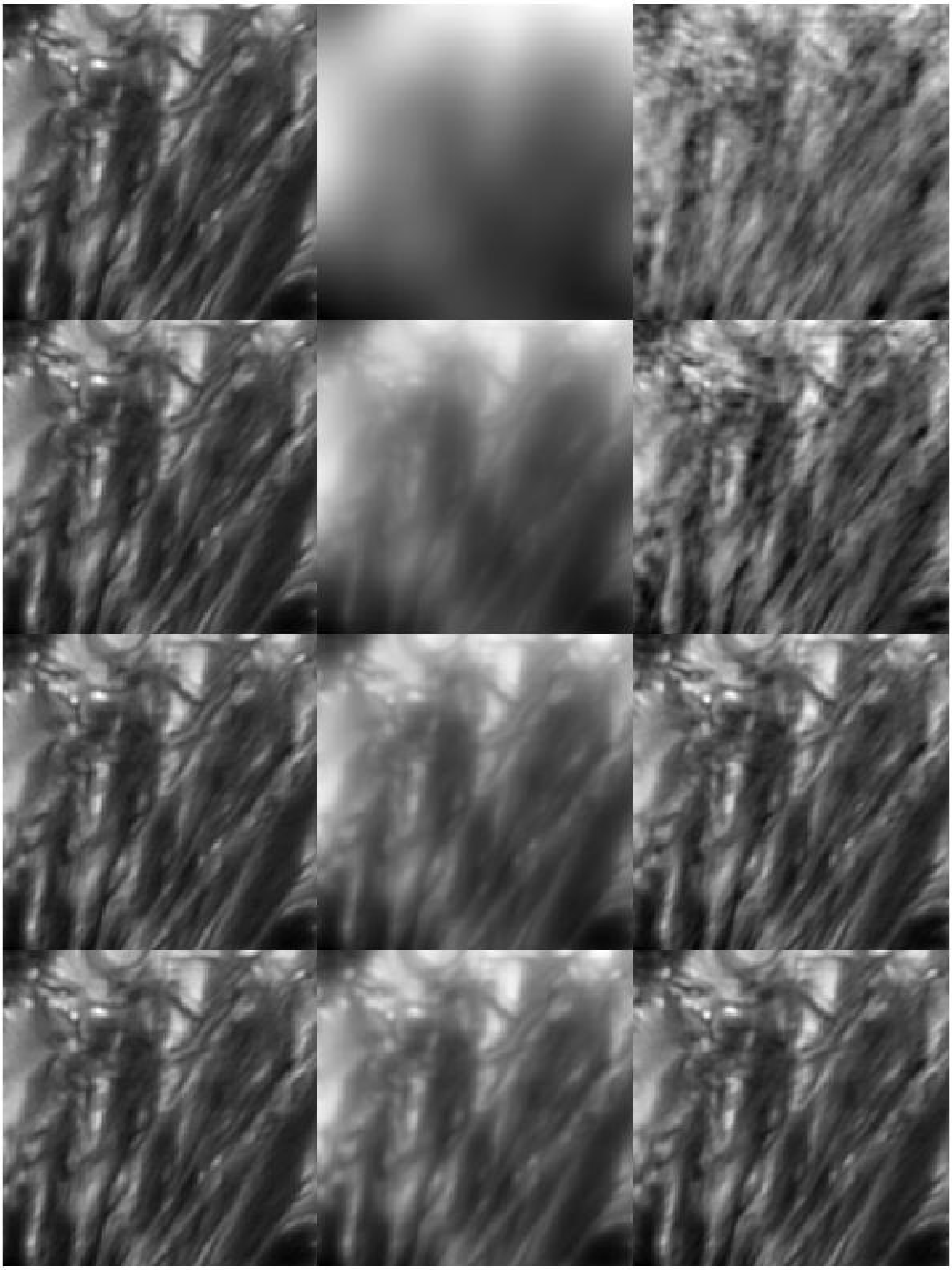

Figure 3.14: Images on the first column are from the new 97 cm Swedish Solar Telescope, obtained after adaptive optics compensation followed by phase diversity restoration. The images in the middle column represent adaptive optics compensated images for r_0 = 4, 6, 8 and 10 cm, (from top to bottom) N = 28 and D = 101 cm, obtained through simulation using the corresponding images on the first column as object. The images in the last column represent the results of adaptive optics compensation followed by bispectrum phase reconstruction (Speckle imaging) for the same parameters, obtained by simulation using the corresponding images in the first column as object.

Figures 3.15 represents speckle transfer function for r_0 = 3 (continuous curve), 5 (dotted), 7 (dash-dot), 9 (dash-dot-dot-dot) and 11 cm (long dash) after adaptive optics correction for D = 91 cm. As it is possible to extract information only up to a value of 10^{-4} to 10^{-5}, we have plotted only up to 10^{-4}. Now, frequency at which the curves cut the *x-axis* times the telescope diameter directly gives the diameter corresponding to the effective resolution. For example, for r_0 = 3 cm, the curve intersects frequency axis (of the plot) around 0.65. This implies that a resolution corresponding to an effective diameter of 0.91 × 0.65 = 0.59 m can be achieved by using speckle interferometry on a adaptive optics corrected image. As adaptive optics alone can achieve a resolution corresponding to 25-30 cm for r_0 = 3 cm, this implies that a gain of a factor two can be achieved by speckle imaging. Similarly, for r_0 = 5 cm, resolution corresponding to an effective diameter of about 70 cm can be achieved and so on. Figure 3.16 represents speckle transfer function for r_0 = 4, 6, 8, 10, and 12 cm, for D = 101 cm. It is clear that resolution corresponding to 80 cm aperture can be obtained by the hybrid imaging technique at optical wavelengths.

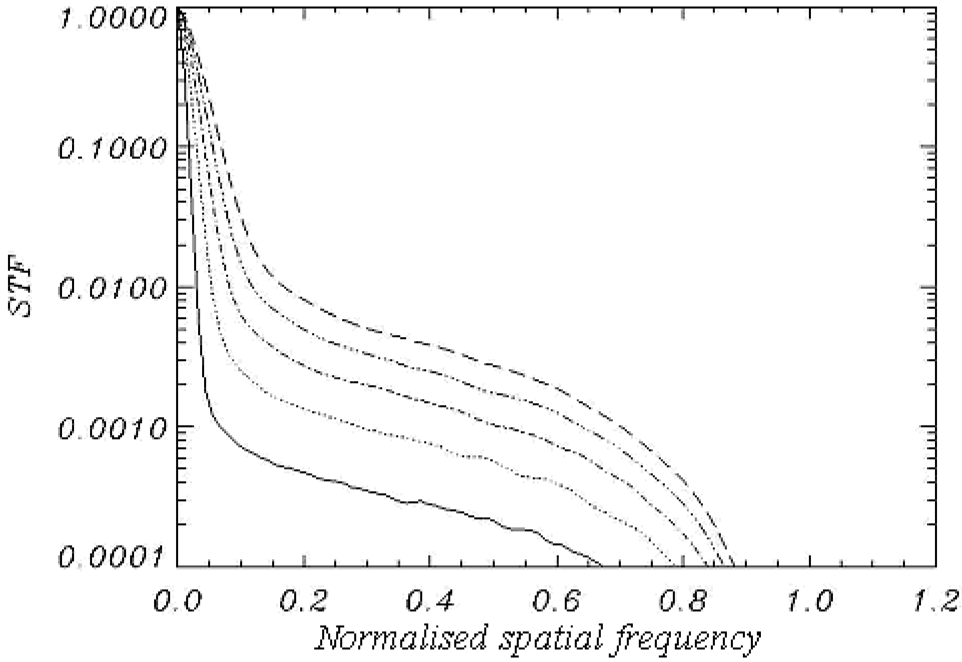

Figure 3.15: Speckle transfer function after correcting for 28 Zernike modes through adaptive optics for a telescope of diameter D = 91 cm and for r_0 = 3 cm (solid line), 5 cm (dotted line), 7 cm (dash-dot line), 9 cm (dash-dot-dot-dot line) and 11 cm (long dashed line).

From our simulations, it is very clear that under poor seeing conditions such as r_0 = 3 cm, low-order adaptive optics alone cannot produce diffraction limited imaging for a meter class telescope. One has to resort to the post-detection techniques such as phase diversity or speckle interferometry/imaging. With such a hybrid imaging strategy, one would be able to achieve a resolution equivalent to that of a 55 cm telescope at 430 nm with r_0 = 3 cm. As r_0 increases, from 3 to 5 cm, a resolution equivalent to that of an 80 cm telescope is possible. Under good seeing conditions (r_0 > 10 cm at visible wavelengths), diffraction limited performance is possible with the hybrid imaging technique.

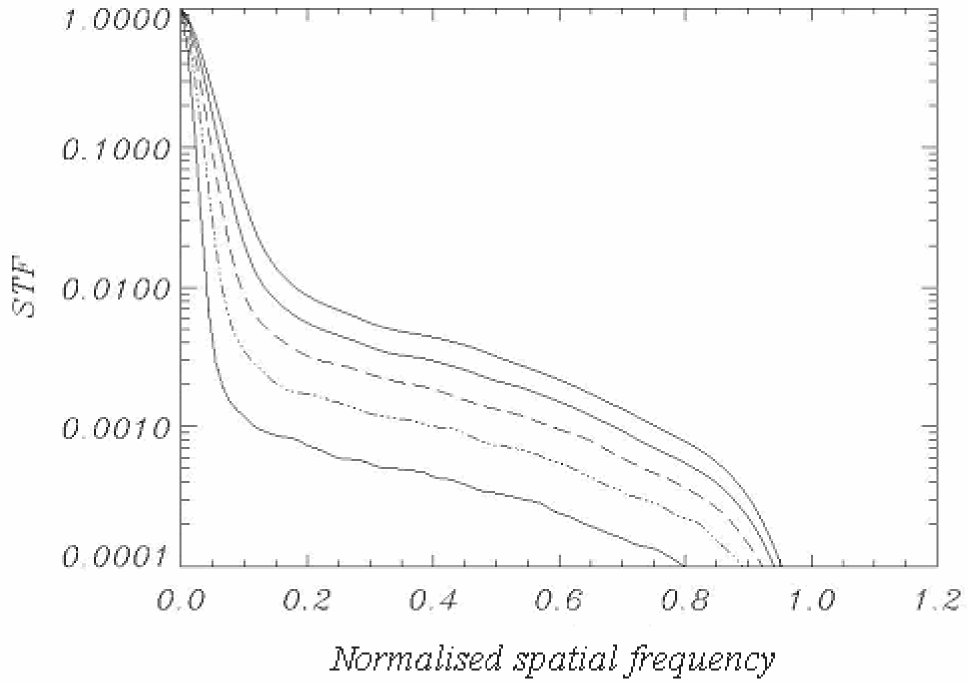

Figure 3.16: Speckle transfer function after correcting for 28 Zernike modes through adaptive optics for a telescope of diameter D = 101 cm, and for r_0 = 4 cm (solid line), 6 cm (dash-dot-dot-dot line), 8 cm (long dashed line), 10 cm (solid line) and 12 cm (uppermost solid line).

In our simulations, we used sub-apertures of sizes 7-11 cm and it appears that its size is not crucial as long as diffraction limited performance is not expected from adaptive optics alone. We assumed an average wind speed of 10 m/s and moved the phase screen by one grid point which amounts to a time delay of 1 ms between consecutive wave-fronts. We corrected each wave-front with the Zernike coefficients obtained for its previous wave-front there by giving a delay ($\Delta\tau$) of 1 ms and obtained an average (of 1024) mean square phase variance over the aperture. We repeated the calculation for different time delays. The time delay for which rms residual phase variance in correcting a finite number of Zernike modes becomes equal to that of the uncompensated terms sets the maximum allowed time-delay and hence the bandwidth through the relation $1/(\pi\Delta\tau)$. In practice, we allowed for a 10% numerical error and found that for ideal case (point by point correction), a bandwidth of 1~kHz is required for r_0 = 3 cm. This is equal to the Greenwood time delay ($\approx$ 1/3 of r_0/v), where v is the wind speed. However, in practice, with sub-apertures of finite size, probably one can afford to have a larger time-delay ($d/v > r_0$) for low order AO systems.

4. In-house Development of Prototype AO System

We plan to demonstrate adaptive optics for a 15 cm refractor available at USO following a low-cost approach demonstrated by Christoph Keller (NSO), Kitt Peak. Considering the prevailing seeing conditions at Udaipur, it would be a good exercise to see whether diffraction limited performance can be achieved for such a small aperture using adaptive optics alone. Figure 4.1 shows the optical layout of the proposed laboratory model.

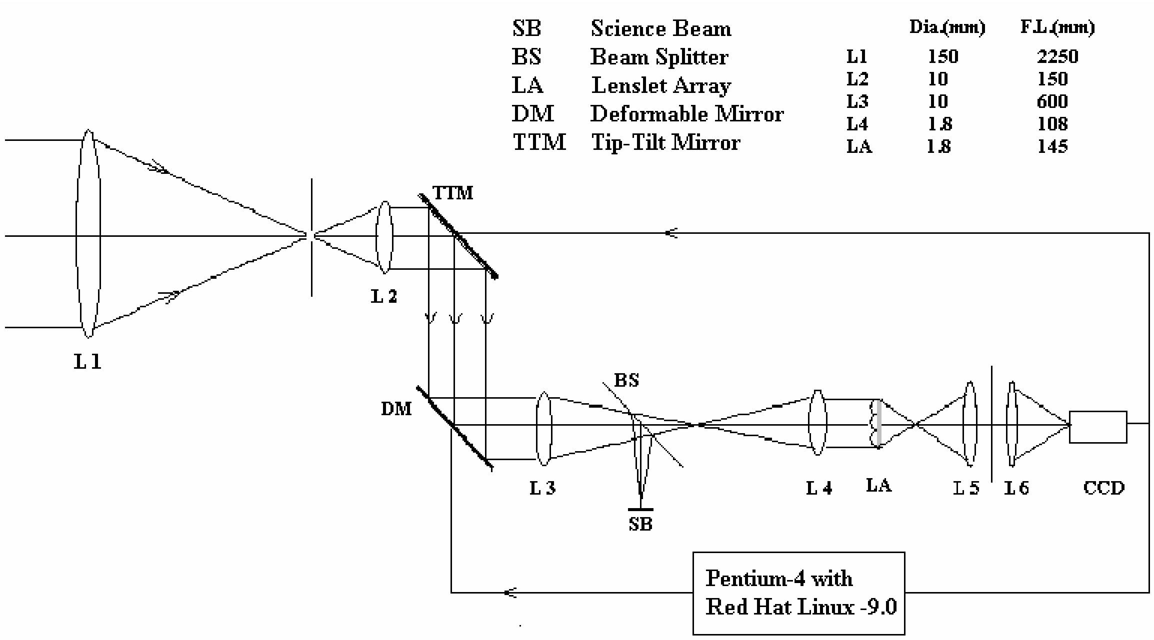

SB	Science Beam
BS	Beam Splitter
LA	Lenslet Array
DM	Deformable Mirror
TTM	Tip-Tilt Mirror

	Dia.(mm)	F.L.(mm)
L1	150	2250
L2	10	150
L3	10	600
L4	1.8	108
LA	1.8	145

Figure 4.1: Laboratory model of Adaptive Optics at USO. Indicated diameters of the lenses (beam) correspond to on axis point source.

A lens L1 of diameter 150 mm and focal length 2250 mm produces an image of the Sun at its focal plane with a scale of about 91 arc-sec per mm. A portion of this image is collimated by another lens L2. The collimated beam is first reflected by a tip-tilt mirror and then by a deformable mirror of 15 mm diameter. The deformable mirror has 37 actuators. However, we were advised (Keller, private communication) to use only the central 10 mm diameter of the deformable mirror for optimum performance. This sets the focal length of the collimating lens L2 as 150 mm. The collimated beam is brought to focus of another lens L3 after being reflected by the deformable mirror. A beam splitter kept close to the focus of L3 divides the beam into two parts. The through going beam is used for adaptive optics correction and the other beam is used for scientific purpose. It is well known that the adaptive optics corrections work well only within an iso-planatic patch whose typical value lies in the range of 5 to 10 arc-sec. In order to have such a small field of view over a practically feasible size (0.6 mm) of a field stop, the focal length of the lens L3 was chosen to be 600 mm. Thus, a square field stop (FS) of side 0.6 mm placed at the focal plane of L3 selects a field of view of about 13 arc-sec. A lens L4 collimates the beam again. The collimated beam falls on a wave-front sensor. The choice of the wave-front sensor depends on the camera available for recording the images. We decided to use a DALSA camera (DALSTAR CA-D6). This camera has a resolution of

260 × 260 pixels of size 10 × 10 µm and has been successfully used by both the KIS group and NSO group for sensing the wave-front.

An important design rule governing the selection of the lenslet array is that the size of the images formed by the lenslets should be closely equal to their physical sizes. We chose a lenslet array with 9 × 9 micro-lenses (LL), each having a diameter of 0.6 mm and focal length of 145 mm. However, we plan to use only the central 3 × 3 lenslets. Thus, the size of the collimated beam falling on the wave-front sensor is limited to a diameter of 1.8 mm for maximum throughput. This sets the focal length of L4 to 108 mm, since the focal ratio of the preceding beam is f/60. Each of the micro-lenses forms the image of the same field of view selected by the field stop with a magnification of 1.34. The size of each image is a square of side 0.81 mm and the total size of all the images is 2.43 mm. As the camera has an aperture size of 2.62 mm, the images formed by the lenslet array are slightly magnified so as to fill the CCD with the images. The filter of appropriate bandwidth is inserted in final beam.

Almost all the major components like the tip-tilt stage, deformable mirrors, detector (CCD) and their accessories were bought from the same vendors which were sourced by Keller. It is planned to use a broadband filter of 20 nm bandwidth (as is the case for KIS and NSO groups) centered at 500 nm for wave-front sensing and a narrow band filter of 1 nm in the science beam. Similar to all the existing solar adaptive optics systems, a separate tip-tilt mirror is used to reduce the demands otherwise laid on the deformable mirror. The list of components and their accessories along with the addresses of the vendors are given in Annexure II.

Current status of Adaptive Optics: In September 2003, the laboratory space required for demonstrating adaptive optics was created and Red-Hat (9.0) Linux was installed on the control computer. The optics table was installed in January 2004. The data acquisition system, which includes the DALSA camera and frame grabber, was successfully installed (in the control computer on Linux platform) and tested in February 2004. A dedicated power supply required for the operation of the camera was made in-house. The DAQ2000 board, used for controlling the tip-tilt stage was installed and tested in May 2004. The 15 cm Coude telescope was shifted from the island observatory to the main office building and used to feed the sunlight over the central 8 cm of the 15 cm doublet. A real-time control software provided by Dr. Christoph Keller, capable of correcting for the wave-front tilt alone, was modified to suit to our system (DAC board in PCI slot, device driver software itifg-8.0.8-1 version) and used for imaging the Venus on June 8, during its transit over the solar disk. At present, the control system appears to be correcting only the slow variations such as the imperfections in the tracking system. This could be due to the inability to operate the camera in memory-mapping mode using itifg-8.0.8-1. Further analysis is in progress. A few opto-mechanical components are awaited.

5. Optical Design

In this section we present the optical design, performance evaluation, tolerance analysis and thermal analysis of the telescope design. This design consists of the Imaging System (IS) and the collimating system (CS). The IS consists of primary mirror (M1) and secondary mirror (M2). The CS consists of the collimator (M3) and auxiliary optics (M4 through M8) (Figures 5.1 and 5.5). The auxiliary optics takes the beam beyond the Nasmyth focus, to a stable platform supporting all the back-end instruments.

5.1 Design Considerations

The design was governed by the following considerations.

- Clear Aperture : 50 cm
- Field of View (FOV) : 6 arc-min diameter
- System length should be as small as possible, to avoid the performance degradation due to change in optics supporting system (OSS) caused by change in temperature.
- Secondary mirror should be capable enough to take ± 32 arc-min (twice the angular size of the Sun) FOV. Otherwise the remaining light (± (32-3) arc-min) will cause damage to the system.
- There should be a provision to place a Liquid Crystal (LC) based polarization package in a collimated beam. As the maximum available size of LC retarders is 50 mm, the collimated beam size should not be more than 50 mm.
- System focus should be in-between the Primary and Secondary mirror, so that holding the Nasmyth mirror and polarization package along the pivot of the mount will be easy and overall weight will be reduced, since otherwise, unnecessary weight must be added as compensator.

5.2 Optical Parameters

Based on the aforementioned considerations, the proposed 50 cm telescope was designed using Zemax^{TM} (Optical design software). Optical parameters of the designed system are shown in Table 5.1 and schematic diagram of the designed telescope is shown in Figure 5.1.

The IS is of F-number 11 and is designed with residual rms wavefront error of 0.023λ (reference wavelength is 632.8 nm). At the focal plane of the IS, required FOV of 6 arc-min is selected. A tertiary mirror is used to get a collimated light, in which polarization package would be placed. By using a parabolic tertiary mirror, the aberrations in the IS system are reduced further. The overall system with three mirrors gives residual wavefront error of 0.0056λ. Radius of curvature of tertiary mirror is chosen in such a way that any part of reflected collimated light from it should not pass through hole of the Nasmyth mirror (Figure 5.2). Polarization package is placed in the collimated beam with online compensation (Section 11.1) for the retardation introduced by 45° reflection off the Nasmyth mirror. A heat stop would be designed to sink 225 watts (for an input flux of 1125 watts, refer Figure 8.2) of power and placed at the system focus. It has to allow only 6 arc-min field of view and remaining light (~225 watts) should be eliminated (Figure 5.2).

Silicon Carbide (SiC) has high thermal conductivity, thermal diffusivity and lightweight making it the preferred material of choice for primary, secondary and tertiary mirrors. Table 5.2 shows the properties of Silicon Carbide.

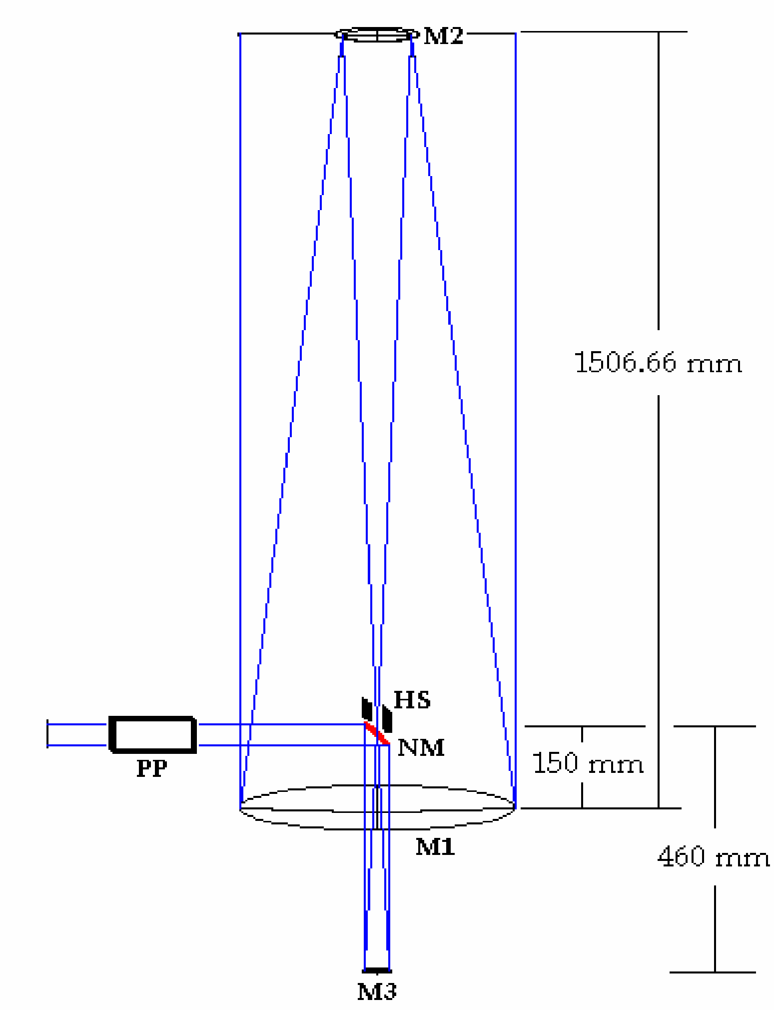

Figure 5.1: Schematic of the designed telescope, HS: Heat stop, PP: Polarization package. M1, M2 and M3 are Primary, Secondary and Tertiary mirrors. NM is the Nasmyth mirror. Polarization package (PP) will be placed in collimated beam after the Nasmyth mirror.

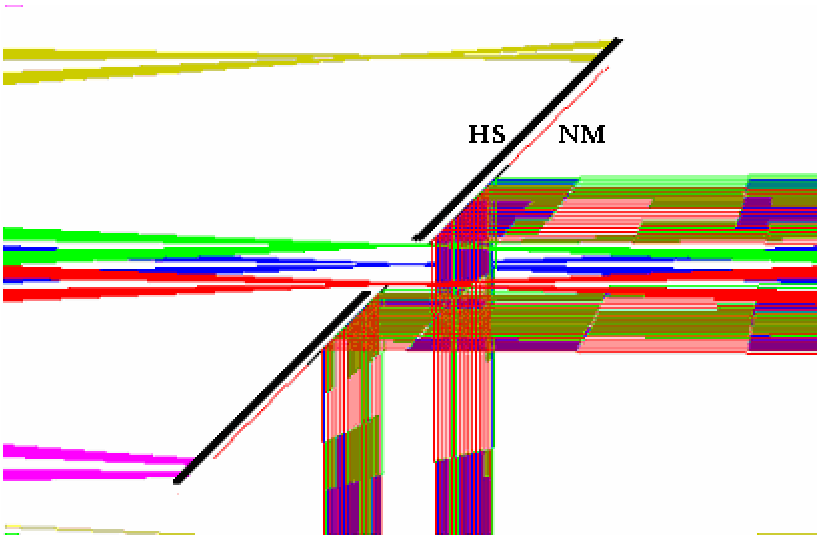

Figure 5.2: Showing enlarged view of the heat stop, allowing the rays corresponding to central 6 arc-min only. Nasmyth mirror, which is tapping the collimated beam coming from the tertiary mirror is also shown.

Table 5.1: Optical parameters of the designed telescope

Parameters	Primary mirror (Concave)	Secondary mirror (Convex)	Tertiary mirror (Concave)
Focal length	2000 mm	775.25 mm	920 mm
Clear Aperture	500 mm	152 mm	54 mm
IS F-Number	4	5.1	
Conic Constant	-1.0	-4.591864	-1.0
Material	SiC	SiC	SiC
Surface irregularity	0.025λ RMS	0.02λ RMS	0.02λ RMS

IS F-number : 11
Primary mirror bore diameter : 120 mm
Distance between Primary and Secondary mirrors : 1506.66 mm

IS focus from Secondary : 1356.680625 mm
IS focus from Primary : 149.97 mm

Image size for 6 arc-min FOV : 9.6 mm
for 32 arc-min FOV : 51.5 mm

Heat stop - Diameter: 158 mm
- Surface absorptivity : ≈ 100 %
- Sink requirement : 225 Watts

Distance between IS focus and Tertiary mirror : 460 mm

Nasmyth mirror - Diameter: 63.2 mm
- Central hole diameter: 15 mm

Table 5.2: Properties of Silicon Carbide-Chemical Vapour Deposition (CVD) (Wilson, 2001)

Property	Units	Silicon Carbide-CVD
Density	Kg/m^3	3210
Modulus of Elasticity	*Gpa*	466
Specific Heat	*J/Kg-K*	712
Specific Stiffness	$Gpa\ cm^3/g$	186
CTE	K^{-1}	2.1×10^{-6}
Thermal Conductivity	*W/m-K*	193
Thermal Diffusivity	m^2/s	84.44×10^{-6}
Thermal Insensitivity	m^2-*K/s*	40.2
Mechanical Stiffness	*J/Kg*	14.5×10^7

5. 3 Performance Evaluation

There are many ways of evaluating the performance of an optical system. The spot diagrams, Modulation Transfer function (MTF), residual wavefront error at different field angles and at different wavelengths are very useful in evaluating the performance of telescope system. Figure 5.3 (a to c) shows some of these characteristics of the designed system.

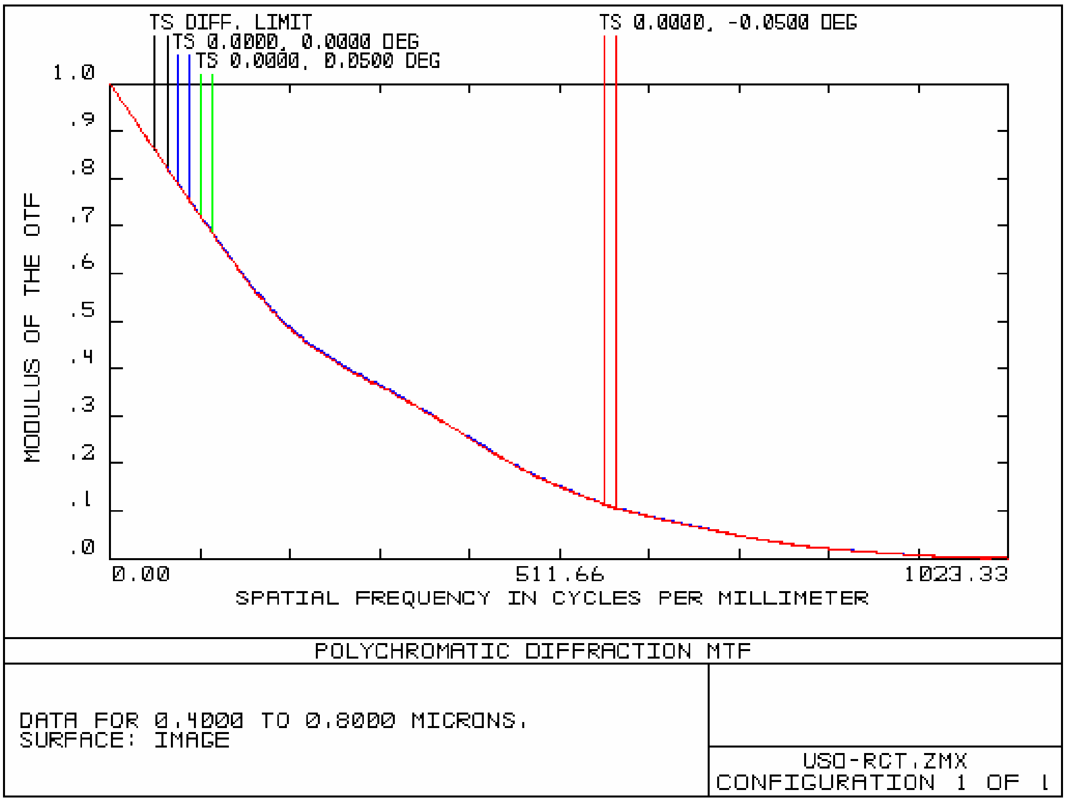

Figure 5.3a: The system performance in terms of contrast at various spatial frequencies for the field angles 0^0, + 0.05° and – 0.05°, T and S represent tangential and sagital plane respectively.

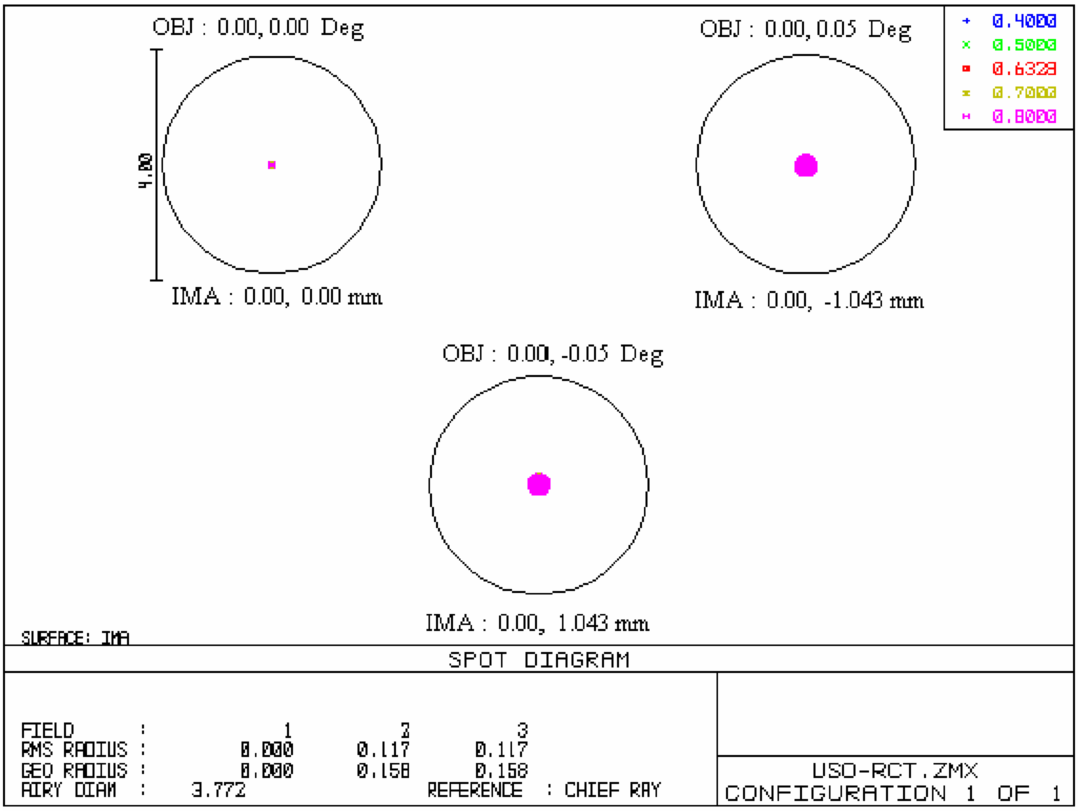

Figure 5.3b: The spot diagrams, show the system performance for the field angle 0^0, + 0.05° and – 0.05° respectively. The circle represents the airy disc size of the designed system.

In the absence of surface irregularities, with the aforementioned optical parameters, residual wavefront error will be better than 0.0056λ at 632.8 nm for 6 arc-min field of view. But polishing of mirror blanks to high accuracy is difficult, time consuming and costlier. So we assigned surface irregularity of 0.025λ to primary and 0.02λ to secondary and tertiary mirror in such a way that the combined system performance will be better than 0.0423λ.

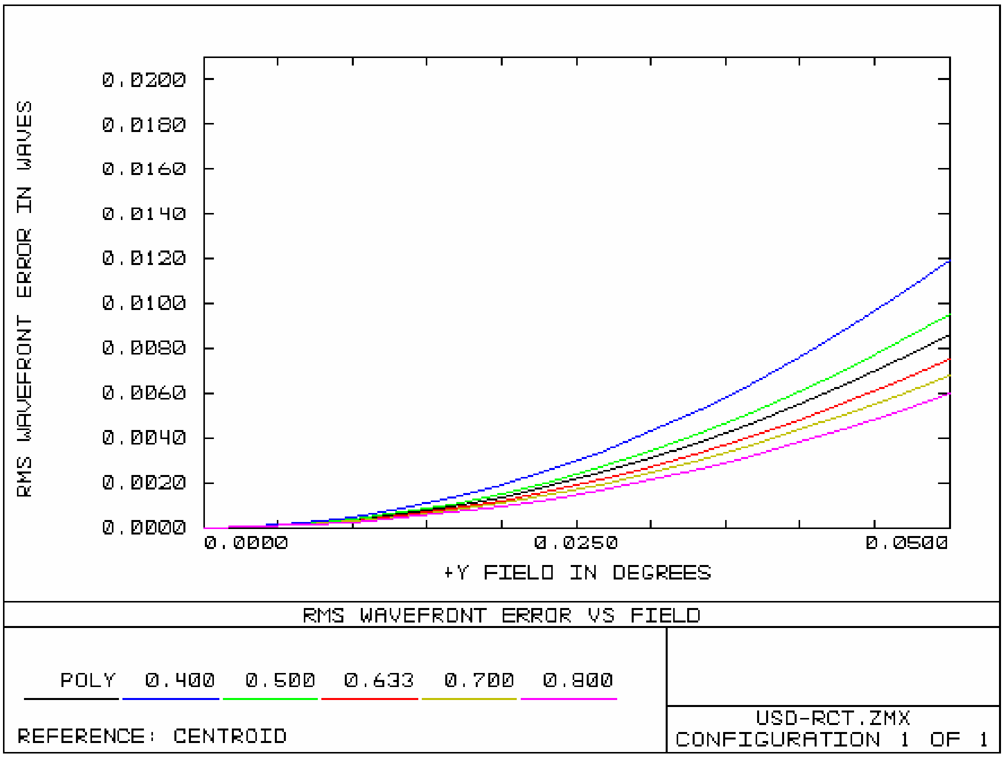

Figure 5.3c: The designed system performance in terms of RMS wave front error vs field at different wavelengths.

System performance with surface irregularities is shown in Figures 5.4 (a and b). Primary, secondary and tertiary mirror surface irregularities are fitted with first 15 Zernike polynomials and the Zernike coefficients are shown in Table 5.3.

Table 5.3: Zernike coefficients, which represent the surface irregularity of primary, secondary mirror and tertiary mirrors.

Zernike terms	Primary mirror $\times 10^{-6}$ mm	Secondary mirror $\times 10^{-6}$ mm	Tertiary mirror $\times 10^{-6}$ mm
Z2	5.00909	-3.69831	1.90568
Z3	-1.48957	-3.69138	4.60665
Z4	1.32048	-1.08602	-1.91041
Z5	-6.09216	1.22850	2.83615
Z6	-5.76670	2.45730	2.17495
Z7	-9.51590	-4.30515	-2.41988
Z8	-2.60062	2.09289	-1.21342
Z9	5.80973	-3.07006	2.28905
Z10	1.83595	-3.90618	7.22135
Z11	3.28009	-2.02164	-4.77479
Z12	7.74413	6.19985	5.15458
Z13	2.79368	3.06756	1.05758
Z14	-2.35575	-6.72729	6.09131
Z15	-5.92968	-2.49569	5.01299

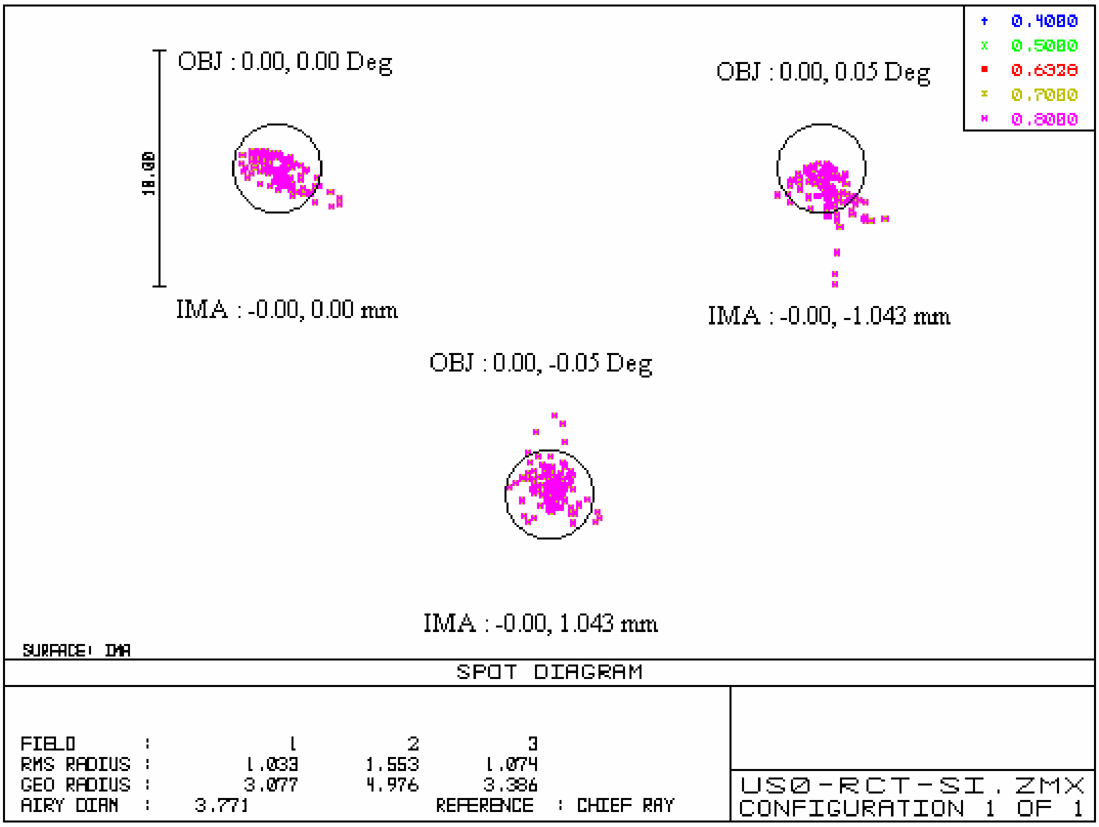

Figure 5.4a: Same as Figure 5.3b but in the presence of surface irregularity with surface parameters mentioned in Table 5.1 Though it shows the light spilling out of the airy disc, the rms spot radius is less than the airy disc radius.

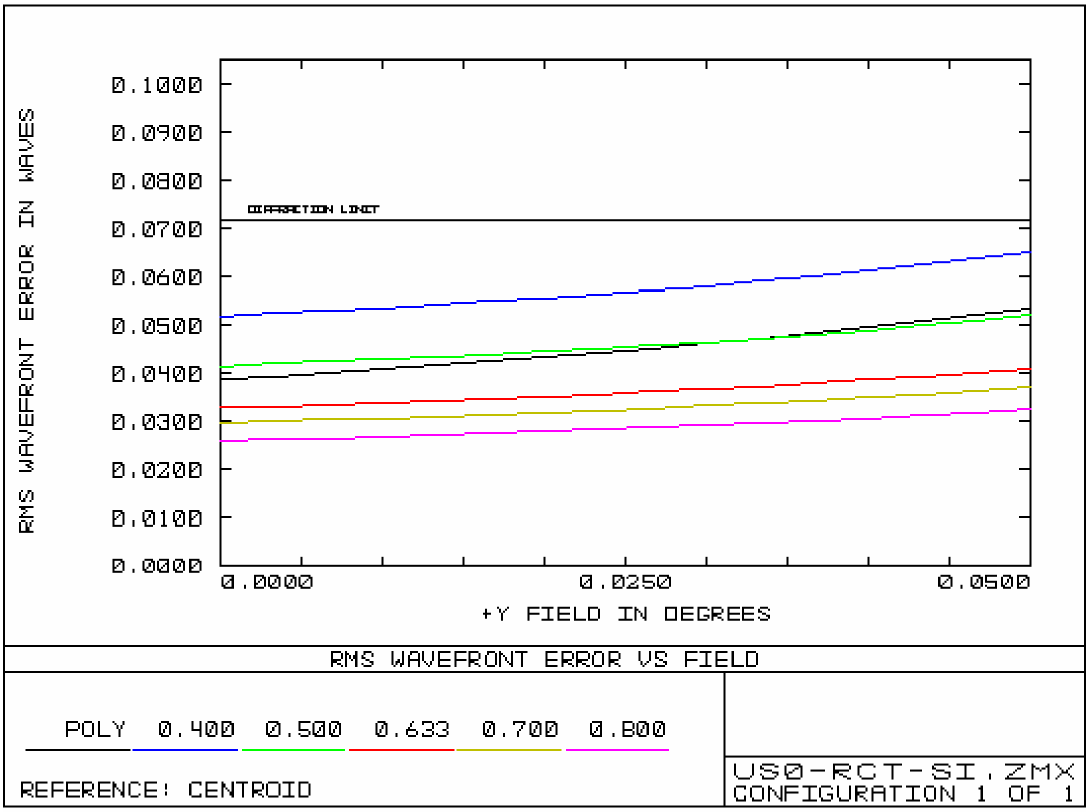

Figure 5.4b: Same as Figure 5.3c but with the surface irregularity with surface parameters mentioned in Table 5.1. It is clear that the system performance is within the diffraction limitation (0.072λ).

5.4 Tolerance Analysis

A set of generally accepted tolerances by manufacturers are shown in Table 5.4. Based on this, the tolerances on various parameters of the designed system are adjusted and their effect on the system performance is studied.

Table 5.4: Set of accepted tolerances (adapted from Shannon, 1997)

Quality level	Thickness (mm)	Radius (%)	Decenter (mm)	Tilt (arc-sec)	Irregularity (fringes)	Residual-wavefront (λ)
Commercial	0.1	1.0	0.1	60	1	0.25 rms
Precision	0.01	0.1	0.01	10	0.25	0.10 rms
High—Precision	0.001	0.01	0.001	1	< 0.1	<0.07 rms

Table 5.5: Tolerances for the designed system

	Min. (mm)	Δ RMS (waves)	Max. (mm)	Δ RMS (waves)
Primary mirror:				
Radius of curvature	-4.00	0.0233	4.0	0.0322
Decentration-x	-0.10	0.0083	0.10	0.0084
Decentration-y	-0.10	0.0084	0.10	0.0084
Conic constant	-0.0015	0.0113	0.003	0.0153
Secondary mirror:				
Radius of curvature	-3.0	0.0139	3.0	0.0059
Decentration-x	-0.10	0.0078	0.10	0.0078
Decentration-y	-0.10	0.0078	0.25	0.0078
Tilt-x (degrees)	-0.01	0.0083	0.01	0.0083
Tilt-y (degrees)	-0.01	0.0082	0.01	0.0082
Conic constant	-0.04	0.0116	0.03	0.0146
Tertiary mirror:				
Decentration-x	-0.5	0.0010	0.5	0.0010
Decentration-y	-0.5	0.00135	0.5	0.00135
Tilt-x (degrees)	-0.05	0.00089	0.05	0.00089
Tilt-y (degrees)	-0.05	0.00058	0.02	0.00058
Conic constant	-0.03	0.00098	0.03	-0.00087
Distance between Primary and Secondary	-1.0	0.0158	1.5	0.0157

These tolerances affect the system performance in two ways: one is on the IS and the other is on the complete system. In IS, the image plane position changes by ±15 mm and residual rms wavefront error will be changed to 0.0716λ. In complete system, the residual rms wavefront error will be changed to 0.0818λ.

By comparing the values in the Table 5.4 with those in the Table 5.5 the designed tolerances are expected to be achieved.

5.5 Thermal Analysis

Assumptions:

- Primary, secondary and tertiary mirrors are fabricated with Silicon-Carbide
- Trusses are made with aluminium
- Rapid thermalization of the mirror
- Mirrors and trusses are manufactured at a temperature of 20ºC and pressure of 1 atmosphere (1 bar).

Zemax estimates the change in radius of curvature and change in length of the trusses using coefficient of thermal expansion of the aforesaid materials. These changes ultimately change the image plane position, and cause the degradation of the system performance in the image plane. In order to bring it back to original performance, either image plane or distance between primary and secondary has to be adjusted. Shifting the image plane position causes changes in the following optics, so it is better to change the distance between primary and secondary by moving the secondary mirror along the axis.

Change in secondary position is estimated (Table 5.6) such that the image plane position will be same at any temperature. This tells the required range of axial motion of secondary tip-tilt system.

Coefficient of Thermal expansion (CTE) of SiC-CVD = $2.1 \times 10^{-6} K^{-1}$
Coefficient of Thermal expansion (CTE) of Aluminium = $22 \times 10^{-6} K^{-1}$

Change in radius of curvature of tertiary mirror and change in length of the trusses holding it with respect to temperature will change the collimation. By selecting the tertiary mirror material with CTE less than CTE of the trusses' material, we can avoid the collimated light becoming a diverging light beam. A little variation in the collimated light will not effect the polarization as long as angle of the convergent light is within the acceptance angle of polarization package (2º, refer annexure IV).

Assume

- Change in temperature is 30ºC
- Truss length that is holding the tertiary mirror is 460 mm
- Change in radius of curvature of tertiary mirror is 0.05796 mm,
- Change in focal length of tertiary mirror is 0.02898 mm
- Change in length of truss is 0.3036 mm

Then, the tertiary mirror moves 0.27462 mm away from its focus. As a result, the emergent beam converges to an image at a distance of 861992 mm instead of at infinity. This is 2 orders of magnitude greater than the final desired focal length. Therefore, no special care needs to be taken for the thermal expansion of the truss holding the tertiary mirror.

Thermal considerations: Optics

To avoid mirror "seeing", the temperature of the primary mirror surface must be maintained within 0.5ºC of the ambient temperature. For a site like Udaipur, the ambient temperature changes by 30º during summer. However, glass substrates of large size do not respond quickly enough to changing external thermal conditions. As a result, the mirror will always be tending to approach thermal equilibrium but never reach thermal equilibrium. Substrates made of SiC will quickly attain thermal equilibrium. Thus, we chose SiC.

Table 5.6: Thermal analysis of the designed optical system

Change in Temparature ^{o}C	Change (mm) in				Axial Motion needed
	Radius of Curvature		OSS length	Image plane Position	
	Primary	Secondary			
5	0.042	-0.0162803	0.1657326	-1.1194621	-0.1480290
10	0.084	-0.0324605	0.3314652	-2.2389242	-0.2960580
15	0.126	-0.0488408	0.4971978	-3.2583863	-0.4440869
20	0.168	-0.0651210	0.6629304	-4.4778484	-0.5921158
25	0.210	-0.0814013	0.8286630	-5.5973105	-0.7401447
30	0.252	-0.0976815	0.9943956	-6.7167727	-0.8881736

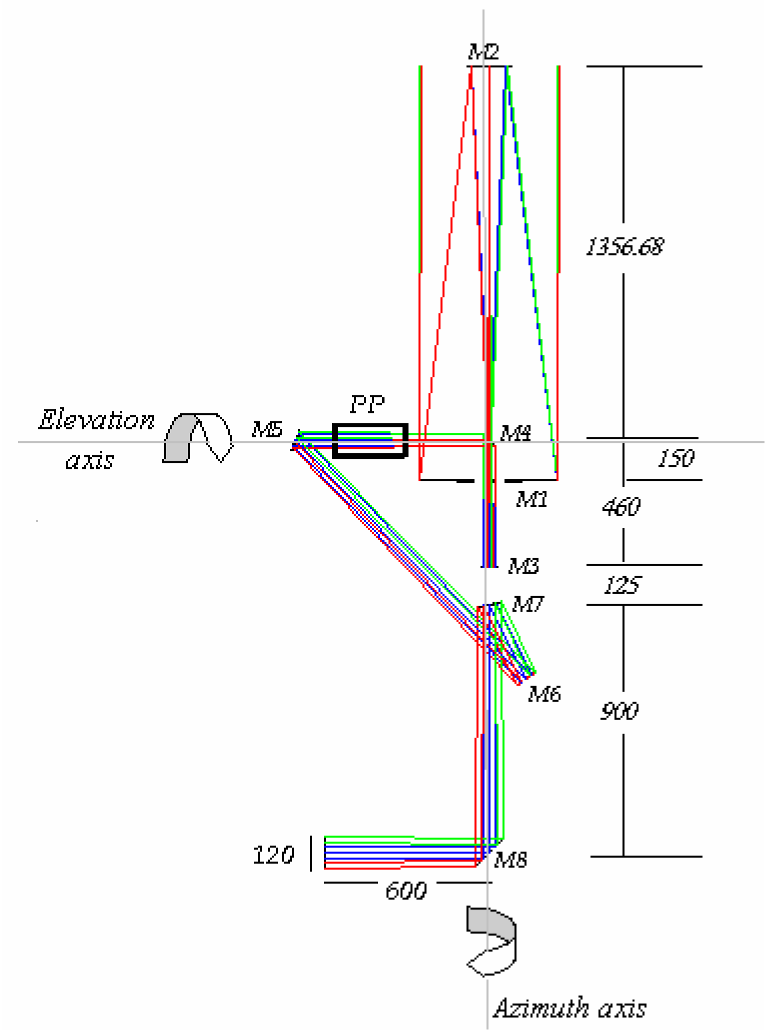

Figure 5.5: Schematic of the complete optical design. After the Nasmyth mirror(M4), beam is sent to the stable platform using the mirrors M5, M6, M7 and M8. PP is polarization package.

Thermal considerations: Optical support system

To avoid turbulence generated by the temperature difference between trusses and ambient air, the trusses must be maintained at the ambient-air’s temperature. If the trusses are designed to remain on planes parallel to the optical axis of the telescope, then they are not liable to be directly heated by solar radiation. However, they will attain the ambient temperature by means of direct exchange of heat with the surroundings. Thus, the trusses are required to change in temperature by about 30ºC during the day.

Table 5.7: Optical parameters of the complete design

Mirror	Diameter (mm)	Radius of curvature (mm)	Distance to next optics (mm)	Description	Imp. parameters	Surface quality RMS at 632.8 nm (λ)
M1	500	4000.0	1506.66	Primary mirror	Conic value : -1.0 Bore dia : 120 mm Concave mirror	0.025
M2	152	1550.5	1816.6806	Secondary mirror	Conic value : -4.591864 Convex mirror	0.02
M3	53.8	920	460	Tertiary mirror for collimation	Conic value : -1.0 Concave mirror	0.02
M4	63.2	Infinity	700	Nasmyth mirror Beam steering at 23° angle	Plane mirror Diameter : 60 mm Central hole dia : 15 mm	0.02
M5	59	Infinity	1200	Beam steering at 9° angle	Plane mirror	0.02
M6	81	Infinity	300	Beam steering at 13° angle	Plane mirror	0.02
M7	87	Infinity	900	Beam steering at 45° angle	Plane mirror	0.02
M8	150	Infinity	600		plane mirror	0.02

For a length of 2 m aluminium truss system spanning about 0.5 m laterally, it turns out that the differential expansion of the truss rods because of inhomogeneities in CTE, or differences in truss length through a 30º range in temperature, would result in a tilt of about 5 arc-sec per percent of the inhomogeneity of material or dimensions. If we wish to limit this tilt to about 0.5 arc-sec, then the tolerance on the material properties or dimensions goes down to 1 part in thousand.

5.6 Design of Transfer Optics for Feeding the Beam to Back-End Instruments

In this section we present the complete design of the telescope, in which beam is sent to a stable platform, where our back-end instruments are planned to be placed. Schematic of the complete design is shown in Figure 5.5 and Optical parameters are given in Table 5.7. Residual wavefront error of the system is 0.0056λ. The system performance is same as shown in Figure 5.3 (a-c).

6. Mount Specifications

Modern telescopes use the alt-az mount because of its compactness. Modeling and testing of the telescope can be conveniently done at the factory before shipping. Since we plan to use the existing building and pillar on the island, the weight of the telescope, being small for the alt-az mount, will hardly cause any problem. The angular momentum vector, being primarily vertical, the transfer of vibrations from the telescope to the pier, will also be less than the equatorial or fork mounts. Basically, our design will then follow that of the mini-LEST (Anderson, Engvold and Owner-Pederson, 2002), except that we introduce the polarization package in the collimated beam after the 45° reflection into the elevation axis (conventionally called Nasmyth focus).

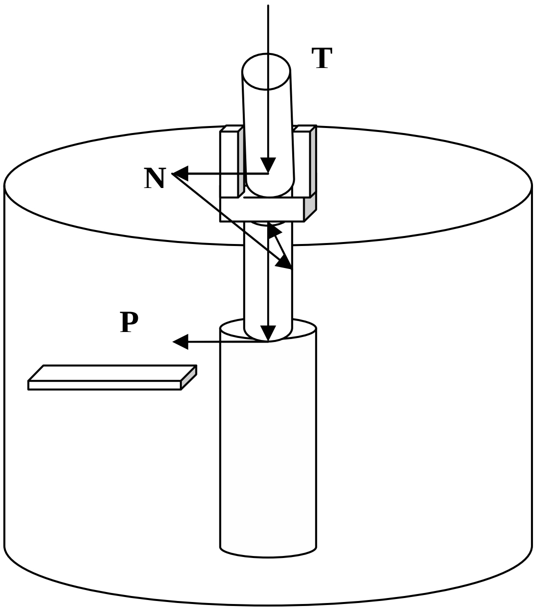

Figure 6.1: Schematic of the telescope layout. The light is taken out through the Nasmyth focus N of the alt-az telescope T and brought down to a suitable floor, where it is fed to the AO system followed by spectrograph, both placed on a platform P. A part of the beam is also tapped before the AO system, to feed an F-P based imaging filtergraph. The scheme of taking out the light through the Nasmyth focus is borrowed from the “mini – LEST” proposal.

The mechanical design of the mount must conform to the optical layout of Figure 5.5. Provision must be made to house the polarimeter within a hollow space inscribing the elevation bearing. Provision must also be made to access the reflected light from M5 to M6 (Figure 5.5). Both M6 and M7 must be housed in a hollow space inscribing the azimuth bearing and must rotate with the telescope’s azimuthal motion.

7. Tip-Tilt Secondary and Guider Telescope

A tip-tilt secondary is required to take care of differential shaking of M1 and M2 induced by vibrations created by wear and tear in the azimuth bearings, or by gusts of wind leaking into the telescope. Slower tilts are produced by uneven expansion of truss rods. A 25 micron depth of wear out in the azimuth bearings will result in a wobble of 10.0 arc-sec. If there are n bearings, the frequency of this wobble would be n/P, where P is the period of rotation of the yoke. If P = 24 hours, and n = 10000, then wobble frequency works out to 0.1 Hz. The error accumulated in 0.1 s is 0.1 arc-sec.

A guiding mechanism can compensate the tracking errors. A small guider telescope can be mounted and co-aligned with the main telescope. The technique of limb guiding is most appropriate since solar features are difficult to see in broad-band light, whereas the solar limb offers the highest contrast.

The focal length of the guider telescope and the pixel size of the CCD camera must be chosen to provide an image scale of 1 arc-sec per pixel. Assuring a centroiding accuracy of 1/10 pixel, we can achieve a guiding accuracy of 0.1 arc-sec. The CCD must accomodate 2 solar diameter in x and y directions. This decides the size of the CCD for limb observation. Since we have specified a large tracking accuracy for the telescope drive, we need to correct only every few seconds. The read out needs to be at the rate of 1 image every few seconds. The error signals generated by the guider should be fed to the telescope drive control system for correction.

The secondary unit must also have a focusing mechanism to counter the thermal expansion of the truss. The stroke of this mechanism must be more than 1 mm. The secondary will also tilt by about few arc-sec in few hours for each percent of non-uniformity in truss dimensions or material properties. A basic wave-front sensor like PUNTINO^{TM} of SPOT OPTICS, for example, can monitor this tilt, as well as non-alignment and defocus of the telescope optics, and correct these by using the tip-tilt secondary. The vendor must provide the entire sensing and correction package.

8. Weather Parameters

We have weather data from Udaipur GONG station at the main campus of USO since October 1995. The weather data recorded by GONG weather station consists of once a minute Atmospheric Temperature (^{o}C), Net Solar Radiation Flux falling on Earth (Watts/m^{2}), Relative Humidity (%), Atmospheric Pressure (millibars), Wind Speed (m/sec), and Wind Direction (degrees azimuth) measured clockwise from North. Having the simultaneous values of Wind Speed and Wind Direction, the components of Wind Speed along S-N and W-E directions can also be found out. Similarly, having the simultaneous values of Relative Humidity and Atmospheric Temperature, the Atmospheric Water Vapour Pressure (millibars) at the given temperature has been calculated. The values of these total 9 parameters between 02:00 - 11:00 UT, per day, over the year 1998 (600 × 365 values) have been shown in the form of 2-D plots using 16 level colour code in the figures below. We have chosen the year 1998 for our purpose, because of the availability of maximum number of data points for this year. It is observed that the components of Wind Speed along S-N and W-E directions are occasionally more than 10 m/sec, which indicate that there is a requirement of wind screen for the stable operation of the telescope.

We plan to install a weather station on the island to monitor all the weather parameters and use these parameters for decision making in respect to telescope operation.

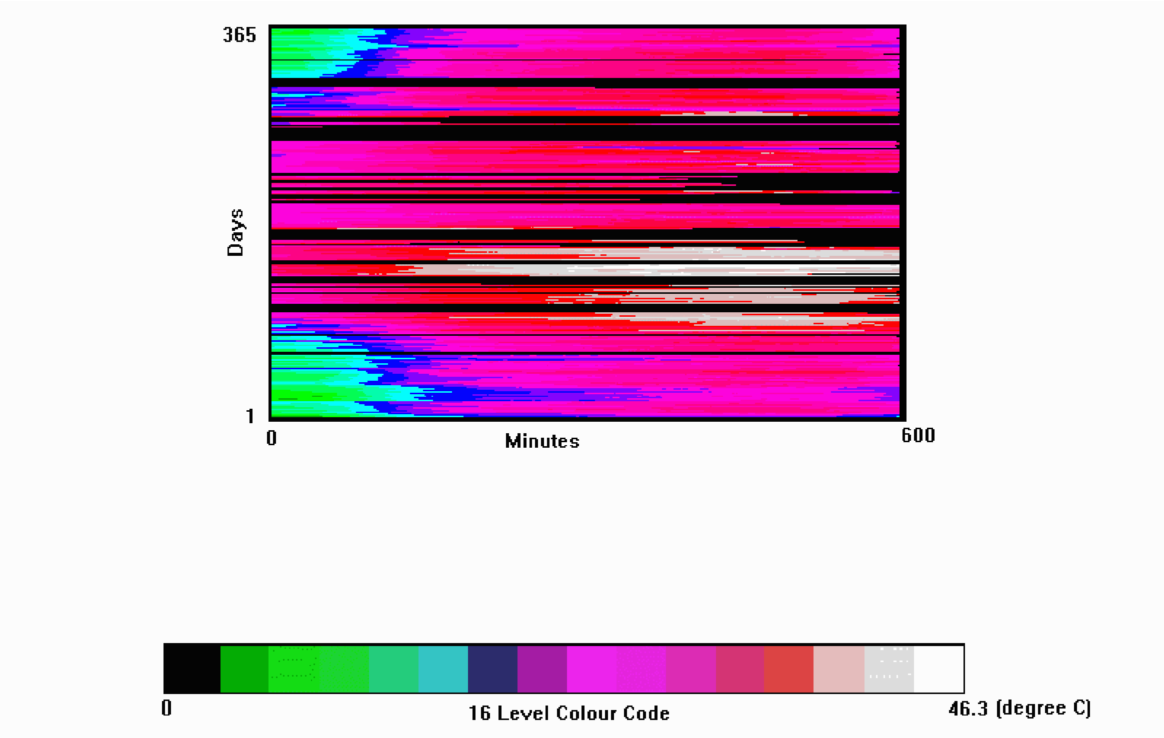

Figure 8.1: Atmospheric Temperature between 02:00 - 11:00 UT, per day, over the year 1998.

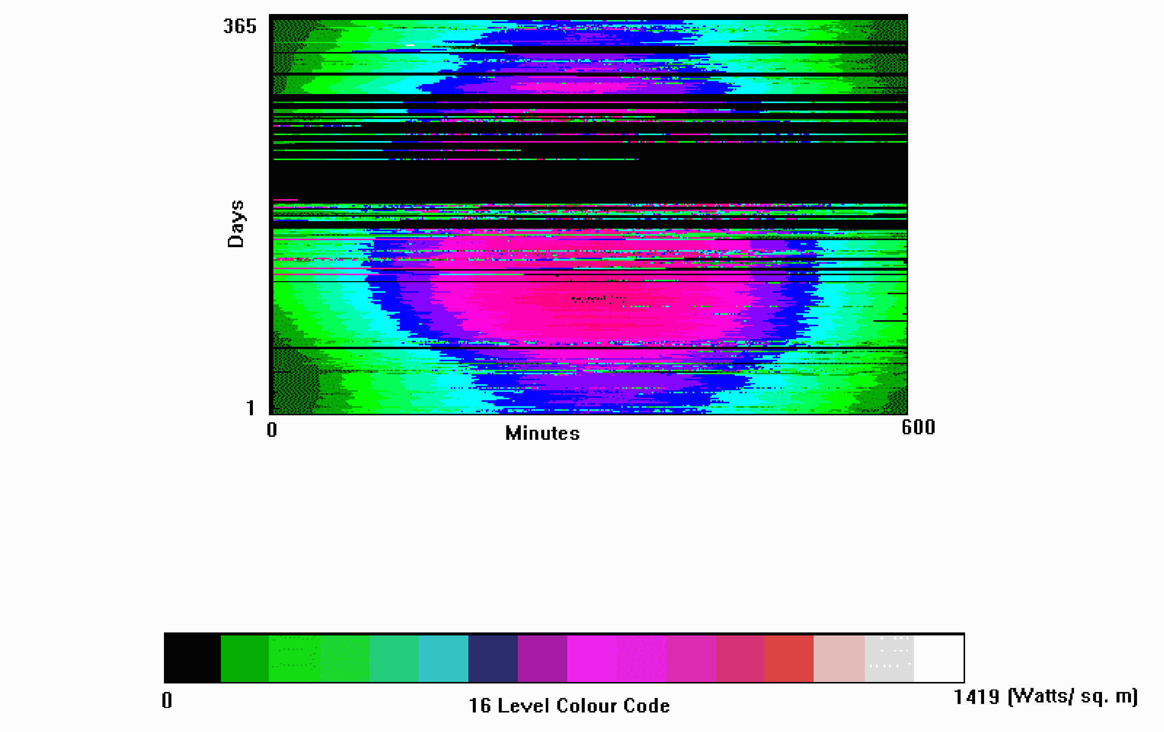

Figure 8.2: Net Solar Radiation Flux falling on Earth between 02:00 - 11:00 UT, per day, over the year 1998.

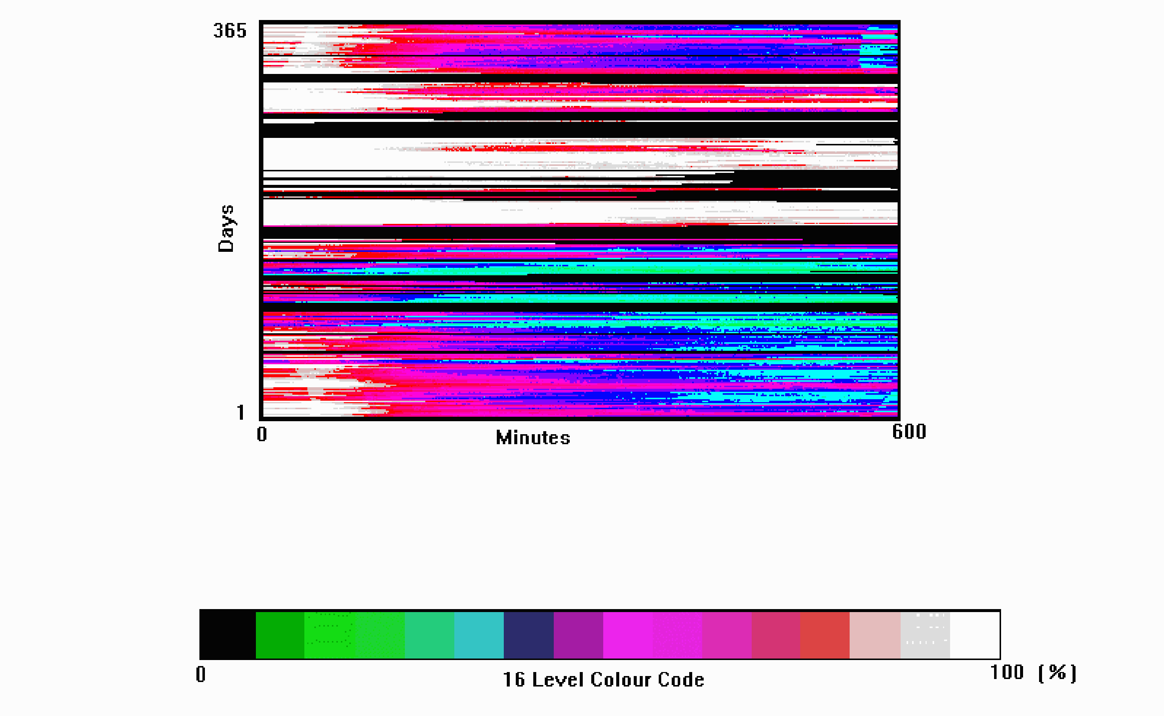

Figure 8.3: Relative Humidity between 02:00 - 11:00 UT, per day, over the year 1998.

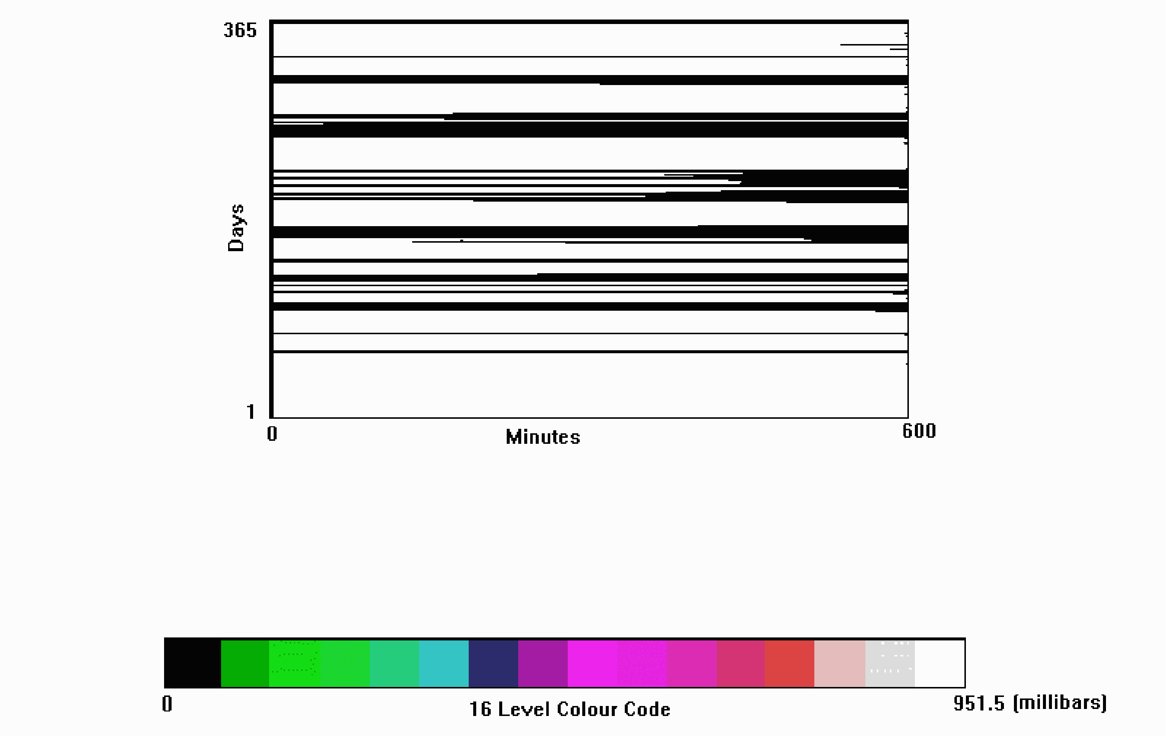

Figure 8.4: Atmospheric Pressure between 02:00 - 11:00 UT, per day, over the year 1998.

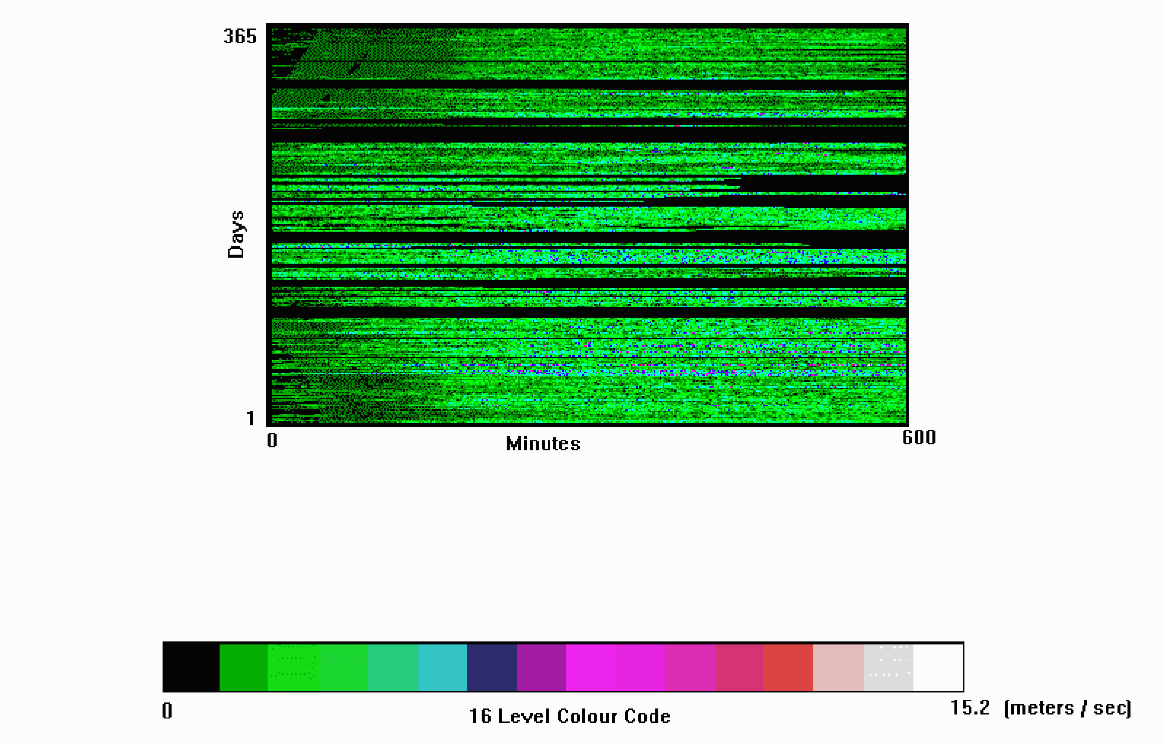

Figure 8.5: Wind speed between 02:00 - 11:00 UT, per day, over the year 1998.

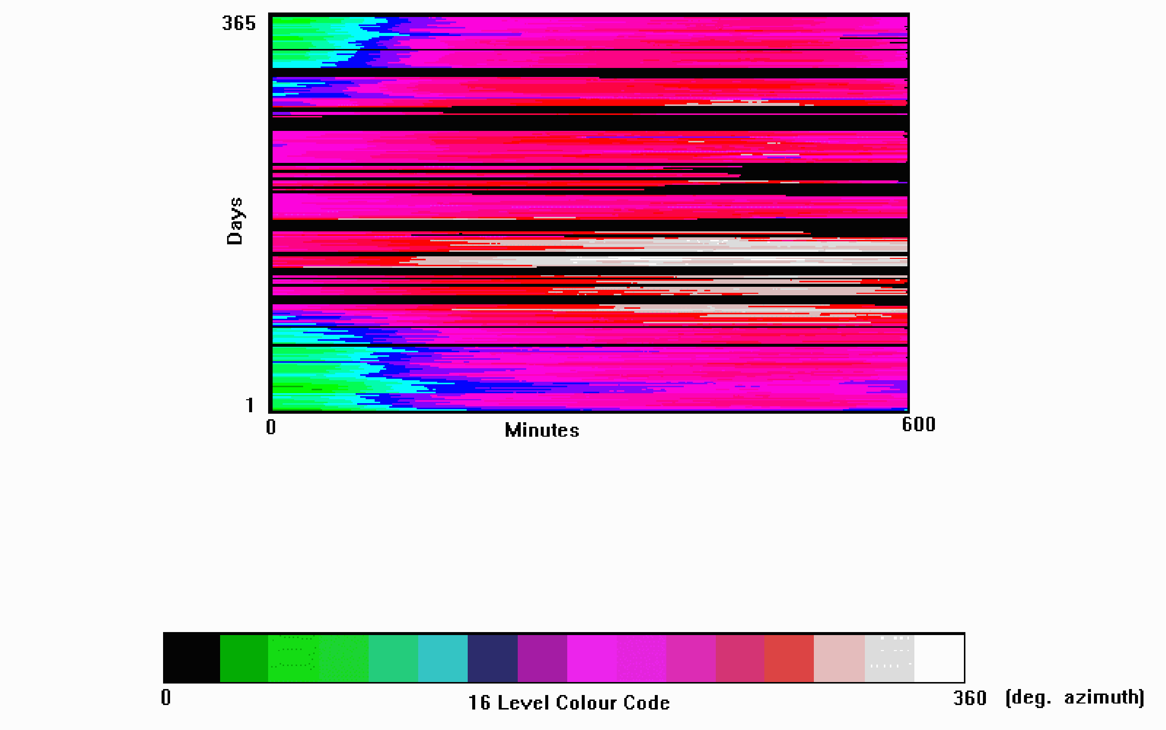

Figure 8.6: Wind direction between 02:00 - 11:00 UT, per day, over the year 1998.

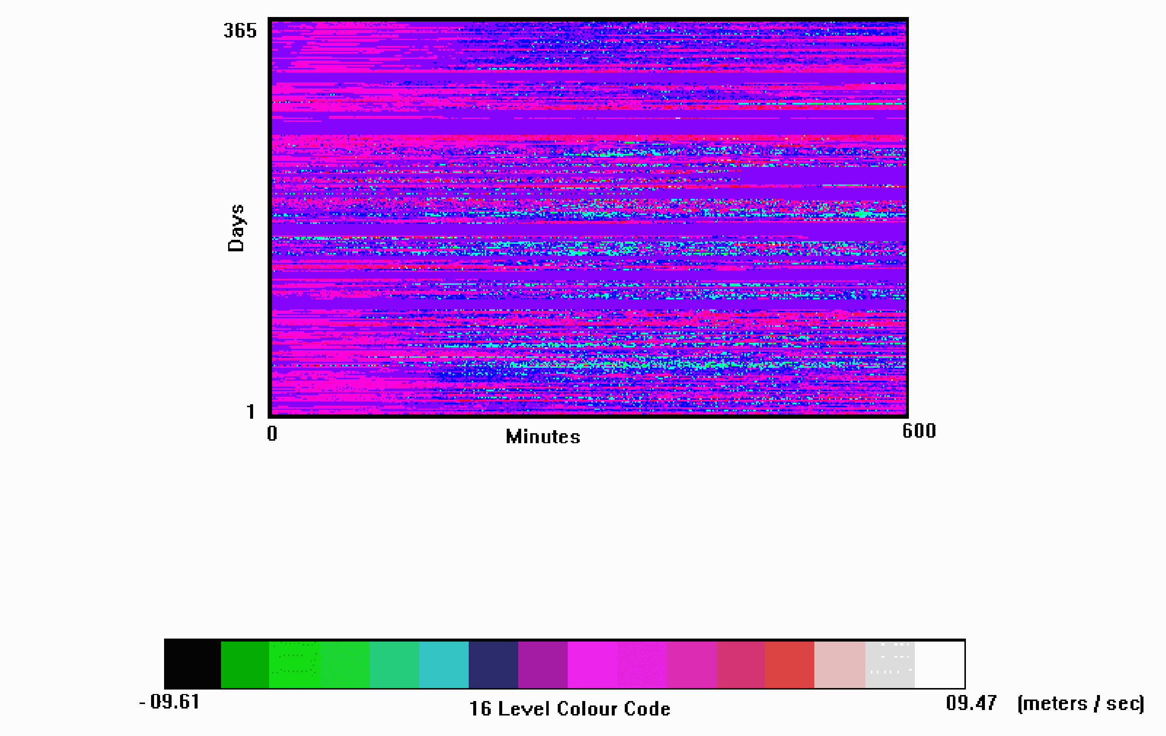

Figure 8.7: Wind speed along S-N direction between 02:00 - 11:00 UT, per day, over the year 1998.

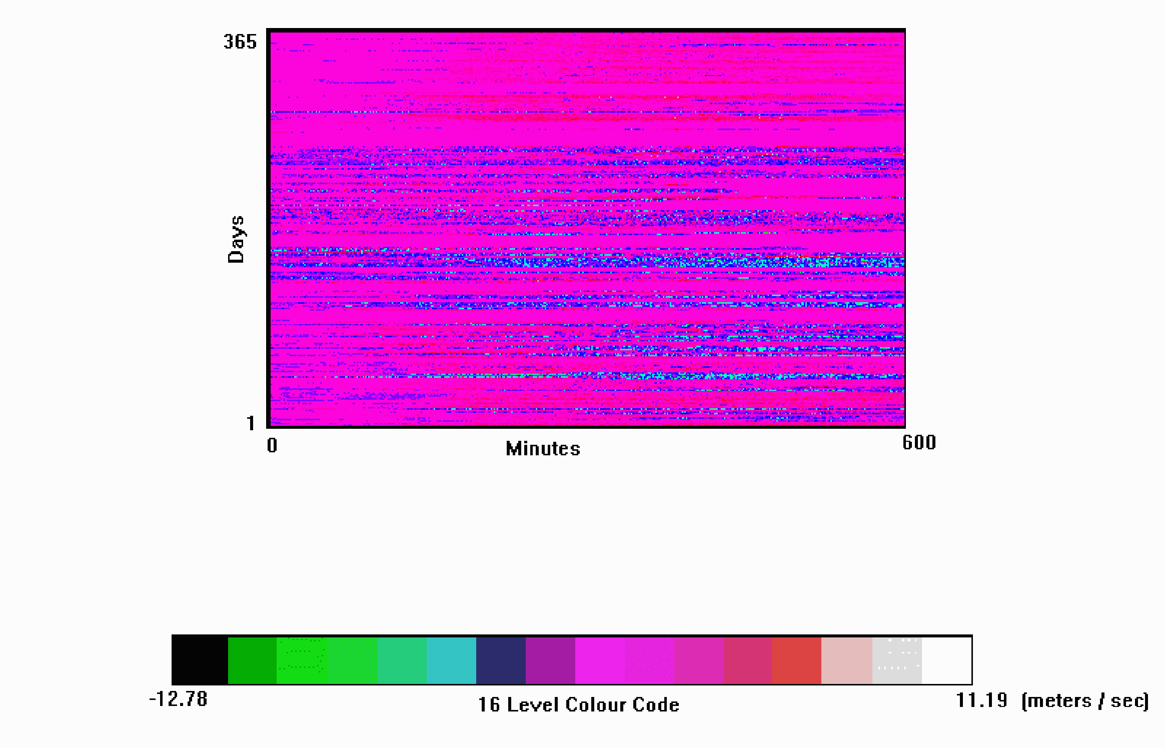

Figure 8.8: Wind speed along W-E direction between 02:00 - 11:00 UT, per day, over the year 1998.

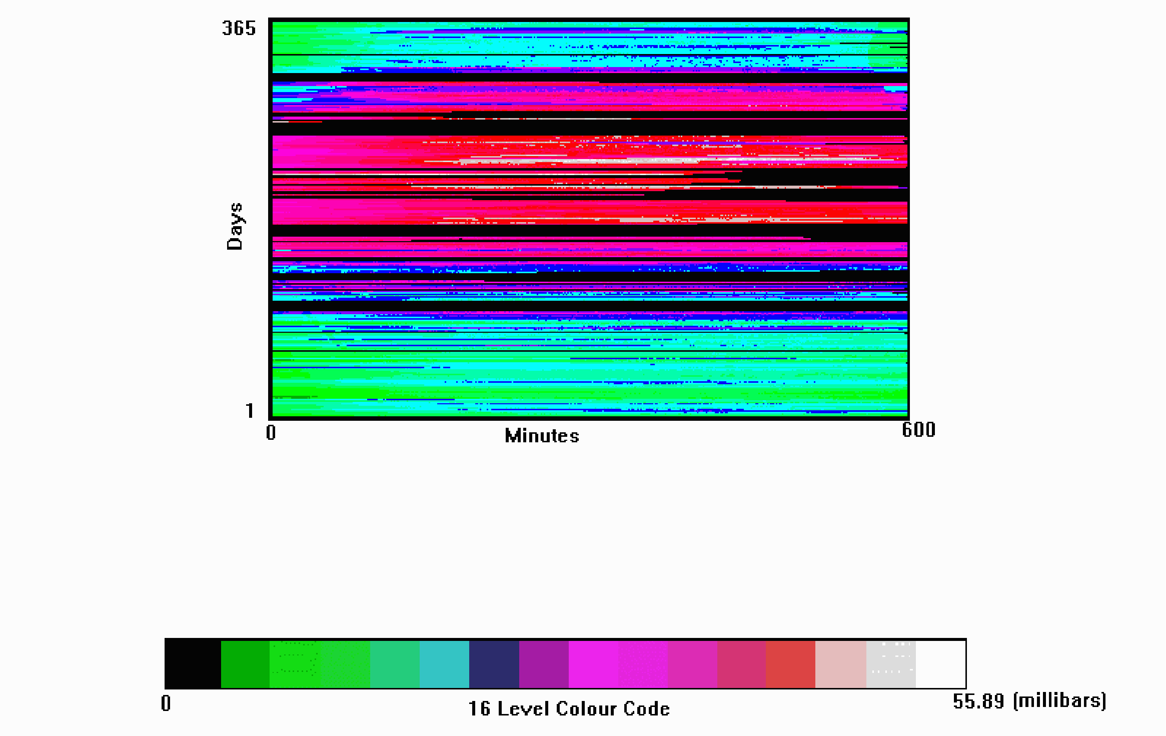

Figure 8.9: Atmospheric Water Vapour Pressure between 02:00 - 11:00 UT, per day, over the year 1998.

9. Dome and Building

A dome is necessary to house the telescope and protect it from the vagaries of the weather. The Dutch Open Telescope (DOT) uses the prevailing winds at that site to flush the heat. However, our site does not have such winds. Nevertheless, it is not completely devoid of winds either. For improving the thermal homogeneity in the telescope’s environment, we would like to avoid a dome during observations. Thus, we intend to remove the dome of the existing building and seat the MAST telescope on the existing pier. Since the existing pier already supports a spar telescope weighing more than 500 kg, there is no problem in replacing this with a more compact and light-weight telescope. We plan to extend the existing pier such that the elevation axis of the new telescope will be at the level of the ring supporting the existing dome.

To protect the telescope from winds during operation, we plan to install a collapsible wind-screen whose height can be varied to be always in level with the topmost extremity of the telescope. Since the telescope is of compact design (1.5 m in length), the maximum height of the wind shield needs to be 1.5 m. The manufacture of such wind-screens is feasible, according to the Chief Engineer, CED, ISRO HQ.

To protect the telescope from rain, when not in operation, we plan to erect a small enclosure for the telescope, which can be retracted away during observations. Ideally, the retracted enclosure must sink below the roof of the building to avoid thermal inhomogenieties in the vicinity of the telescope during operations. Again, because of the compact design of the telescope, this kind of enclosure is also feasible.

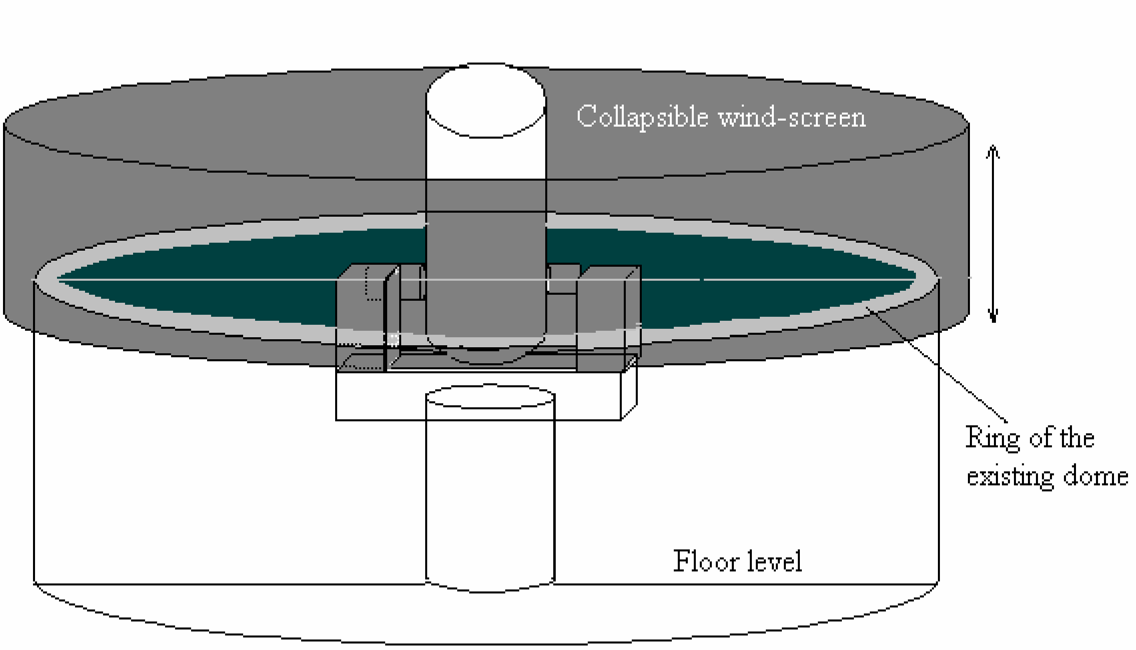

Figure 9.1: Top section of proposed modification of existing building. Existing dome will be replaced by a wall of variable height. The height of the wall will match the elevation of the telescope. In this way, the telescope will be protected from wind loading, at the same time thermal equalization will take place. A small retractable enclosure for the telescope will protect it from rains when not in use.

10. Control System

The telescope control would provide a mechanism for the telescope to point accurately in the sky, and then track the Sun over an extended period of time with the required accuracy. To achieve high accuracies, pointing and tracking systems are “closed-loop” system, in which deviations from desired functioning are detected and corrected. In classical closed loop servo system, there are angle position sensors on each axis of telescope, e.g., optical shaft angle encoders, and a microcomputer which compares the actual position (given by encoders) with the desired position (the apparent position of the object), and issues commands to bring these closer together. The main difficulty with this classical approach is that it senses errors at the telescope axes, not the object itself. No random or systematic error between the encoder and the image plane, such as tube or mount flexure, atmospheric refraction, are directly sensed. Instead, these errors are modeled in software. An alternative is to use a “sun sensor” which could be used to close the loop on the Sun, such that once the Sun is acquired, the Sun sensor, and not the optical encoders, assume control of the telescope. The telescope moves in the sky in “open loop” (i.e., without any position feedback), and when it arrives in the position of Sun, it acquires and centers it under microcomputer control. This is an example of the general class of servo control systems, in which the desired position and the current telescope position error signal is computed, which forms a command to the telescope drive motor. Since there are no encoder readings in open-loop system, the desired position of the telescope is adjusted to compensate for the telescope’s mechanical errors, which are as follows:

1. Zero offset (the zero point in hour angle or declination)
2. Polar axis misalignment (in equatorial mounts)
3. Non-perpendicularity of the axes
4. collimation errors
5. tube flexure
6. mount flexure
7. servo lag
8. gearing errors
9. bearing errors
10. drive train torsion errors

In each of the two axes, the telescope will be driven by a digitally-controlled stepper motors. The high resolution of 0.25° (corresponding to 0.1 arc-sec at the telescope axis) of the digital control on the motor shaft would allow the entire range of drive rates from maximum slew to finest increment guiding. For Sun tracking, the telescope will have a limb guider that centers the telescope on the desired part of the Sun. Blind pointing by means of encoders is unnecessary and usually inaccurate because the encoders are never perfectly aligned (Dunn 1985). However, a good tracking system improves the performance of the guider by requiring less frequent corrections.

10.1 Telescope Control System

The telescope control system (TCS) is the highest level of real-time controller. It would operate all major telescope sub-systems, including the mount, primary mirror support, tip-tilt mirror support, and image rotation control systems, among others. It would also provide basic services to the telescope, such as coordinated time, ephemeris calculation and prediction, coordinated motion, pointing and tracking adjustment.

10.2 Mount Control System

The mount control system (MCS) would provide the real-time controller for the major axes of the telescope, and occasionally for some of minor axes like Cassegrain/Nasmyth rotators. The MCS would also operate associated mechanical assemblies such as the cable wraps, brakes, and hydraulics.

10.3 Other Systems

Other telescope systems would include the enclosure/dome (ECS), wind shields, acquisition and guidance, adaptive optics (AO), and instrument (ICS) control systems. There is a definite cost advantage in duplicating as much of an existing control system as possible, for example the Mt. Abu telescope control system (Annexure III.)

10.4 Drive Specifications

All modern telescope manufacturers provide very accurate drive systems. A good example is that of the Himalayan Chandra Telescope (HCT), built by EOST for the Indian Institute of Astrophysics. After modeling and locking with an auto-guider system, the drive of the HCT maintains the target star within 0.3 arc-sec throughout the observation period. Such drives will decrease the load on the tip-tilt and AO systems, which can then concentrate on compensating for thermal expansions and atmospheric turbulence.

10.5 Control System Specifications

Table 10.1: Specifications of the control system

Drives	Sidereal and solar tracking Slew speed < 2 min to go from stow to any valid coordinate
Accuracy of acquiring the Sun	< 10 arc-sec
Accuracy of fine pointing	< 1 arc-sec
Stability/jitter	0.25 arc-sec for 10 minute open-loop; jitter no more than 0.05 arc-sec time less than 1 second
Zone of avoidance	5^0 around zenith
Safety limit switches	Hardware & software enabled
Electrical Supply	AC input supply 230 V, 50 Hz Indian standard.
Standby operation	Capability to operate under UPS

10.6 Schematic of the MAST Control System

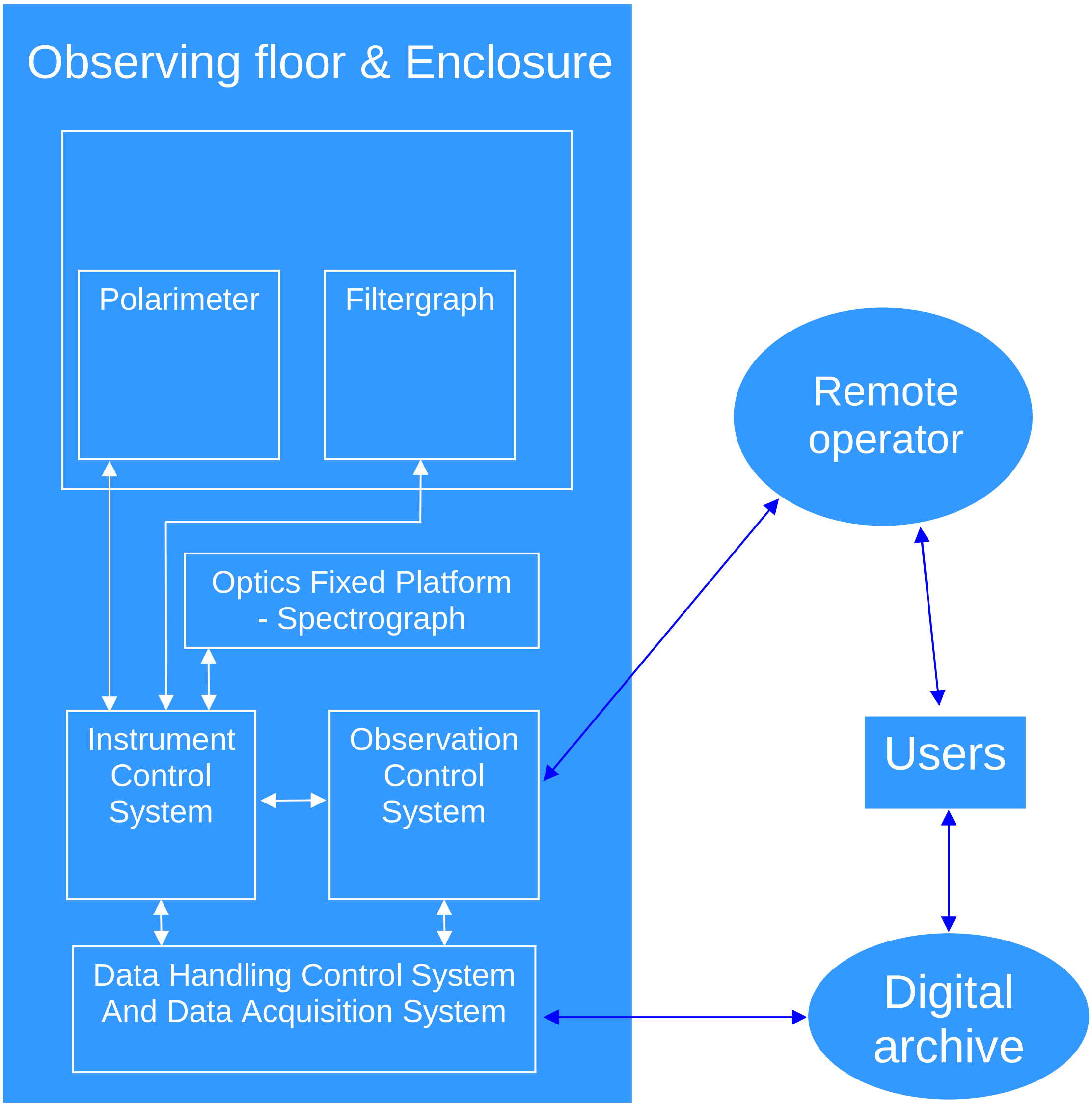

11. Back-end Instruments

We propose to deploy the back-end instruments on a stable platform that receives the collimated beam from M8 (Figure 5.5).

11.1 Polarimeter

11.1.1 On-line Compensation of Cross-talk:

The polarimeter will be placed on the elevation axis. The light, after collimation, encounters a 45° reflection. This reflection will produce I to Q, Q to I, V to U and U to V cross-talks, where I, Q, U, and V are the Stokes parameters of the sunlight entering the telescope. The I-Q talk can be represented as

$$I' = (1+X^2).I + (1- X^2).Q$$

$$Q'= (1- X^2).I + (1+ X^2).Q$$

Where X = ratio of reflectivities of p and s components.

By observing in the continuum near the observed line, we can safely assume that Q =0. Hence, we get

$$Q'= (1- X^2).I'/(1+ X^2)$$

A scatter plot of Q' vs. I' will easily provide X.

The talk of V into U is given by

$$U'= X\cos(\tau).U - X\sin(\tau).V$$

$$V'= X\sin(\tau).U + X\cos(\tau).V.$$

Where τ = retardance between p and s components.

This talk is more serious, and can be eliminated by introducing an extra retardance of $-\tau$ to the LC retarder during each step of the polarization modulation. We can obtain an initial estimate of τ, by observing a quiet region at disk center and doing a U vs. V scatter plot. In a quiet region at disk center, the magnetic flux tubes are vertical, hence U = 0. Thus,

$$U' = -\tan(\tau).V'$$

A scatter plot of V' vs. U' will provide τ. After this, we can get talk-free U by adding $-\tau$ to the retarder. The entire polarimeter must rotate about the elevation axis along with the telescope, to maintain the same reference axes with respect to the solar image. A quarter wave retarder must be attached with its fast axis at 45° to the analyzer axis, so that the output light is circularly polarised. A circularly polarized output will not change its intensity due to reflection at other mirrors further down the optical train.

11.1.2 Polarimetric Scheme:

The analyzer package measures the polarization of the line profiles induced by the magnetic field. This usually consists of one or more variable retarder plates and a linear polarizer. A polarization calibration set-up for the calibration of instrumental polarization will also be added for the proposed polarizing scheme.

Polarization analyzer package: In order to obtain the full vector magnetic field one should measure polarization state of the spectral line, i.e. all Stokes parameters I, Q, U and V. Stokes I gives the total intensity, V gives the circular polarization of the line, which is related to the line-of-sight magnetic field, while Q and U give the linear polarization which is related to the transverse field strength and azimuth. In principle, by using a combination of two variable retarders and a linear polarizer or a polarizing beam splitter, it would be possible to modulate the incoming polarization such that all Stokes parameters could be retrieved from the measurements. For the MAST telescope, liquid crystal variable retarders will be used as the polarization analyzers. This has the advantages of no moving parts and require only low voltages. In the following, the use of two liquid crystal variable retarders to produce the required polarization modulation is outlined.

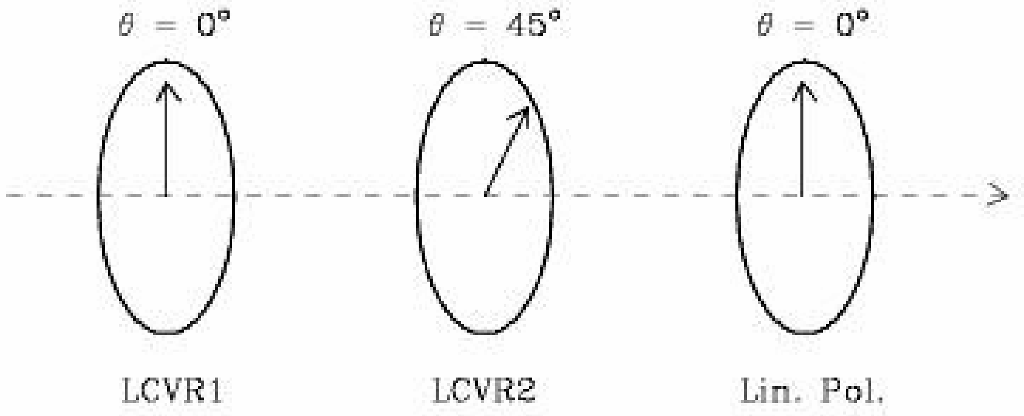

Figure 11.2: Polarization modulation scheme using two liquid crystal variable retarders (LCVR), the fast axis of which are placed at 0^0 and 45^0 to the transmission axis of the linear polarizer.

Modulation schemes using two LCVRs (Liquid Crystal Variable Retarders) have been extensively studied in the past (Collados, 2003). A very flexible configuration uses a first LCVR with its fast axis at 0^0 (i.e., aligned with the final linear polarizer) and retardance δ_1 and a second LCVR with the fast axis at 45^0 and retardance δ_2 as shown in Figure 11.2. Finally, the linear polarizer makes the polarization analysis (the linear polarizer could be replaced by a beam splitter to have dual beam set up). In this configuration, the detected intensity I_D is a linear combination of the Stokes parameters as given by

$$I_D = I + C_{\delta 2} Q + S_{\delta 1} S_{\delta 2} U - C_{\delta 1} S_{\delta 2} V \qquad (1)$$

$$C_{\delta 1} = \cos(\delta 1)\ ,\ S_{\delta 1} = \sin(\delta 1)$$

$$C_{\delta 2} = \cos(\delta 2)\ ,\ S_{\delta 2} = \sin(\delta 2)$$

For the vector mode, four independent linear combinations (I_1, I_2, I_3 and I_4) can be obtained where all four Stokes parameters are equally weighted.

By equating the coefficients that multiply the Stokes parameters, one finds that the retardance values needed are

$$\delta_1 = [45, 135, 225, 315], \quad \delta_2 = [54.736, 125.264, 234.736, 305.264]$$

Using these retardance values, the coefficients multiplying the Stokes parameters in equation (1) are all equal to $\pm (1/\sqrt{3})$. Considering the response time of the LCVRs, i.e. low voltages on LCVRs have high retardance and large jumps to increase the retardance (that is decreasing the voltage) corresponds to long switching times, one would also sets the retardance as

$$\delta_1 = [315, 315, 225, 225] \text{ and } \delta_2 = [305.264, 54.736, 125.264, 234.736]$$

and produce four accumulation states given by:

$$I_1 = I + (1/\sqrt{3})Q + (1/\sqrt{3})U + (1/\sqrt{3})V \tag{2}$$

$$I_2 = I + (1/\sqrt{3})Q - (1/\sqrt{3})U - (1/\sqrt{3})V$$

$$I_3 = I - (1/\sqrt{3})Q - (1/\sqrt{3})U + (1/\sqrt{3})V$$

$$I_4 = I - (1/\sqrt{3})Q + (1/\sqrt{3})U - (1/\sqrt{3})V$$

From the accumulated intensities (I_1, I_2, I_3 and I_4) , one recovers the Stokes parameters by simple inversion:

$$I = (1/4)I_1 + (1/4)I_2 + (1/4)I_3 + (1/4)I_4 \tag{3}$$

$$Q = (\sqrt{3}/4)I_1 + (\sqrt{3}/4)I_2 - (\sqrt{3}/4)I_3 - (\sqrt{3}/4)I_4$$

$$U = (\sqrt{3}/4)I_1 + (\sqrt{3}/4)I_2 - (\sqrt{3}/4)I_3 - (\sqrt{3}/4)I_4$$

$$V = (\sqrt{3}/4)I_1 - (\sqrt{3}/4)I_2 + (\sqrt{3}/4)I_3 - (\sqrt{3}/4)I_4$$

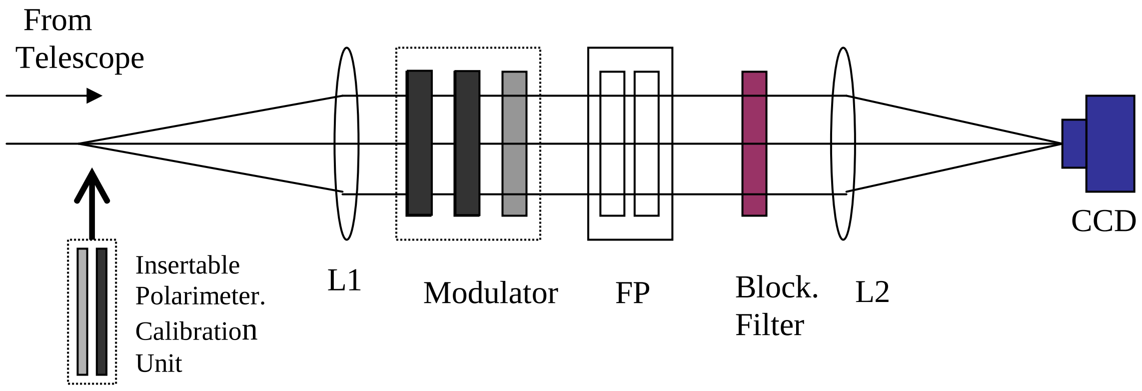

Figure 11.3: Optical layout of the proposed imaging vector magnetograph. L1 and L2 are the collimator and camera lenses, respectively. Modulator package consists of two liquid crystal variable retarders (dark block) and one linear polarizer (grey block). Polarization calibrator can be inserted into beam, the linear polarizer and fixed quarter wave plate are mounted on motors such that they can be oriented in any known angle with respect to the analyzer.

In this modulation scheme, the same images are used for deriving all the Stokes parameters. By introducing a linear polarizer and fixed quarter wave plate in front of the polarization package, it would be possible to calibrate the instrument for linear and circular polarizations. Setting the polarizer and retarder at appropriate angles and operating the modulation package in normal mode provides a calibration of the sensitivity of the instrument to various polarization states and the cross-talks.

11.2 Adaptive Optics System

We plan to design the adaptive optics for the proposed 50 cm telescope similar to the laboratory model and use the same lenslet array, Dalsa camera and tip/tilt and deformable mirrors, for wave-front sensing and correction. The control computer and software would be updated as per the availability of the new high-speed processor(s). The exact design parameters would be available only after the completion of the laboratory model by December 2004.

11.3 Fabry-Perot Based Narrow Band Filtergraph

The imaging vector magnetograph basically has two sections, a narrow band tunable filter and a polarization analyzer (modulator). The first of these components is used to isolate narrow spectral bands on the spectral line profile. The tunability of the filter is essentially used to position the pass band on a series of wavelength positions within the line profile. The tuning step and the spectral bandwidth of the narrow-band filter decides how well the line profile is reproduced.

The Narrow Band Filtergraph system will consist of a tunable air gap Fabry-Perot system with appropriate pre-filters for imaging spectroscopy. The FP consists of two parallel plates polished to $\lambda/200$ flatness and coated with multilayer dielectric coatings with reflectivity in excess of ~ 95 %. The FP plates are mounted on three piezo-electric stacks. The cavity spacing is adjusted by applying high voltages across piezos. The parallelism of FP plates is maintained by a bridge arrangement of gap sensing capacitance micrometers across two perpendicular axis and maintaining the balance by a CS100 closed-loop servo controller. The Free Spectral Range (FSR) near 6000 Å region is about 4 Å. Taking moderate estimate of reflectivity of plates to be ~90% (although specified value is ~ 95%) the reflective finesse is estimated to be ~30, which means FWHM of about ~130 mÅ. Adding flatness finesse for these highly polished ($\lambda/200$) plates to reflective finesse makes negligible change in net finesse value ~30. Thus a reasonable estimate of spectral resolution of FP is ~50000. The scan range of FP is 488 ± 3 μm. The scanning of FP can be accomplished by sending commands over RS232 interface. The parameters of FP are given in Table 11.1 below.

Table 11.1: Piezo-Electric etalon properties

Substrate Material	Fused Silica
Type	ET50 IC Optics inc.
Reflectivity	0.96 at λ=5500-7000 Å
Usable Aperture	50 mm
Plate Flatness	$\lambda/200$
Etalon spacing	488 ± 3 μm
Coating	Multi-layer dielectric coating

11.4 Spectrograph

In order to measure the velocity flows of the order of 0.5 km/s in the solar atmosphere using photospheric and chromospheric lines, we plan to have a spectrograph as a back-end instrument. The main requirement for the science goals to be met is the large wavelength range so that more than two spectral lines can be chosen for spectroscopy in the photosphere as well as the chromosphere. In order to be able to measure the small velocities of the order of 0.5 km/s, one requires a high linear dispersion of 5.25 mÅ /pixel. If one uses a CCD of 24 microns size pixels, then the required dispersion is 21.8 pm/mm. For designing such a high dispersion spectrograph, the chief components i.e. the entrance slit, collimator, grating and camera have to be suitably selected. There are different configurations for the arrangement of these components. The simplest of these is the Littrow arrangement that uses the same optics as a camera and collimator.

Design considerations: One can choose a specific pixel size. For a specific wavelength and the littrow condition, the telescope focal ratio is determined. The spectrograph focal length depends upon the pixel size and grating selection. The availability of particular diffraction gratings of specific blazing angles also guide the designing of the spectrograph for the MAST. Our goal of wavelength diversity, i.e., observing at more than two wavelengths requires a longer focal length of the spectrograph which is not difficult as the spectrograph will be installed on a stationary platform. The choice of pixel size matching the littrow condition for the spectrograph will minimize the overall spectrograph size and is a significant factor to be considered in the design.

Further, the design of the spectrograph takes into consideration the coupling of the spectrograph to the main telescope. From all these factors, we consider a basic design with 24 μm slit-width, f/40 telescope feed which approximately matches with the basic f-ratio of the telescope and therefore, no major scaling would be required prior to the entrance at the slit. The spectrograph size can then be either 1.8 m or 2.2 m depending upon the choice of the gratings with blazing angle 63.46^0 or 57^0 (Table 11.2). Therefore, the larger size of the spectrograph can take into account the multi-camera optics for observations in several wavelengths.

11.5 Spectrograph Specifications:

Table 11.2: Specification of the proposed spectograph

Spectral Lines	Wavelength (Å) 6302 (Fe I), 5173 (Mg II b), 8542 (Ca II), 4861 (Hβ)
Linear dispersion	22 pm/mm (6302.5 Å)
Slit-width	24 μm
Littrow Collimator	2 m focal length
Grating	Echelle grating 79 lines/mm, blazed at 63.46^o, 36 order for 6301.5 Å
CCD camera	24 μm pixel size

References :

Ambastha, A., and Bhatnagar, A.: 1988, *J. Astrophys. Astron*. **9**,137.

Ambastha, A., Hagyard, M. J., and West, E. A.: 1993, *Solar Phys*. **148**, 277.

Ambastha, A., Basu, S., Antia, H. M.: 2003, *Solar Phys.* **218**, 151.

Ambastha, A., Basu, S., Antia, H. M., and Bogart, R. S.: 2004, *SOHO14/GONG*.

Anderson, T., Engvold, O., and Owner-Pedersen, M.: 2002, LEST Foundation Technical Report No. 64, Institute of Theoretical Astrophysics, Oslo.

Beckers, J. M.: 1981, in Jordan (ed.), *Sun as a Star,* p.61.

Bhatnagar, A.: 1968, Ph.D. thesis, Agra University.

Bhatnagar, A., Jain, K., and Tripathy, S. C.: 1999, *Astrophys. J.* **521**, 885.

Bhatnagar, A., Jain, K., and Tripathy, S. C.: 2002, *Astrophysics and Space. Sci.* **281**, 761.

Bhattacharyya, J. C.: 1970, D.Phil. thesis, Calcutta University.

Born, M., and Wolf, E.:1980, *Principles of Optics*, Pergamon, Oxford.

Collados, M. V.: 2003, in S. Fineschi (ed.), *Polarimetry in Astronomy*, Proceedings of the SPIE, 4843, 55.

Dashora, N.: 2003, *Project report*, USO.

Debi Prasad, C., Ambastha, A., and Ai, G.: 1998, *Solar Phys.* **179**, 133.

Debi Prasad, C.: 2000, in *Proc. IAU Colloq. 179*, Venkatakrishnan, P., Engvold, O., and Choudhuri, A.R. (eds.), J. Astrophys. Astron. 21, 249.

Dunn, R. C.: 1985, *Solar Phys.* **100**, 1.

Evershed, J.: 1909, *Mon. Not. R. Astron. Soc.* **69**, 454.

Falconer, D. A., Moore, R. L., and Gary, G. A.: 2002, *Astrophys. J.* **569**, 1016.

Faurobert-Scholl, M.: 1993, *Astron. Astrophys.* **268**, 765.

Feynman, J., and Ruzmaikin, A.: 2004, *Solar Phys.* **219**, 301.

Fontenla, J., Ambastha, A., Kalman, B., and Csepura, G.: 1995, *Astrophys. J.* **440**, 894.

Fried, D.L.: 1966, *JOSA* **56,** 1372.

Hagyard, M. J., Stark, B., and Venkatakrishnan, P.: 1999, *Solar Phys.* **184**,133.
Hudson, and Cliver : 2001, *J. Geophys. Res.* **25**, 199.

Jain, K., Tripathy, S. C., and Bhatnagar, A.: 2000, *Astrophys. J.* **542**, 521.

Keller, C. U.: 2000, In *Proc. IAU Colloq. 179*, Venkatakrishnan, P., Engvold, O., and Choudhuri, A. R. (eds.), J. Astrophys. Astron. 21, 127.

Krishnakumar, V., and Venkatakrishnan, P. 1999, *Solar Phys.* **186**, 43.

Krishnakumar, V.: 2000, Ph.D. thesis, Bangalore University.

Leka, K. D., van Driel-Gesztelyi, L., and Canfield, R.C.: 1994, in Balasubramaniam, K. S., and Simon, G. W. (eds.), *ASP Conf. Series Vol. 68*, NSO/Sac Peak Solar Physics Workshop, p.145.

MacQueen, R. M.,and Fisher, R. R.: 1983, *Solar Phys.* **89**, 89.

McGlamery, B. L.: 1976, *SPIE* **74**, 225.

Nagendra, K. N., and Stenflo, J. O.: 1999, *Solar Polarization*, Astrophysics and Space Science Library, Vol 243, Kluwer Academic Press.

Noll, R. J.: 1976, *JOSA* **66**, 207.

Parker, E.N.: 1979, *Cosmical Magnetic Fields*, Oxford University Press.

Rangarajan, K. E.: 1999 in K. N. Nagendra, and J. O. Stenflo (eds.), *Solar Polarization*, Proceedings of an international workshop held in Bangalore, India, 12-16 October, 1998, Kluwer Academic Publishers, Boston, Mass., p.179-188.

Rangarajan, K.E., and Rao, D. M.: 1999, *Astrophys. J.* 524, L139.

Ravindra, B., Venkatakrishnan, P., and Kumar, B.: 2004, *Solar Phys.*(In press).

Rimmele, T. R.: 2004, *Astrophys. J.* **604**, 906.

Scharmer, G. B., Dettori, P., Lofdahl, M. G., and Shand, M.: 2003, *SPIE* **4853,** 52.

Schrijver, et al.: 1998, *Nature* **394**, 152.

Shannon, R. R.: 1997, *The Art and Science of Optical Design*, Cambridge University.

Sivaraman, K.R.: 1970, Ph.D. thesis, Madurai University.

Sivaraman, K.R., Rausaria, R.R., and Aleem, S.M.: 1992, *Solar Phys.* **138**, 353.

Sridharan, R., Venkatakrishnan, P., and Verma, V. K.: 2002, *Solar Phys.* **211**, 395.

Sridharan, R.: 2003, Techniques for achieving higher spatial resolution', Ph.D. thesis, Bangalore University, Bangalore.

Srivastava, N.: 1994, Ph.D. thesis, Pt. Ravishankar Shukla University, Raipur (M. P.)

Srivastava, N., Schwenn, R., Inhester, B., Martin, S., and Hanoaka, Y.: 2000, *Astrophys. J.* **534**, 468.

Srivastava, N., and Venkatakrishnan, P.: 2004, *J. Geophys. Res.* (In press)

Stenflo, J. O. : 1994, *Solar Magnetic Fields: Polarized Radiation Diagnostics*, Kluwer,Dordrecht.

Stenflo, J. O., and Nagendra, K. N.: 1996, *Solar Phys.* **164**, Proc. 1st SPW.

Stenflo, J. O., and Keller, C. U.: 1997, *Astron. Astrophys.* **321**, 927.

Thompson et al.: 1999, *Astrophys. J.* **517**, L151.

Tripathy, S. C., Jain, K., and Bhatnagar, A.: 2003, in S.C. Tripathy and P. Ventakatakrishnan (eds.), *Probing the sun with high resolution*, Narosa Publishing House, New Delhi, p.199-202.

Udit Narain and Ulmschneider, P.: 1990, *Space Sci. Rev.* **54**, 377.

van Ballegooijen, A. A., Nisenson, P., Noyes, R. W., Lofdahl, M. G., Stein, R.F., Nordlund, A., and Krishnakumar, V. : 1998, *Astrophys. J.* **509**, 435.

van Driel-Gesztelyi et al.: 1999, *ASP Conf. Series* **184**, 302.

Venkatakrishnan, P.: 1979, *Solar Phys.* **63**, 135.

Venkatakrishnan, P.: 2000, in *Proc. IAU Colloq. 179*, P.Venkatakrishnan, O. Engvold, and A.R. Choudhuri (eds.), J. Astrophys. Astron., 21, 171

Venkatakrishnan, P., Kumar, B., and Tripathy, S. C.: 2002, *Solar Phys.* **211**,77.

Venkatakrishnan, P., Kumar, B., and Tripathy, S. C.: 2003, in S.C. Tripathy and P. Ventakatakrishnan (eds.), *Probing the sun with high resolution*, Narosa Publishing House, New Delhi, p.203-207.

Venkatakrishnan, P., and Ravindra, B.: 2003, *Geophys. Res. Lett.* **30**, 2181.

von der Lühe, O.: 1984, *J. Opt. Soc. Am.* **A1**, 510.

Wilson, R. N.: 2001, *Reflecting telescope Optics-II* , Springer.

Zarro et al.: 1999, *Astrophys. J.* **142**, L520.

ANNEXURE I [†]

1. Diurnal variation of r_0 (Fried's Parameters)

Figures 1, 2, 3 and 4 show the diurnal variation in r_0 during March 20 - 23, March 24 -28, March 29 -31 and April 01 -04, 2003 respectively. In each plot the 'asterisk' shows the r_0 value corresponding to the time whereas the bar with 'asterisk' shows error in the results. It is found that the error is ~ 25% in each value of r_0.

2. Variation of r_0 at a particular time each day

We are interested in finding the variation in r_0 for a fixed time each day. In this way we will be able to know how everyday morning, afternoon or evening the level of turbulence is varying and thus we can infer when the relative seeing conditions during the day.

Figure 5 shows the distribution of r_0 measured around 10:15 hrs from March 20 to April 05, 2003. It indicates that r_0 value is between 1.5 cm to 2.0 cm for four days, between 2.0 cm to 2.5 cm for eight days and between 2.5 cm to 3.0 cm for five days. That is, at 10:15 hrs, r_0 attains the maximum value only for five days, whereas it has medium range for eight days and the minimum for four days. Therefore we infer that if we consider r_0 = 2.5 - 3.0 cm corresponds to the better seeing conditions (in comparison to other days), the seeing was better only for five days at 10:15 hrs.

Figure 6 shows the distribution of r_0 measured around 12:00 hrs from March 20 to April 05, 2003. It indicates that r_0 falls in the range of 1.0 to 3.0 cm. The maximum value is only for one day and is in the range 2.5 - 3.0 cm. It falls in the range of 1-5 to 2.0 cm for nine days and 2.0 to 2.5 for six days. Here, we also note that the minimum value (1.0 - 1.5 cm.) occurs only once. Hence we can say that at 12:00 hrs., the seeing becomes rather poorer than what it was at 10:15 hrs, in the sense that the maximum value (r_0 = 2.5 - 3.0 cm) here occurs only for one day and r_0 is less than 2.0 cm for ten days.

Figure 7 shows the distribution of r_0 measured around 14:30 hrs from March 20 to April 05, 2003. Here too, the maximum value of r_0 (2.5 - 3.0 cm.) occurs only for one day. It lies between 2.0 to 2.5 cm for eight days and 1.5 to 2.0 cm for seven days. Therefore, these results indicate that the seeing at 14:30 hrs is a little better than that at 12:00 hrs.

Figure 8 shows the distribution of r_0 measured around 15:45 hrs from March 20 to April 05, 2003. The maximum value that r_0 attains at this time is in the range of 2.0 cm to 2.5 cm, that too only for five days and for rest of the days the r_0 lies between 1.5 cm to 2.0 cm. Here, r_0 does not go beyond 2.5 cm even for a single day. Also only five days have the maximum value. The seeing is not good in comparison to that at 14:30 hrs and poorer in comparison to that at 10:15 hrs.

[†] *This annexure is an excerpt from the project report submitted by Mr. Nirvikar Dashora. The main aim of the project was to estimate the Fried's parameter (seeing conditions) in the absence of water in lake Fateh Sagar. The main results of the project are described here.*

3. Histogram of all the measurements

Figure 9 shows the histogram of all the measurements. We have 63 observations. These 63 r_0 values are plotted against the number of observations i.e. how many number of observation have a particular r_0 value. We find that

r_0 = 1.0 cm to 1.5 cm for 01 observation
r_0 = 1.5 cm to 2.0 cm for 28 observations
r_0 = 2.0 cm to 2.5 cm for 27 observations
r_0 = 2.5 cm to 3.0 cm for 07 observations

-At first sight these values reveal that almost equal number of observations have the r_0 = 1.5 - 2.0 cm and r_0 = 2.0 - 2.5 cm. This directly gives us the range of $r_{0,}$ which can be taken as 1.5 cm to 2.5 cm. Also a major part of total number of observations i.e. 55 out of 63 falls in this range, it can be taken as the range of variation of Fried's parameter (r_0) for the total number of days of observations.

- Only 7 out of 63 observations having maximum value of r_0. This means, that seeing was best for these many number of observations over the period of 16 days.

- 1 out of 63 observations has the r_0 value less than 1.5 cm which can be taken as an exceptional case.

Figure 10 shows a plot of r_0 vs. the time of observation for the entire data.

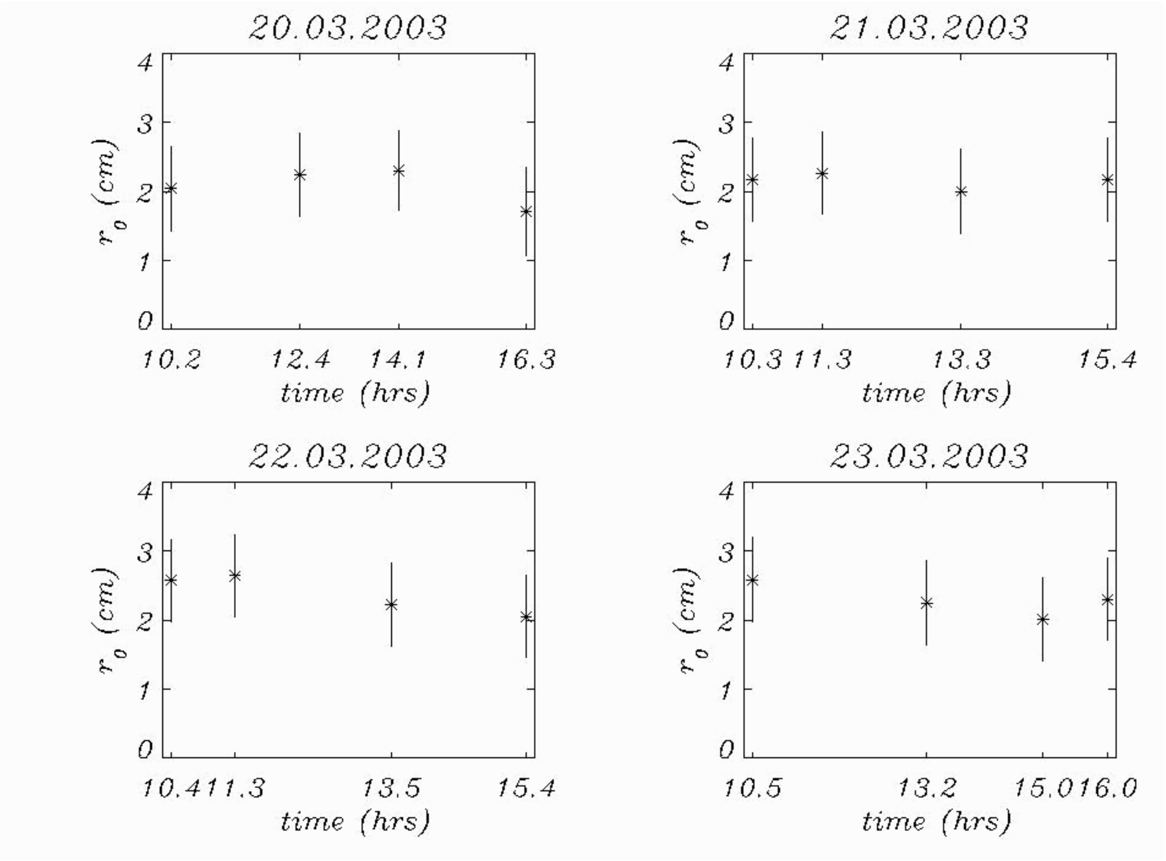

Figure 2: This figure shows the diurnal variation of r_0 from March 20 to 23, 2003.

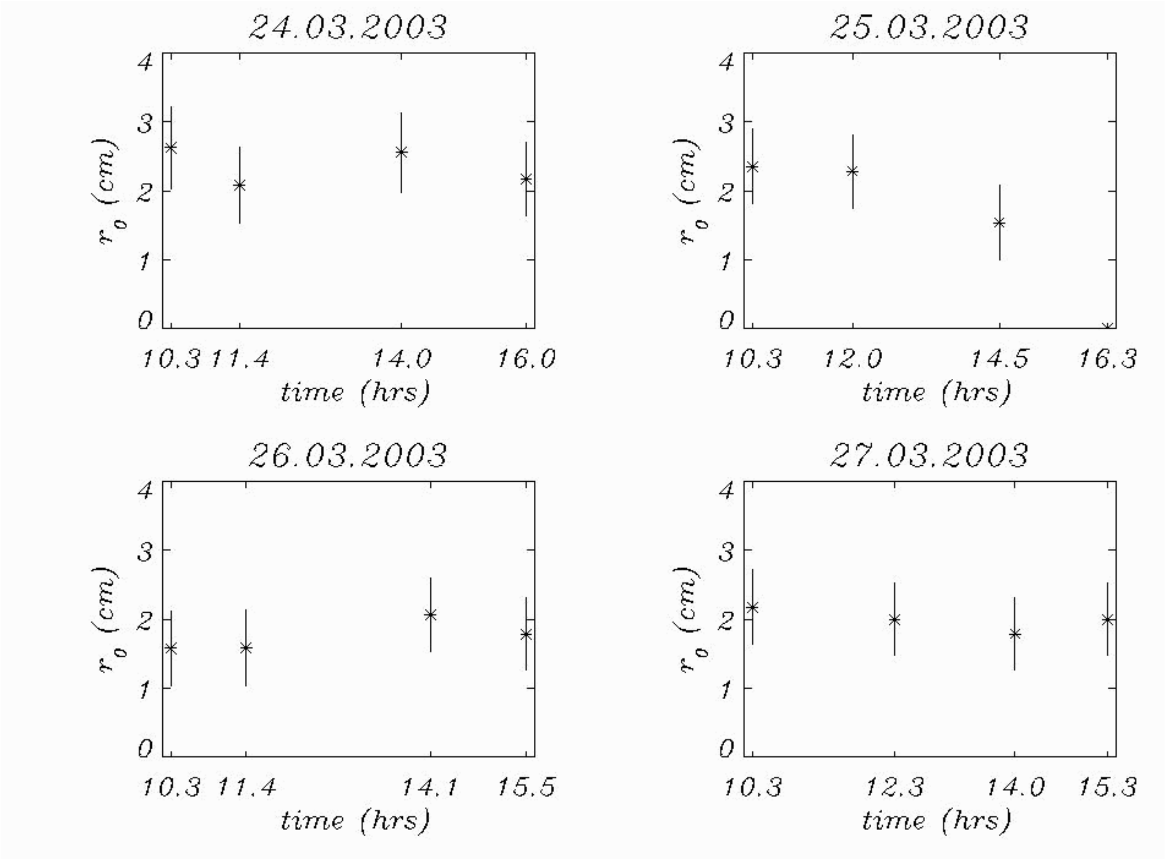

Figure 2: This figure shows the diurnal variation of r_0 from March 24 to 27, 2003.

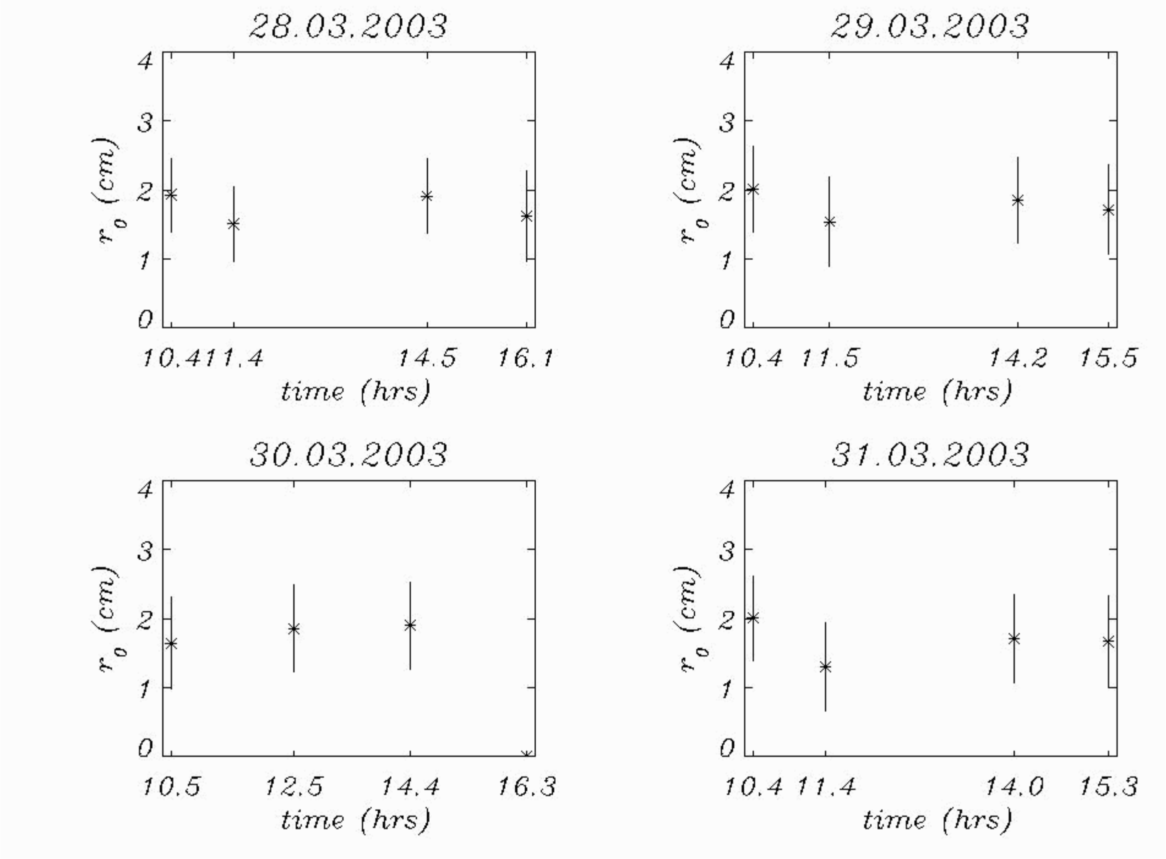

Figure 3: This figure shows the diurnal variation of r_0 from March 27 to 31, 2003.

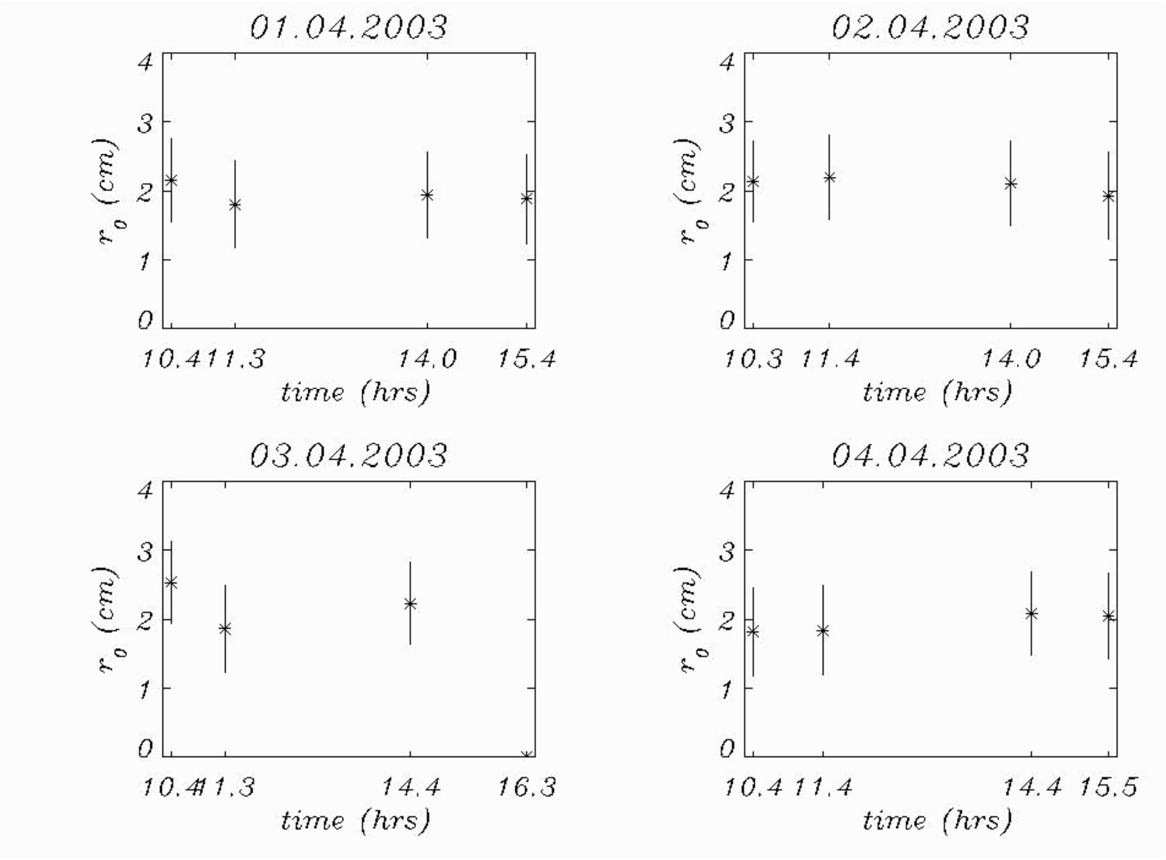

Figure 4: This figure shows the diurnal variation of r_0 from April 01 to 04, 2003

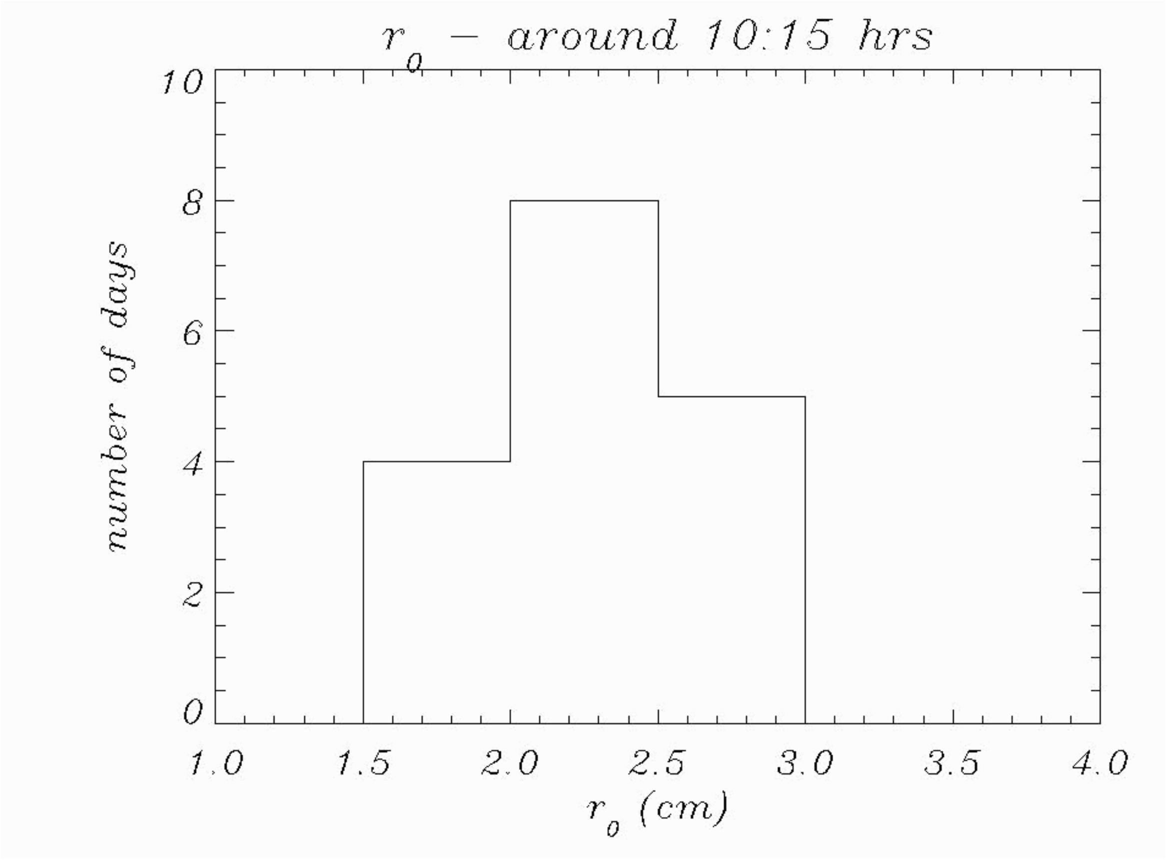

Figure 5: This figure shows the histogram of r_0 around 10:15 hrs from March 20 to April 5, 2003.

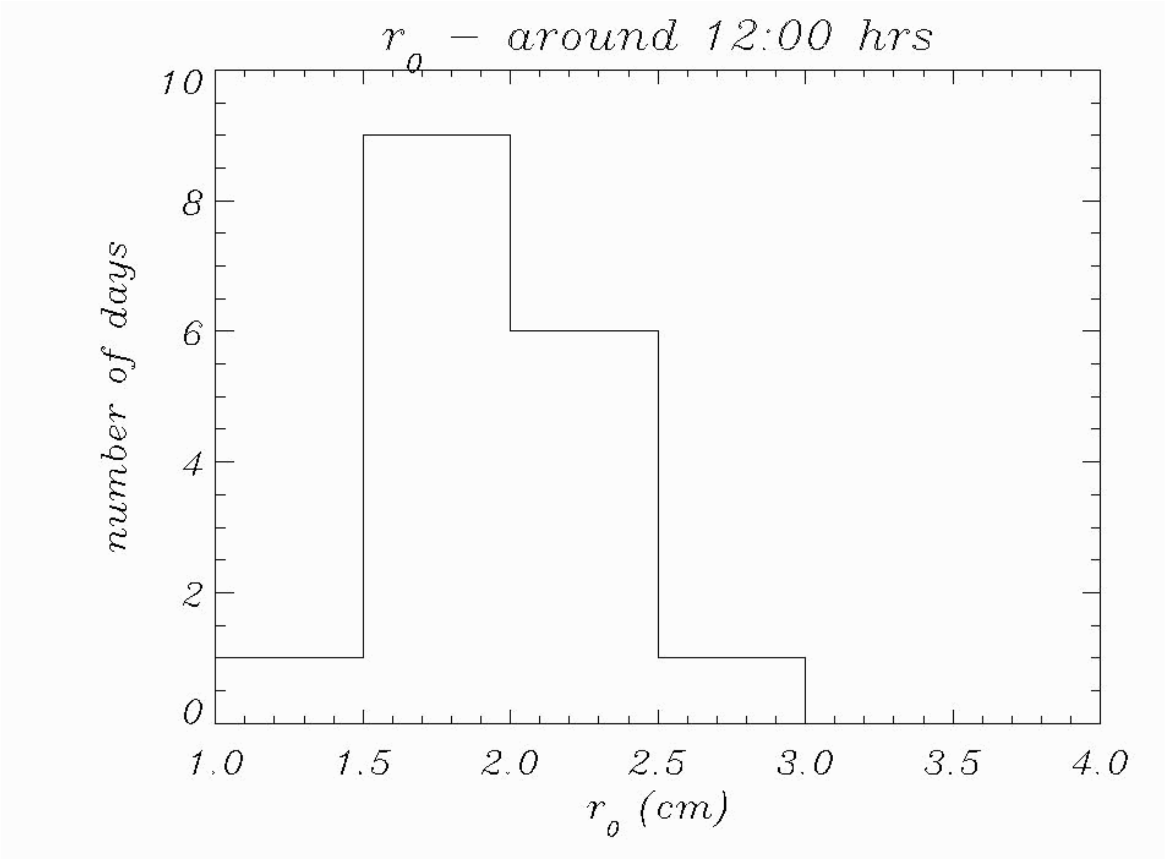

Figure 6: This figure shows the histogram of r_0 around 12:00 hrs from March 20 to April 5, 2003.

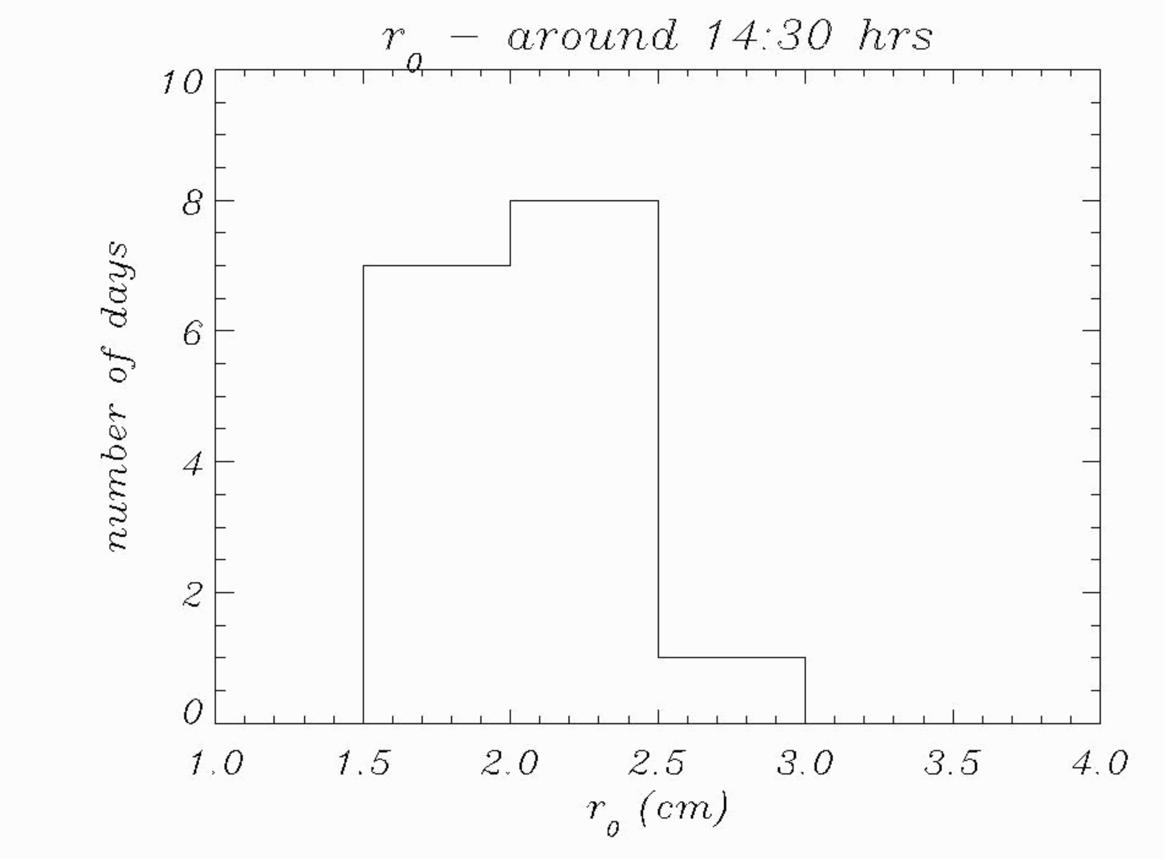

Figure 7: This figure shows the histogram of r_0 around 14:30 hrs from March 20 to April 5, 2003.

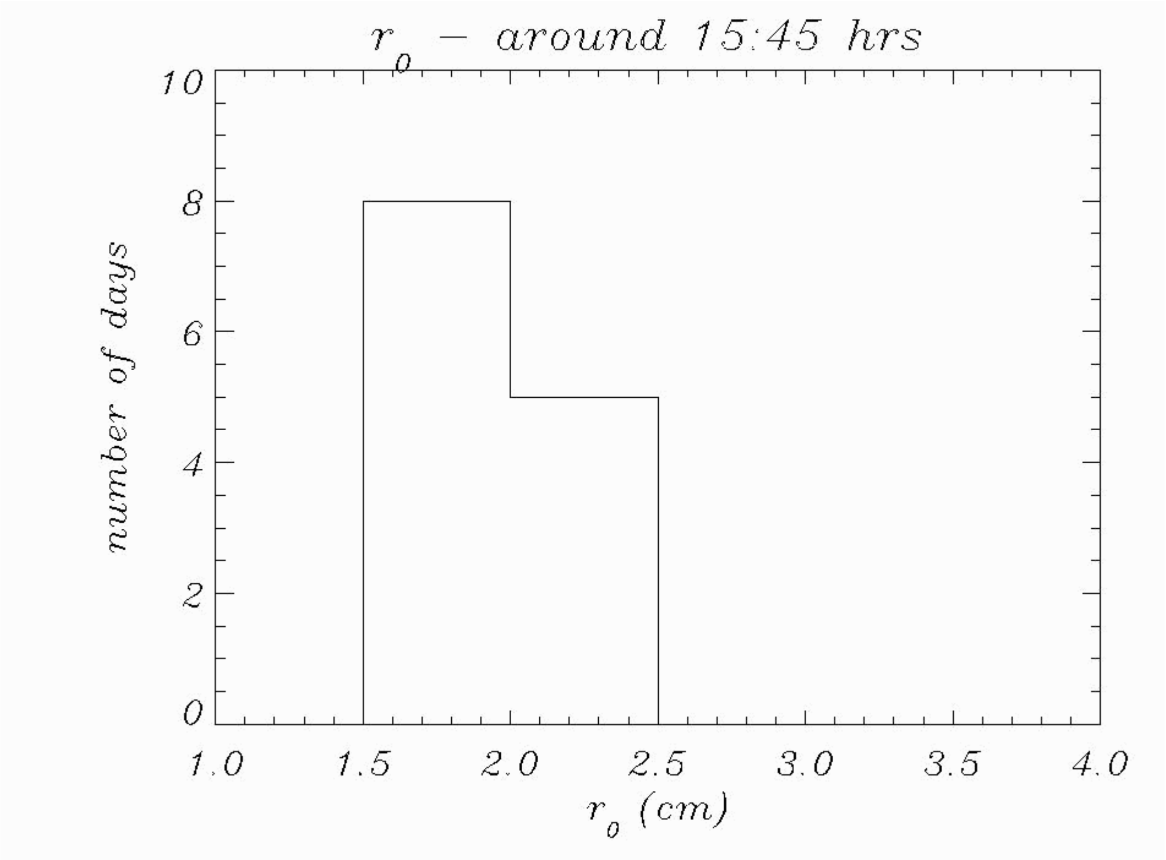

Figure 8: This figure shows the histogram of r_0 around 15:45 hrs from March 20 to April 5, 2003.

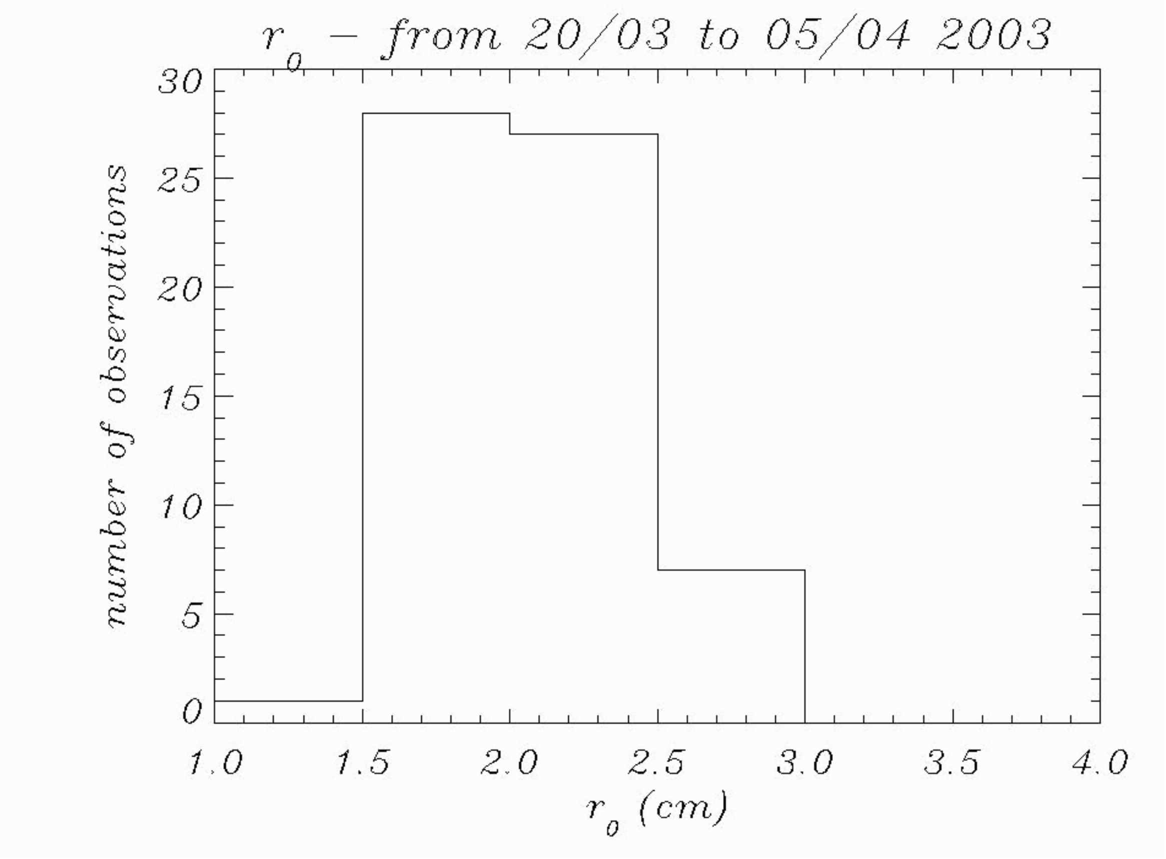

Figure 9: This figure shows the histogram of r_0 from March 20 to April 5, 2003.

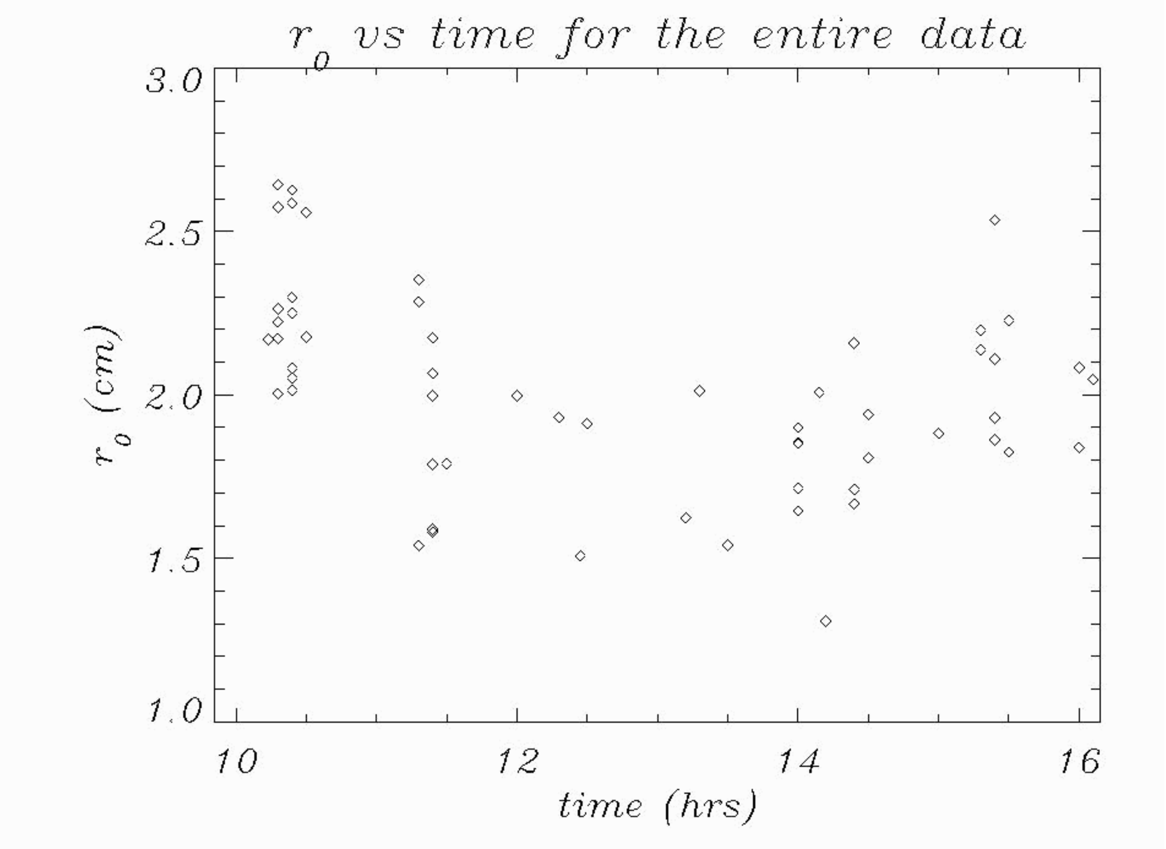

Figure 10: This figure shows the variation of r_0 with time for the entire data.

Annexure II

AO Component Details

Component	Accessories and Specifications	Company
Tip-Tilt stage	1. K-108-00, PSH 8 Piezo tilting system, 2 active axes, -10 to 150 V, Dimension: 25 x 25 x 60 mm, cable length:1m, LEMOSA connector, Piezo -electric mounted crystal 2. ENV modular amplifier system, Series ENV 150, part no. E-103-20, 14TE wide, 1 channel, LEMOSA connector, voltage: -10 to 150 V (2 in quantity) 3. Casing for ENV system, 63 TE, 9" system, power supply wire, part no E-103-90 4. ENT 150: 230 V main supply, module width 14 TE, output power 50 W The 2-channel DAC voltage output card from Measurement Computing (concept electronics being Indian agents) used by Keller for tip-tilt mirror has been replaced by DaqBoard/2000 of IOtech as it is compatible with PCI slots.	Piezosystem Jena GmbH, Prossingstr 27, D-07745, Jena, Germany. Phone: +49-3641-66 88-0 Fax : +49-3641-66 88 –66 Email: info@piezojena.com
Tip-tilt mirror	1. Diameter 25 mm 2. Thickness 10 mm 3. Surface Accuracy $\lambda/6$ (rms)	Prisms India Private Ltd. C-92, PIPDIC Industrial Estate, Mettuppalayam, Pondicherry, 605 009 Phone: 0413-2277059, 2271289, 2277060 Fax: 0413-2250328 www.prismsindia.com Email: prisms@vsnl.com
Deformable mirror	1. 37 actuator, 15 mm diameter membrane mirror 2. Mirror socket consisting of a PCB holder with PGA (Pin Grid Array) compatible connector on the front side and two band cable connectors on the back side from OKO Technologies. 3. 2 high voltage amplifier boards, each containing 20 non-inverting DC 4. Amplifies with gain 53, providing output voltage swing of 1-255 V for the input range of 0 to 4.5 V, for controlling mirror shape 5. One power-supply with ±15 V, another high voltage power supply (with maximum of 300V)	OKO Technologies, Reinier de Graafweg 300, 2625 DJ Delft, The Netherlands. Fax: 31-15-2574233 Email: oko@okotech.com

Lenslet array	1. Focal length : 145 mm 2. Pitch : 0.6 mm 3. Shape : Hexagonal 4. 9 × 9 lenslets etched on a glass plate of 18 mm dia.	Smart Micro Optical Solutions (SMOS) Entwicklung und Herstellung Mikrooptischer Elemente Dannheckerstr, 43 d, 69190 Walldorf. Germany
CCD camera and accessories	Camera : 1. Model no. DALSTAR CA-D6, 2. 260 by 260 pixels, 3. 995 frames per second readout, 4. 8 bit internal digitization	DALSA WATERLOO, 605 MC Murray Road, Waterloo,ONTANIO, CANADA N2V2EG Phone: 519-886-6000 Fax: 519-886-8023
	Frame grabber : 1. PC-DIG PCI LVDS frame grabber 2. Driver for Windows The driver software for the Linux platform, called Imaging Technology Inc.-Frame Grabber (ITI-FG) device driver, is provided freely by GOM mbH. *Web : http://oss.gom.com*	CORECO Imaging, 7075 Place Robert Joncas, Suite # 142, St. Laurent Quebec, Canada, H4M2Z2 Phone: 514-333-1301 Fax: 514-333-1388 Indian representatives: Online solutions Imaging Pvt. Ltd., 3,Thiruvalluvar Street, Rajaram Mehta Nagar, Aminjikarai, Chennai 600 029, India. Phone: 91-044-3741935 Fax: 91-044-3744579 Mobile: 98400 82630 Email: online_solutions@vsnl.com
	CCD camera frame grabber cable : DBH-D100 – TO – OPEN 100 pin LVDS	MATROX Electronics System Ltd, 1055, Boulst-Regis, Dorual (Quebec), Canada H9P2T4 Phone: 514-822-6000 Fax: 514-822-6292 Web: www.matrox.com
	CCD camera power supply	USO, Udaipur
Control computer:	IBM compatible computer system Intel Pentium 4 processor 2.4+ GHz., 845 chipset Intel Box motherboard, 512 MB DDR memory, Standard 40 GB hard disk drive, 6 PCI back planes, 1 CNR slot parallel, serial and USB ports, 10/100 MBPS Ethernet card, Keyboard, mouse, CD writer 52 x R-W speed, 1.4MB FDD, cables and manuals, 17” color monitor, Red-Hat Linux 9 OS	
Narrow-band Interference filters	Part No. CW(nm) BW(nm) 1427-5773-0010 577.3 1 1427-4305-0010 430.5 1 1427-8542-0010 854.2 0.3 CW : Center wavelength BW : Band Width	Spectra-Film, 34, Dunham Road, Billerica, Massachusetts 01821, USA

Broad-band and Neutral Density filters	Broad band filter : Part No: 500FS20-25 CW : 501.3 nm BW @ (50 %) : 20 nm (491-511nm) Incidence angle : 0 Neutral Density filters : Part No. xxx-FN52-25 xxx- 300, 250, 200, 150, 100, 90, 80, 70, 60, 50, 40, 30, 20, 10	Andover Corporation 4,Commercial Drive, Salem NH 03079 USA. Phone: (603)-893-6888 Fax: (603)-893-6508 www.andcorp.com
Optical table, mounting supports	Research Grade Optical Table Model No. : M-RS1000-48-12 Width 4ft, height 8ft, thickness 12 inch, I-2000-4H vibration isolators Portable noiseless air compressor (ACMP-02 JUN-AIR)	Newport corporation USA www.newport.com

Annexure III

Some Considerations Regarding Control System Based on Mt. Abu Telescope:

Small/medium telescope controller is available as a stand-alone unit with hand set and RS-232 serial control. In this case, we can use any operating system. Serial control is possible, with either windows or Linux using a small program. For networking (TCP/IP), a small module is available, which converts from RS-232 to any other standard.

Some important points:

1. Safety limits in software and hardware are required.

2. Vibration free operation on telescope mount.

3. Tracking accuracy: 0.1 arc-sec in 10 s; 0.5 arc-sec in 600 s.

4. Slew rate/ fast movement rate: 2° per sec available for Mt. Abu telescope but small telescope can have even higher: 5° per sec.

5. Medium speed for Mt. Abu telescope is 2 arc-min per sec.

6. Absolute pointing needs to be ± 10 arc-sec above 30° elevation.

7. Relative pointing within 5° area: ±1 arc-sec.

8. Az/Elevation needs instrumentation rotation at 0.1° or better accuracy.

9. Windscreen needs to be interfaced.

10. AC input supply 230 V, 50 Hz Indian standard.

11. Adjustment for elevation and azimuth in mount.

12. UPS operation for telescope will constrain the choice of drive motors.

Annexure IV

ATST Modulator Matrix

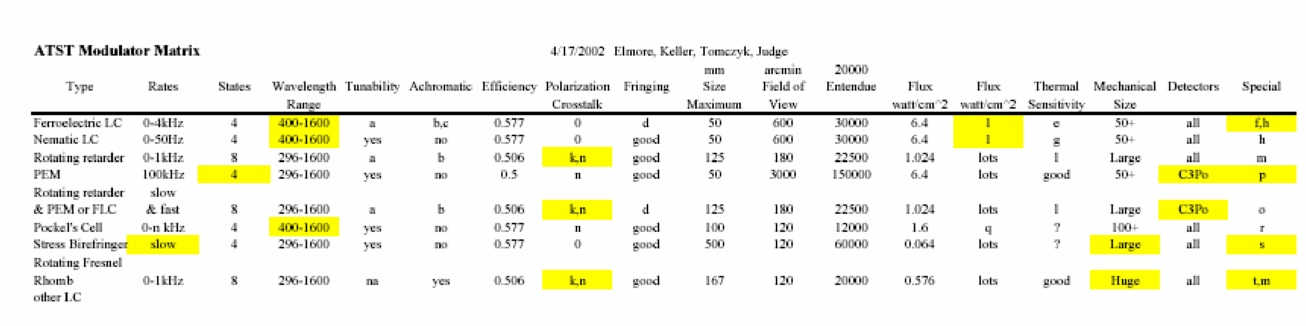

ATST Modulator Matrix 4/17/2002 Elmore, Keller, Tomczyk, Judge

Type	Rates	States	Wavelength Range	Tunability	Achromatic	Efficiency	Polarization Crosstalk	Fringing	mm Size Maximum	arcmin Field of View	20000 Entendue	Flux watt/cm^2	Flux watt/cm^2	Thermal Sensitivity	Mechanical Size	Detectors	Special
Ferroelectric LC	0-4kHz	4	400-1600	a	b,c	0.577	0	d	50	600	30000	6.4	l	e	50+	all	f,h
Nematic LC	0-50Hz	4	400-1600	yes	no	0.577	0	good	50	600	30000	6.4	l	g	50+	all	h
Rotating retarder	0-1kHz	8	296-1600	a	b	0.506	k,n	good	125	180	22500	1.024	lots	l	Large	all	m
PEM	100kHz	4	296-1600	yes	no	0.5	n	good	50	3000	150000	6.4	lots	good	50+	C3Po	p
Rotating retarder & PEM or FLC	slow & fast	8	296-1600	a	b	0.506	k,n	d	125	180	22500	1.024	lots	l	Large	C3Po	o
Pockel's Cell	0-n kHz	4	400-1600	yes	no	0.577	n	good	100	120	12000	1.6	q	?	100+	all	r
Stress Birefringer	slow	4	296-1600	yes	no	0.577	0	good	500	120	60000	0.064	lots	?	Large	all	s
Rotating Fresnel Rhomb	0-1kHz	8	296-1600	na	yes	0.506	k,n	good	167	120	20000	0.576	lots	good	Huge	all	t,m
other LC																	

a	Panchratnam arrangement could rotate center element to obtain desired retardance at a range of wavelengths. Fast axis will wander. Retardance tunability a possibility.
b	Pnachratnam fixed arrangement would be achromatic. Multiple panchratnam plates possible.
c	Combination of LC materials may be possible for achromaticity.
d	Fringing depends upon the number of surfaces. A Panchratnam configuration could have significant fringes
e	Range of axis switching is a function of temperature. Range diminishes approximately .7degress/C
f	Low voltage switchable.
g	Approximately 0.25 degrees of retardance/C
h	Careful characterization of retardance vs voltage and temperature is important.
j	Achromatic bi-crystaline retarders have been fabricated. Super achromatic panchratnam retarder is possible
k	Since all states not modulated with equal efficiency, telescope polarization variations from intensity leak into polarizaiton
l	Thermal sensitivity of a crystal or bi-crystalline achromat is large. An athermal bi-crystalline non-achromat has been designed.
M	Rotating mechanical device must have good servo and is very large compared to optic.
n	Modulation could be fast compared to seeing therefore eliminating crosstalk. If fast enough only one beam is needed.
o	Similar system used in Mk4. Frequency response has not been modeled.
p	Precise phasing of two PEMs and detector has not yet been demonstrated
q	Depends upon conducting layer
	r Much progress since Stokes II. Research needed here.
s	A lot of energy to create retardance. Nearly uncharted territory.
t	Huge mechanical beast. Do not now know how to make a retarder of about 3/8 wave.

C3Po = Charge Caching Cmos PhOtodetectors, Detectors CCD, HgCdTe, C3Po vis or IR

Acknowledgement

The contributions of Profs. G. S. Agarwal, R. K. Varma, R. Cowsik, S. M. Chitre, G. Srinivasan, in the early stages of the project are acknowledged. In addition, Profs. U. R. Rao and G. S. Agarwal have been extremely patient with continued support, in terms of finance and manpower.

The speedy responses provided by PRL and USO administration, in particular, Messrs. M. R. G. Murthy, G. N. Nagori, Y. M. Trivedi, N. Ravishankar, C. V. R. G. Deekshitulu, and R. Koshy have been quite remarkable. The crucial comments of the committee members, Prof. S. Krishnaswami, Prof. S. N. Tandon, Prof. S. Ananthakrishnan, Prof. R. S. Sirohi, Dr. A. S. Kiran Kumar, Dr. Hemant Dave, Dr. A. K. Saxena, and Dr. T. G. K. Murthy are gratefully acknowledged, and also the earlier encouragement from Drs. George Joseph, Rob Rutten and Luc Dame. Drs. John Leibacher, Jack Harvey, Christoph Keller, Dirk Soltau, G. B. Scharmer, Oskar von der Lühe and O. Engvold have given patient responses to our numerous queries. Drs. Jacques Beckers and Peter Brandt provided valuable tips on “seeing”. Mr. John Briggs and his colleagues at NSO helped a lot on the issue of scintillometers. Drs. K. Sankarasubramanian and Shibu K. Mathew are acknowledged for their inputs for the back-end instruments.

Many vendors gave useful feed-back on our earlier request for budgetary quotations but special mention must be made of Craig Smith of EOST. Mr. Rajesh Shah of Mt. Abu also provided useful inputs on the control system. Finally, a special mention must be made of Dr. K. Kasturirangan’s comments during an ISRO council review that decided the direction of the project development.